

UNIVERSITÉ DE GENÈVE

FACULTÉ DES SCIENCES

Section de physique

Professeure Anna Sfyrla

Département de physique nucléaire
et corpusculaire (DPNC)

**Top-quark pair production cross-section measurements
in the all-hadronic decay channel at the ATLAS experiment
and
hardware-based track reconstruction
for the ATLAS trigger HL-LHC upgrade**

THÈSE

présentée à la Faculté des sciences de l'Université de Genève
pour obtenir le grade de Docteur en sciences, mention physique

par

Riccardo Poggi

de Broni, Pavia (Italie)

Thèse N° 5548

GENÈVE

Atelier d'impression ReproMail
2021



**UNIVERSITÉ
DE GENÈVE**

FACULTÉ DES SCIENCES

DOCTORAT ÈS SCIENCES, MENTION PHYSIQUE

Thèse de Monsieur Riccardo POGGI

intitulée :

**«Top-quark Pair Production Cross-section
Measurements in the All-hadronic Decay Channel
at the ATLAS Experiment
and
Hardware-based Track Reconstruction for the
ATLAS Trigger HL-LHC Upgrade »**

La Faculté des sciences, sur le préavis de Madame A. SFYRLA, professeure associée et directrice de thèse (Département de physique nucléaire et corpusculaire), Monsieur F. RIVA, professeur assistant (Département de physique théorique), Monsieur X. WU, professeur associé (Département de physique nucléaire et corpusculaire) et Monsieur G. SALAMANNA, professeur (Department of Mathematics and Physics, Roma Tre University, Rome, Italy), autorise l'impression de la présente thèse, sans exprimer d'opinion sur les propositions qui y sont énoncées.

Genève, le 25 février 2021

Thèse - 5548 -

Le Doyen

Abstract

As the heaviest particle of the Standard Model, the top quark is a key ingredient in both precision electroweak physics measurements and searches for new physics models. The top-quark production processes, such as the top-quark pair production, constitute a significant background to many searches for physics beyond the Standard Model. Increasing the accuracy of theoretical models associated with the top-quark production is of central importance for improving measurements and searches at the LHC.

In this thesis are presented single- and double-differential cross-section measurements for the production of top-quark pairs in the resolved topology of the all-hadronic channel, using data collected by the ATLAS detector at the CERN LHC from proton–proton collisions at 13 TeV during 2015 and 2016, corresponding to an integrated luminosity of 36.1 fb^{-1} .

These differential distributions are measured in data with corrections both to the stable-particle level in a fiducial phase space and to the parton level in the full phase space. Correlations between the $t\bar{t}$ system and associated jet production are also measured and compared with predictions of matrix element calculations.

The results can be used to improve the top-quark Monte Carlo modelling. In particular, the particle-level results provide insight in regions of the phase space with many additional jets and can be used in future PDF measurements and top-quark pole mass extraction.

The rapidities of the individual top quarks and of the top-quark pair are found to be well modelled, while the leading top-quark transverse momentum and top-quark pair transverse momentum are found to be incompatible with several theoretical predictions. Significant mismodelling is observed in the hardness of the additional jet emissions.

A comparison with other published results is also presented, showing the predictions to be rather accurate and for the most part compatible in the different regions of phase space and for different channels. However, some tension remains and better models are indeed needed to reproduce the data for all observables in all channels. Compared to other channels, the all-hadronic chan-

nel leads to better resolution for observables such as angular distributions and measurements of extra jets relative to the top-quark pair system.

Future prospects for the application of machine learning algorithms for the reconstruction of the $t\bar{t}$ all-hadronic system are also presented. A deep neural-network architecture has been developed with embedded elements of special relativity, showing favourable results when compared with a more conventional χ^2 -minimisation technique. The proposed approach targets the problem of large combinatorics resulting from the large jet multiplicity in the final state. This method, benchmarked for the $t\bar{t}$ system, will provide a novel solution for handling large combinatorics, also common in high jet multiplicity searches at the LHC.

This thesis includes work related to the upgrade program of the ATLAS trigger and data acquisition system for the High-Luminosity LHC. In particular, studies for the development of the *hardware tracking for the trigger* (HTT) are presented.

To cope with the expected high-pile-up conditions the HTT system uses information from the upgraded ATLAS tracking detector to provide reconstructed particle tracks as early as possible in the trigger selection.

The study carried out for the HTT prototype obtained estimates on the FPGA resources necessary to achieve the targeted computational goal. These results are used to drive the choice of FPGA vendor and model for the upgrade project.

Resumé

En tant que la particule plus lourde du Modèle Standard, le quark top est un ingrédient clé à la fois dans les mesures de précision de la physique électrofaible et dans la recherche de nouvelle physique au-delà du Modèle Standard. Les processus de production du quark top, tels que la production de paires, constituent une partie importante du bruit de fond qu'il faut rejeter pour observer des particules au-delà du Modèle Standard. L'augmentation de la précision des modèles théoriques associés à la production de quarks top est d'une importance capitale pour améliorer les mesures et les recherches au LHC.

Dans cette thèse sont présentées des mesures de section différentielle pour la production de paires de quarks top dans la topologie résolue du canal tout-hadronique, en utilisant les données collectées par le détecteur ATLAS au LHC du CERN lors de collisions protons-protons à 13 TeV en 2015 et 2016, correspondant à une luminosité intégrée de 36.1 fb^{-1} .

Ces distributions différentielles sont mesurées dans les données avec des corrections au niveau des particules stables dans un espace de phase fiducial et au niveau du parton dans un espace de phase complet. Les corrélations entre le système $t\bar{t}$ et la production de jet associée sont également mesurées et comparées aux prédictions des calculs des éléments de matrice.

Les résultats peuvent être utilisés pour améliorer la modélisation Monte Carlo du quark top. En particulier, les résultats au niveau des particules donnent un aperçu des régions de l'espace de phase avec beaucoup de jets supplémentaires et peuvent être utilisés dans de futures mesures de PDF et d'extraction de la masse du pôle du quark top.

Le rapidité des quarks top individuels et par paires sont bien modélisées, tandis que le moment transversal du quarks top et le moment transversal de la paire de quarks top sont incompatibles avec plusieurs prédictions théoriques. L'écart entre la modélisation et les mesures de la dureté des émissions de jets supplémentaires est important.

Une comparaison avec d'autres résultats publiés est également présentée, montrant que les prédictions sont plutôt précises et pour la plupart compatibles dans les différentes régions de l'espace de phase et pour différents canaux. Cependant,

une certaine tension subsiste et de meilleurs modèles sont en effet nécessaires pour reproduire les données pour tous les observables dans tous les canaux. Les observables, telles que les distributions angulaires et les mesures de jets supplémentaires au système de paires de quarks, ont une meilleure résolution dans le canal tout-hadronique par rapport à d'autres canaux.

Les perspectives d'avenir pour l'application d'algorithmes d'apprentissage automatique pour la reconstruction du système entièrement électronique sont également présentées. Une architecture de réseau neuronal profond a été développée avec des éléments intégrés de relativité spéciale, montrant des résultats favorables par rapport à une technique plus conventionnelle de minimisation de χ^2 . L'approche proposée essaie de résoudre le problème des grandes combinatoires lié au grand nombre de jet dans les états finaux. Cette méthode, étalonnée pour le système $t\bar{t}$, apportera une nouvelle solution pour traiter les grandes combinatoires, celles-ci étant un problème commun à de nombreuses recherches sur la multiplicité des jets au LHC.

Cette thèse inclut des travaux liés au programme de mise à niveau du système de trigger et d'acquisition de donnée du ATLAS en préparation pour le LHC à haute luminosité. En particulier, des études pour le développement de le système d'*hardware tracking for the trigger* (HTT) sont présentés.

Pour faire face aux conditions prévues du pile-up élevé prévues, le système HTT utilise les informations du nouveau traceur d'ATLAS pour fournir des traces de particules reconstituées le aussi tôt que possible dans la sélection du trigger.

L'étude réalisée pour le prototype HTT a permis d'obtenir des estimations sur les ressources de FPGA nécessaires pour atteindre l'objectif de calcul visé. Ces résultats sont utilisés pour orienter le choix du fournisseur de FPGA et du modèle à suivre pour le projet de mise à niveau.

Contents

Introduction	13
1 Theoretical framework	15
1.1 The Standard Model of particle physics	15
1.2 Quantum chromodynamics	16
1.3 Electroweak theory	18
1.4 Standard model achievements	27
1.5 Standard model shortcomings	28
2 Top quark physics at the LHC	31
2.1 The Large Hadron Collider	31
2.2 Top quark production and decay modes	34
2.3 Top quark pair production	36
2.4 Top-quark mass	39
3 The ATLAS detector	43
3.1 Magnet system	45
3.2 Coordinate system	46
3.3 Inner detector	46
3.4 Calorimeter system	48
3.5 Muon spectrometer	51
4 The ATLAS trigger and data acquisition system	55
4.1 System characterisation	55
4.2 Trigger menu	57
4.3 Level-1	59
4.4 High level trigger	62
5 The hardware tracking for the trigger	65
5.1 The high luminosity LHC	65
5.2 ATLAS TDAQ for phase-II	66
5.3 Hardware tracking for the trigger	69
5.4 Track fitting for the PRM	73
5.5 Digital signal processing performance test	76

5.6	Resource allocation estimate	79
6	Analysis motivation	83
6.1	Observables	84
7	Data and Monte Carlo samples	89
7.1	Data samples	89
7.2	Monte Carlo samples	89
8	Object reconstruction	95
8.1	Electrons	95
8.2	Muons	97
8.3	Jets	99
8.4	Hadronic taus	101
8.5	Overlap removal	101
8.6	Particle-level objects definitions	102
8.7	Parton-level objects definitions	102
9	Event selection	103
9.1	Event selection	103
9.2	Kinematic reconstruction of the $t\bar{t}$ system	107
9.3	Multi-jet background rejection	109
9.4	Kinematic Likelihood alternative study	109
10	Background estimate	115
10.1	Data-driven estimate of multi-jet background	115
10.2	Distributions of signal region selecting variables	119
10.3	Multi-jet background for different jet multiplicities	122
11	Unfolding	125
11.1	Iterative Bayesian method	125
11.2	Unfolding at particle level	126
11.3	Unfolding at parton level	128
12	Systematic uncertainties	129
12.1	Experimental uncertainties	130
12.2	Signal modelling uncertainties	131
12.3	Background modelling uncertainties	133
12.4	Systematic uncertainties summary	134
13	Results	135
13.1	Data-MC agreement	135
13.2	Results at particle level	137
13.3	Results at parton level	149

13.4 Total cross-section	155
14 Comparison with other ATLAS differential cross-section measurements	157
14.1 Comparison of results with the ℓ +jets channel	157
14.2 Comparison of results with the all-hadronic channel in the boosted topology	160
15 Deep neural network for $t\bar{t}$ system reconstruction	163
15.1 Architecture	164
15.2 Jet assignment	165
15.3 Performance	167
Conclusions	171
Bibliography	173

Introduction

As the heaviest particle of the standard model, the top quark provides an insight into a wide range of topics, including proton structure and precision electroweak physics. Top-quark pair production is also the most significant background to many searches for physics beyond the standard model. Therefore, improving the accuracy of theoretical models for this production process is of central importance.

This thesis focuses on the analysis of data collected by the ATLAS experiment at the *large hadron collider* (LHC) and on the upgrade of the ATLAS detector planned for the *high-luminosity LHC* (HL-LHC).

Measurements of differential cross-sections for the production of top-quark pairs are presented, using data collected by the ATLAS detector at a centre-of-mass energy $\sqrt{s} = 13$ TeV in 2015 and 2016 and corresponding to 36.1 fb^{-1} of proton–proton (pp) collisions.

The resolved all-hadronic final state is analysed. Specifically, each top quark decays into a bottom quark and two additional quarks, and all three quarks from each top-quark decay are resolved into distinct jets, leading to at least six jets in the final state. This final state has the largest branching ratio, but is subject to a large background contamination from multi-jet production.

Differently than other final states, the absence of neutrinos accompanying leptonic decays avoids kinematic ambiguities and allows for a full reconstruction of the top-quark pair without utilising the missing transverse momentum.

Single- and double-differential distributions of the kinematic properties of the top-quark–top-antiquark ($t\bar{t}$) system are presented. These differential distributions are measured in data with corrections both to the stable-particle level in a fiducial phase space and to the parton level in the full phase space. These results can be used to strengthen constraints on parton distribution functions and tuning of precision cross-section computations.

Correlations between the $t\bar{t}$ system and associated jet production are also measured, and are compared with predictions of matrix element calculations.

Relatively to the phase-II upgrade program of the ATLAS detector, studies of

the *hardware tracking for the trigger* (HTT) system are presented.

Charged particle reconstruction at the HL-LHC presents a special challenge for the ATLAS *trigger and data acquisition* system, a critical hardware and software component which holds the very challenging task of selecting the few interesting interactions concealed within a huge background in almost in real-time.

To cope with the expected high-pile-up conditions the HTT uses information from the upgraded ATLAS tracking detector to provide reconstructed particle tracks as early as possible in the trigger selection.

The HTT system comprises custom-designed electronic boards using *associative memories* (AMs) *application-specific integrated circuits* (ASICs) for pattern recognition and *field programmable gate arrays* (FPGAs) for track reconstruction and fitting.

The work of this thesis has produced the following public material:

- “Measurements of $t\bar{t}$ differential cross-sections of highly boosted top quarks decaying to all-hadronic final states in pp collisions at $\sqrt{s} = 13$ TeV using the ATLAS detector” [1],
- “Design of the ATLAS phase-II hardware-based tracking processor” [2],
- “Digital Signal Processing in FPGA for Particle Track Reconstruction at the HL-LHC ATLAS” [3].

The thesis is structured as follows. In chapter 1 is presented the standard model of particle physics. Chapter 2 focuses on the top-quark physics. In chapter 3, a general view of the ATLAS detector at the LHC together with a timeline of its planned upgrade is reported. In chapter 4 are presented the physics and technological challenges of the ATLAS trigger and data acquisition system. In chapter 5 are reported the estimates and performance tests performed in the context of the HTT upgrade. In chapter 6, the motivation for the analysis are illustrated. In chapter 7, a description is given of the data and MC samples used. The event reconstruction is defined in chapter 8. In chapter 9, the selection criteria is described. In chapter 10, the procedure used to evaluate the multi-jet background is illustrated. The unfolding procedure used to correct for the detector and reconstruction effects is described in chapter 11. The systematic uncertainties and the results are presented respectively in chapter 12 and 13. In chapter 14, the comparison of common observables with other $t\bar{t}$ decay channels is presented. In chapter 15, one additional study for future prospects on the use of machine learning techniques for $t\bar{t}$ system reconstruction is presented.

Theoretical framework

The *Standard Model* (SM) of particle physics is a theoretical framework that was developed throughout the second half of the 20th century [4, 5, 6] and has evolved over the years in a collaborative effort by theoretical and experimental physicists alike.

It classifies all known elementary particles and it describes three of the four known fundamental forces in the universe. The electromagnetic, the weak, and the strong interactions are included in the SM, while the gravitational force has been found, so far, to be mathematically irreconcilable with the quantum mechanical description used by the SM.

Although the SM is not a complete theory that can explain all fundamental physical aspects of the universe, it has demonstrated enormous and continuous success in providing experimental predictions.

1.1 The Standard Model of particle physics

The SM is a gauge quantum field theory based on the local gauge symmetry group

$$SU(3)_C \times SU(2)_L \times U(1)_Y, \quad (1.1)$$

where $SU(3)_C$ is the unbroken *colour* (C) symmetry, corresponding to the non-abelian gauge theory called *quantum chromodynamics* (QCD); while $SU(2)_L \times U(1)_Y$ is the combined symmetry of *isospin* (L) and *hypercharge* (Y), corresponding to the *electroweak* (EW) non-abelian gauge theory.

The fields of the theory are spin- $1/2$ *fermion* fields called *Dirac fields*, which are in turn classified into six *leptons* (l), six *quarks* (q) and their respective *anti-particles* (\bar{l} and \bar{q} respectively).

Quarks and fermions are further divided into three pairs of particles exhibiting similar physical behaviours. These three tiers or *families* are called *flavours* or *generations*.

The SM *Lagrangian*, which is invariant under its symmetry group, can be written as a combination of two separate QCD and EW contributions as

$$\mathcal{L}_{\text{SM}} = \mathcal{L}_{\text{QCD}} + \mathcal{L}_{\text{EW}}. \quad (1.2)$$

QCD is the theory of strong interaction and it describes the interactions between quarks, anti-quarks and the eight gauge bosons of the theory called *gluons*.

EW is instead a *chiral* theory which includes four gauge bosons, the higgs boson doublet, their mutual interaction and their interaction with the fermion fields.

1.2 Quantum chromodynamics

The $\text{SU}(3)_C$ of QCD acts on the three kinds of “colour” charges: *red* (r), *blue* (b) and *green* (g). The quarks and anti-quarks carry one single colour charge, which typically changes at the quark-gluon vertex. The gluons carry two units of charge, one of colour and one of anti-colour. The gluons transform in the adjoint representation of the gauge group, while the quarks transform in the fundamental representation.

The quarks transform in the fundamental representation of $\text{SU}(3)_C$, while the gluons transform in the adjoint representation.

The QCD Lagrangian, involving only quarks and gluons, comprises the addition of two terms:

$$\mathcal{L}_{\text{QCD}} = -\frac{1}{4}G_{\mu\nu}^a G^{\mu\nu a} + \bar{q}(i\gamma^\mu D_\mu)q. \quad (1.3)$$

Referring to the first term of Eq. (1.3), $G_{\mu\nu}^a$ is the gauge invariant field associated to $\text{SU}(3)_C$ defined as

$$G_{\mu\nu}^a = \partial_\mu G_\nu^a - \partial_\nu G_\mu^a - g_s f^{abc} G_\mu^b G_\nu^c, \quad (1.4)$$

where $G_\mu^a(x)$ ($a \in 1, 2, \dots, 8$) are the eight gluon fields, f^{abc} ($a, b, c \in 1, 2, \dots, 8$) is the structure constants of the corresponding Lie algebras of $\text{SU}(3)_C$ and g_s is the QCD coupling constant also referred to as $\alpha_s = g_s^2/4\pi$.

The third term, $g_s f^{abc} G_\mu^b G_\nu^c$ of Eq. (1.4), represents the gluon self-interaction and is responsible for the non-Abelian nature of QCD.

Although a treatment of the renormalisation of the SM Lagrangian exceeds the

scope of this thesis, the value of α_s is not independent from the energy scale of the interaction process relative to the energy parameter chosen as part of the renormalisation scheme.

At the first order or *one loop* approximation, the coupling constant can be expressed as

$$\alpha_s(\mu_R^2, \Lambda^2) = \frac{4\pi}{\beta_0^{(n_f)} \log(\frac{\mu_R^2}{\Lambda^2})}, \quad (1.5)$$

where μ_R is the renormalisation energy scale of the process, Λ is the asymptotic scale parameter, $\beta_0^{(n_f)}$ is the first order approximation of a more general beta function and it is equal to $11 - 2/3 n_f$, where n_f is the number of active flavours involved in the process.

If $n_f \leq 16$ (which is the case for the SM, where $n_f = 3$), the beta parameter dictates the presence of a phenomenon known as *asymptotic freedom*, where the coupling α_s decreases with the increasing energy scale and in the high energy limit the quarks are allowed to propagate as free particles.

Instead, in the low energy limit, the phenomenon of *quark confinement* ensues, where the value of α_s grows towards a diverging point and quarks and gluons can not appear as free particles.

Referring to the second term of Eq. (1.3), γ^μ are the Dirac γ -matrices, a set of conventional matrices $\{\gamma^0, \gamma^1, \gamma^2, \gamma^3\}$ with a specific anticommutation relation

$$\{\gamma^\mu, \gamma^\nu\} = 2g^{\mu\nu} I_4, \quad (1.6)$$

where I_4 is the 4×4 identity matrix and $g^{\mu\nu}$ is the Minkowski metric.

In the Dirac basis, the γ -matrices correspond to

$$\gamma^0 = \begin{pmatrix} I_2 & 0 \\ 0 & -I_2 \end{pmatrix} \quad \text{and} \quad \gamma^i = \begin{pmatrix} 0 & \sigma^i \\ -\sigma^i & 0 \end{pmatrix}, \quad (1.7)$$

where I_2 is the 2×2 identity matrix and σ_i are the Pauli matrices

$$\sigma_1 = \sigma_x = \begin{pmatrix} 0 & 1 \\ 1 & 0 \end{pmatrix}, \quad \sigma_2 = \sigma_y = \begin{pmatrix} 0 & -i \\ i & 0 \end{pmatrix} \quad \text{and} \quad \sigma_3 = \sigma_z = \begin{pmatrix} 1 & 0 \\ 0 & -1 \end{pmatrix}. \quad (1.8)$$

Referring again to the second term of Eq. (1.3), q is the quark field in the fundamental $SU(3)_C$ representation. It is a 3-component object or triplet, with

colour index r, g and b :

$$q = \begin{pmatrix} q_r \\ q_g \\ q_b \end{pmatrix} \quad \text{and} \quad \bar{q} = \begin{pmatrix} \bar{q}_r & \bar{q}_g & \bar{q}_b \end{pmatrix}, \quad (1.9)$$

where each component is itself a 4-component Dirac spinor of $SU(2)_L \times U(1)_Y$ as described in Sec. 1.3.2. To be noted that in this section the quarks flavour index is omitted for ease of notation, while in Sec. 1.3 the colour index is omitted for ease of notation.

The final component of Eq. (1.3) that needs to be defined is D_μ , the gauge-covariant derivative, which is introduced through minimal substitution of the partial derivative by promoting the global gauge symmetry to a local one.

$$D_\mu = \partial_\mu + ig_s T^a G_\mu^a, \quad (1.10)$$

where T^a are the eight generators of $SU(3)_C$, which are 3×3 Hermitian traceless matrices defined as $T^a = \lambda_a/2$, with respect to the Gell-Mann's basis λ_a :

$$\begin{aligned} \lambda_i &= \begin{pmatrix} \sigma_i & 1 \\ & 0 \\ 0 & 0 & 0 \end{pmatrix} \text{ for } i = 1, 2, 3; & \lambda_4 &= \begin{pmatrix} 0 & 0 & 1 \\ 0 & 0 & 0 \\ 1 & 0 & 0 \end{pmatrix}; & \lambda_5 &= \begin{pmatrix} 0 & 0 & -i \\ 0 & 0 & 0 \\ i & 0 & 0 \end{pmatrix}; \\ \lambda_6 &= \begin{pmatrix} 0 & 0 & 0 \\ 0 & 0 & 1 \\ 0 & 1 & 0 \end{pmatrix}; & \lambda_7 &= \begin{pmatrix} 0 & 0 & 0 \\ 0 & 0 & -i \\ 0 & i & 0 \end{pmatrix}; & \lambda_8 &= \frac{1}{\sqrt{3}} \begin{pmatrix} 1 & 0 & 0 \\ 0 & 1 & 0 \\ 0 & 0 & -2 \end{pmatrix}; \end{aligned}$$

and therefore satisfying the commutation relation:

$$[T^a, T^b] = if^{abc} T^c. \quad (1.11)$$

1.3 Electroweak theory

The EW theory describes the weak and electromagnetic interactions and its Lagrangian, invariant under $SU(2)_L \times U(1)_Y$, can be divided into four sectors as

$$\mathcal{L}_{EW} = \mathcal{L}_{\text{gauge}} + \mathcal{L}_{\text{ferm}} + \mathcal{L}_\Phi + \mathcal{L}_Y. \quad (1.12)$$

- The gauge sector, $\mathcal{L}_{\text{gauge}}$, describes the gauge bosons dynamics.
- The fermion sector, $\mathcal{L}_{\text{ferm}}$, introduces the fermion fields and describes their interaction with the gauge bosons.
- The higgs sector, \mathcal{L}_{Φ} , introduces the higgs boson and describes its interaction with the gauge bosons and its self-coupling.
- The Yukawa sector, \mathcal{L}_Y , establishes fermion masses via their interaction with the higgs boson.

1.3.1 The gauge sector

The SM theory is based on the symmetry group of Eq. (1.1) and the gauge bosons sector corresponding to $\text{SU}(2)_L \times \text{U}(1)_Y$ is given by

$$\mathcal{L}_{\text{gauge}} = -\frac{1}{4}W_{\mu\nu}^i W^{\mu\nu i} - \frac{1}{4}B_{\mu\nu} B^{\mu\nu}, \quad (1.13)$$

where $W_{\mu\nu}^i$ and $B_{\mu\nu}$ are the gauge invariant fields associated to $\text{SU}(2)_L$ and $\text{U}(1)_Y$ respectively. Specifically, they are defined as

$$W_{\mu\nu}^i = \partial_\mu G_\nu^i - \partial_\nu W_\mu^i + g\epsilon^{ijk}W_\mu^j W_\nu^k \quad (1.14)$$

$$B_{\mu\nu} = \partial_\mu B_\nu - \partial_\nu B_\mu, \quad (1.15)$$

where $W_\mu^i(x)$ and $B_\mu(x)$ are the electroweak fields, ϵ^{ijk} is the structure constants of the corresponding Lie algebras of $\text{SU}(2)_L$, and g is the coupling constants of EW.

The three gauge fields $W_\mu^i(x)$ correspond to the three generators I^i of $\text{SU}(2)_L$, which are 2×2 Hermitian and traceless matrices $I^i = \sigma_i/2$, where σ_i are the Pauli matrices, and they satisfy the commutation relation:

$$[I^i, I^j] = i\epsilon^{ijk}I^k. \quad (1.16)$$

The single gauge field $B_\mu(x)$ corresponds to the generator Y of $\text{U}(1)_Y$, which is a 2×2 matrix proportional to the identity.

The electromagnetic subgroup

The electromagnetic group $\text{U}(1)_{\text{EM}}$ appears in the SM as a subgroup of the total electroweak group

$$\text{U}(1)_{\text{EM}} \subset \text{SU}(2)_L \times \text{U}(1)_Y, \quad (1.17)$$

via the Gell-Mann-Nishijima formula which relates Y , I_3 and the electrical charge generator Q by

$$Q = I_3 + \frac{Y}{2}. \quad (1.18)$$

1.3.2 The fermionic sector

The fermion fields of the SM, leptons and quarks, are divided into three generations.

The leptons that carry an integral negative electric charge are called *charged leptons* and include the *electron* (e), the *muon* (μ) and the *tau* (τ).

The other three leptons are neutral and are collectively called *neutrinos* (ν). Specifically, they are the *electron neutrino* (ν_e), the *muon neutrino* (ν_μ) and the *tau neutrino* (ν_τ).

The quarks carry a fractional electric charge with respect to the charged leptons of either $+2/3$ or $-1/3$. They are the *up* (u), *down* (d), *strange* (s), *charm* (c), *top* (t) and *bottom* (b) quarks.

The generic electroweak fermion is composed of two chiral components: a left-handed doublet and a right-handed singlets, which can be defined as follows:

$$\begin{aligned} \psi_L &= \frac{1}{2}(1 - \gamma_5)\psi, \\ \psi_R &= \frac{1}{2}(1 + \gamma_5)\psi, \end{aligned} \quad (1.19)$$

where ψ represents a fermion, the L and R indexes correspond the left-handed and right-handed components respectively, and γ^5 is a fifth γ -matrix defined with respect to the other four γ -matrices as $\gamma^5 := i\gamma^0\gamma^1\gamma^2\gamma^3$, which in the Dirac basis (see Eq. (1.7)) corresponds to

$$\gamma^5 = \begin{pmatrix} 0 & I_2 \\ I_2 & 0 \end{pmatrix}. \quad (1.20)$$

The EW leptons can therefore be written as

$$l_L^i \equiv \begin{pmatrix} \nu_{e^i L} \\ e_L^i \end{pmatrix}, \quad l_R^i \equiv e_R^i, \quad (1.21)$$

where the index i spans over the three flavor families, which for the charged leptons are $l^i = \{e, \mu, \tau\}$, while for the neutrinos are $\nu_e^i = \{\nu_e, \nu_\mu, \nu_\tau\}$. Right

handed neutrinos are absent in the SM (see Sec. 1.5.3).

In an analogous way, the EW quarks can be written as:

$$q_L^i \equiv \begin{pmatrix} u_L^i \\ d_L^i \end{pmatrix}, u_R^i, d_R^i, \quad (1.22)$$

where the index i spans again over the three flavor families $u^i = \{u, c, t\}$ and $d^i = \{d, s, b\}$.

The left- and right-handed EW fermions are respectively doublets and singlets of $SU(2)_L$.

Fermions and gauge bosons interaction

Due to their doublet and singlet nature, left and right chiral components of EM fermions interact differently by the gauge boson fields. Their interaction is described by the fermion sector Lagrangian as follows:

$$\mathcal{L}_{\text{ferm}} = \sum_{i=1}^3 q_L^i \not{D} q_L^i + u_R^i \not{D} u_R^i + d_R^i \not{D} d_R^i + l_L^i \not{D} l_L^i + l_R^i \not{D} l_R^i, \quad (1.23)$$

where q_L^i, q_R^i, l_L^i and l_R^i are the quark and lepton fields for all three flavour families, as defined above; \not{D} is shorthand for $\not{D} = \gamma^\mu D_\mu$ with the gauge-covariant derivative D_μ obtained through minimal substitution as

$$D_\mu = \partial_\mu + ig \mathbb{I}^i W_\mu^i + ig' Y B_\mu, \quad (1.24)$$

where \mathbb{I}^i and Y are the generators of $SU(2)_L$ and $U(1)_Y$ respectively (see Sec. 1.3.1). While g and g' are the coupling constant of $SU(2)_L$ and $U(1)_Y$ respectively.

1.3.3 The Higgs sector

An isospin doublet complex scalar field has been recently proven experimentally [7, 8] to be part of the SM (see Sec. 1.4). This field is known as the Higgs field and it is defined as

$$\Phi = \begin{pmatrix} \phi^+ \\ \phi_0 \end{pmatrix}, \quad (1.25)$$

where the superscript $+$ and subscript 0 indicate the electric charge of the components.

The scalar Lagrangian with a quartic self-interaction of the Higgs sector is

defined as

$$\mathcal{L}_\Phi = (D^\mu \Phi)^\dagger (D_\mu \Phi) - V(\Phi^\dagger \Phi), \quad (1.26)$$

where $V(\Phi^\dagger \Phi)$ represents the higgs potential, defined as

$$V(\Phi^\dagger \Phi) = -\mu^2 \Phi^\dagger \Phi + \frac{\lambda}{4} (\Phi^\dagger \Phi)^2. \quad (1.27)$$

The potential $V(\Phi^\dagger \Phi)$ depends on two parameters, μ^2 and λ . The case $\lambda < 0$ is considered not physical and leads to a non-stable minimum, while in the case of $\lambda > 0$ there are two possibilities: $\mu^2 > 0$ and $\mu^2 < 0$.

If $\mu^2 < 0$, the potential in Eq. (1.27) has one minimum, which corresponds to $\Phi^\dagger \Phi = 0$ and gives the vacuum expectation value $\langle 0 | \Phi | 0 \rangle = 0$. If instead $\mu^2 > 0$, the potential in Eq. (1.27) has a minimum for

$$\Phi^\dagger \Phi = \frac{\mu^2}{2\lambda} \equiv \frac{v^2}{2}. \quad (1.28)$$

Consequently, the Higgs field has a non-zero *vacuum expectation value* (VEV)

$$\langle 0 | \Phi | 0 \rangle = \frac{v}{\sqrt{2}}, \quad (1.29)$$

which defines the electroweak energy scale.

Additionally, the fundamental vacuum state is chosen to be

$$\Phi_0 \equiv \frac{1}{\sqrt{2}} \begin{pmatrix} 0 \\ v \end{pmatrix}. \quad (1.30)$$

Although Φ is a doublet of $SU(2)_L$, its lowest energy configuration, the Higgs field vacuum state Φ_0 , does not share the same symmetry. Specifically, since $I^i \Phi_0 \neq 0, \forall i$ and $Y \Phi_0 \neq 0$, invariance is broken for all four generators of $SU(2)_L \times U(1)_Y$. This is interpreted as the *spontaneous symmetry breaking* (SSB) of the electroweak group.

Furthermore, since the Higgs field vacuum state is invariant under $U(1)_{EM}$, due to the fact that Q as defined in Eq. (1.18) leads to $Q \Phi_0 = 0$, the electroweak group is said to spontaneously symmetry break into the electromagnetic subgroup

$$SU(2)_L \times U(1)_Y \xrightarrow{SSB} U(1)_{EM}. \quad (1.31)$$

To represent all true minimum states, the Higgs field can be rewritten as fluc-

tuations around its vacuum state and three out of four degrees of freedom, corresponding to the *Goldstone bosons* or *Higgs ghosts* generated during the SSB, can be rotated away with a unitary gauge transformation. As a result, $\phi^+ = 0$ and ϕ_0 loses its imaginary component becoming real. The Higgs field can therefore be written as

$$\Phi' = \begin{pmatrix} 0 \\ \frac{1}{\sqrt{2}}(v + h_0(x)) \end{pmatrix}, \quad (1.32)$$

where the remaining degree of freedom, h_0 , represents the actual particle associated to the Higgs boson field: an electrically neutral real scalar field.

At this point, after SSB, the interaction terms between the Higgs and the gauge fields generates mass terms for three out of the four electroweak bosons.

Since the unbroken gauge fields W_μ^i and B_μ are not eigenstates of the remaining $U(1)_{\text{EM}}$ group, their mass terms need to be diagonalised resulting in three massive gauge boson fields W_μ^\pm , Z_μ^0 , and one massless gauge boson field A_μ .

These new gauge bosons correspond to a linear combinations of the unbroken fields:

$$W_\mu^\pm = \frac{1}{2}(W_\mu^1 \mp W_\mu^2), \quad (1.33)$$

$$Z_\mu^0 = \cos(\theta_w)W_\mu^3 - \sin(\theta_w)B_\mu, \quad (1.34)$$

$$A_\mu = \sin(\theta_w)W_\mu^3 + \cos(\theta_w)B_\mu, \quad (1.35)$$

where θ_w is the weak mixing angle fixed by the coupling constants

$$\cos(\theta_w) = \frac{g}{\sqrt{g'^2 + g^2}} \quad \text{and} \quad \sin(\theta_w) = \frac{g'}{\sqrt{g'^2 + g^2}}. \quad (1.36)$$

The redefined gauge boson fields W_μ^\pm and Z_μ^0 correspond to the W^\pm and Z^0 massive vector bosons. The \pm signs of the W bosons refer to their respective electrical charge, whereas the Z^0 is electrically neutral.

The gauge boson A_μ corresponds to the massless photon and the unification relation

$$e \equiv \frac{gg'}{\sqrt{g'^2 + g^2}} \quad (1.37)$$

allows the massless boson A_μ to be interpreted as the *quantum electrodynamics* photon gauge boson.

By computing the interaction terms, the masses for the W^\pm and Z^0 result to be

$$m_W = g \frac{v}{2} \quad \text{and} \quad m_Z = \frac{v}{2} \sqrt{g'^2 + g^2}, \quad (1.38)$$

which leads them to be related by the weak mixing angle as follows:

$$m_W = m_Z \cos(\theta_w). \quad (1.39)$$

The theory also includes a massive Higgs boson through its self-coupling, where its mass term is given by

$$m_{h_0} = \sqrt{2}\mu = \frac{v\lambda}{2}. \quad (1.40)$$

1.3.4 The Yukawa sector

The Yukawa Lagrangian couples fermions with the Higgs field, generating their mass terms. This sector of the SM can be further divided into a lepton and quark part.

The leptonic part of the Yukawa Lagrangian is given by

$$\mathcal{L}_{Y\text{-leptons}} = - \sum_{i=1}^3 [y_i (l_L^i)^\dagger \Phi l_R^i + h.c.], \quad (1.41)$$

where l_L^i and l_R^i are the lepton fields, defined in Sec. 1.3.2 with the index i spanning over the three flavor families; y_i are the Yukawa coupling constants for leptons and Φ is the Higgs boson, as given in Eq. (1.32), where the prime apex has been dropped to simplify the notation.

The leptonic Yukawa interaction excludes neutrinos, which remain massless, and generates mass terms for the other leptons as

$$m_i = \frac{v}{\sqrt{2}} y_i. \quad (1.42)$$

For quarks the situation is slightly different, because their mass eigenstates do not match the gauge-bosons interaction eigenstates. This mismatch leads to a Lagrangian with non diagonal Yukawa couplings $y_{ij}^{d,u}$:

$$\mathcal{L}_{Y\text{-quarks}} = - \sum_{i,j=1}^3 [y_{ij}^d (q_L^i)^\dagger \Phi d_R^j + y_{ij}^u (q_L^i)^\dagger \Phi^c u_R^j + h.c.], \quad (1.43)$$

where Φ^c is a conjugate of the Higgs field $\Phi^c \equiv i\sigma^2 \Phi^\star$.

Φ^c is also a doublet of $SU(2)_L$, like Φ , and its corresponding term in the Lagrangian accommodates for the down-type masses.

By applying a bi-unitary transformation, the Yukawa couplings can be diagonalised and the Lagrangian can be rewritten in the mass eigenbasis. Adopting a

matrix notation consistent with Eq. (1.22), the transformation of basis can be defined as follows:

$$\begin{cases} u'_L = V_L^u u_L \\ d'_L = V_L^d d_L \end{cases} \text{ and } \begin{cases} u'_R = V_R^u u_R \\ d'_R = V_R^d d_R \end{cases}, \quad \text{with } u = \begin{pmatrix} u \\ c \\ t \end{pmatrix} \text{ and } d = \begin{pmatrix} d \\ s \\ b \end{pmatrix}, \quad (1.44)$$

where V_L^u , V_L^d , V_R^u and V_R^d are unitary matrices.

The Lagrangian expressed in the new basis becomes:

$$\mathcal{L}_{Y\text{-quarks}} = - \sum_{i=1}^3 [y_i^{d'} (q_L')^\dagger \Phi d_R'^j + y_i^{u'} (q_L')^\dagger \Phi^c u_R'^j + h.c.], \quad (1.45)$$

where the new diagonal Yukawa couplings, expressed in matrix notation to not weigh down the notation, are given by

$$Y^{d'} \equiv V_L^{d\dagger} Y^d V_R^d \text{ and } Y^{u'} \equiv V_L^{u\dagger} Y^u V_R^u. \quad (1.46)$$

The mass terms of the quarks correspond to

$$m_{d'_i} = \frac{v}{\sqrt{2}} y_i^{d'} \text{ and } m_{u'_i} = \frac{v}{\sqrt{2}} y_i^{u'}. \quad (1.47)$$

Therefore, the possibility of flavor mixing for quarks is a consequence of having a non diagonal transformation matrix between the mass eigenbasis and the interaction eigenbasis.

However, for the neutral gauge boson Z^0 , the mixing terms drop out of the equations and *flavour changing neutral currents* remain absent. While on the other hand, for *charged currents* mediated by the W^\pm bosons, a mixing matrix arises: the *Cabibbo-Kobayashi-Maskawa* (CKM) matrix.

Specifically, the quark Lagrangian for the W^\pm sector takes the following form:

$$\mathcal{L}_{cc} = -\frac{g}{2} \left[\overline{u}_L \gamma_\mu \left(V_L^{u\dagger} V_L^d \right) d_L + h.c. \right], \quad (1.48)$$

	Field	Spin	SU(3) _C	SU(2) _L	Y/2
Quarks	q_L^i	1/2	3	2	1/3
	u_r^i	1/2	3	1	4/3
	d_r^i	1/2	3	1	-2/3
Leptons	l_L^i	1/2	1	2	-1
	l_r^i	1/2	1	1	-2
Higgs doublet	Φ	0	1	2	1
Gauge bosons	G_μ^a	1	8	1	0
	W_μ^a	1	1	3	0
	B_μ	1	1	1	0

Table 1.1: Reference table for all SM fields with their notation, spin, and group representation.

leading to the following definition of the 3×3 complex unitary CKM matrix:

$$U_{\text{CKM}} \equiv V_L^{u\dagger} V_L^d = \begin{bmatrix} V_{ud} & V_{us} & V_{ub} \\ V_{cd} & V_{cs} & V_{cb} \\ V_{td} & V_{ts} & V_{tb} \end{bmatrix}, \quad (1.49)$$

where the magnitude of the elements of the matrix corresponds to the strength of that specific flavour-changing weak decay.

Because of the freedom of redefining the global phases for five out of six quark fields, the CKM matrix can be parametrised by three angles and one complex phase. The role of this complex phase is particularly important in the theory, as the fact that the CKM matrix retains its complex nature, which is strictly related to having three instead of two flavour families, accounts for a violation of the *charge parity* (CP) symmetry.

In the SM there is no flavour mixing for leptons.

For summary and reference, all fields of the SM are reported in Tab. 1.1.

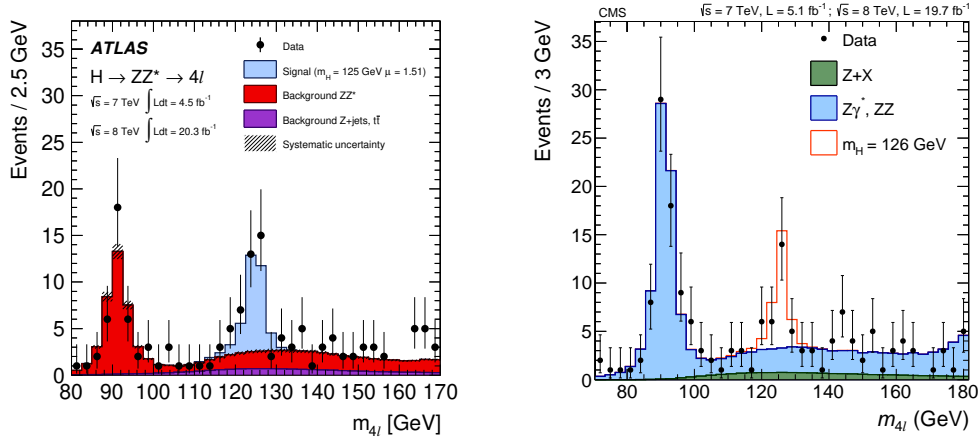


Figure 1.1: The distribution of the four-lepton invariant mass, m_{4l} , for the selected candidates, compared to the expected signal and background contributions. For the combined $\sqrt{s} = 7 \text{ TeV}$ and $\sqrt{s} = 8 \text{ TeV}$. For a mass hypothesis of (a) $m_H = 125 \text{ GeV}$ from the ATLAS experiment and (b) $m_H = 126 \text{ GeV}$ from the CMS experiment [9, 10].

1.4 Standard model achievements

Historically, the SM has been an extremely prolific source for physics research. Over the course of the years, it pointed towards the discovery of unknown particles and fundamental interactions phenomenology.

Multiple experiments have tested the SM since its first formulation in the 1960s and its validity has been confirmed by many precision measurements.

The last experimental breakthrough that completed the SM particles table was the recent discovery of the Higgs boson (Fig. 1.1) by the ATLAS and CMS collaboration at the LHC in 2012, which resulted in a Nobel prize for physics award.

The SM has also survived a variety of high precision measurements aimed at testing the consistency of this modelling theory. Fig. 1.2 shows several SM total production cross section measured by ATLAS and compared to the corresponding theoretical expectations.

Another important class of experiments related to the SM are those testing the validity of implicit assumptions within the model. Within the SM alone, there are 18¹ undetermined and independent free parameters.

One possible set of these independent parameters comprises the three coupling constants, g , g' and g_s , the Higgs VEV and self-coupling constants, v and λ ,

¹By considering the QCD vacuum angle, θ_{QCD} , the undetermined SM parameters would actually be 19. This angle has to be extremely small, but not exactly zero in order to account for CP violation in the strong interaction. [11]

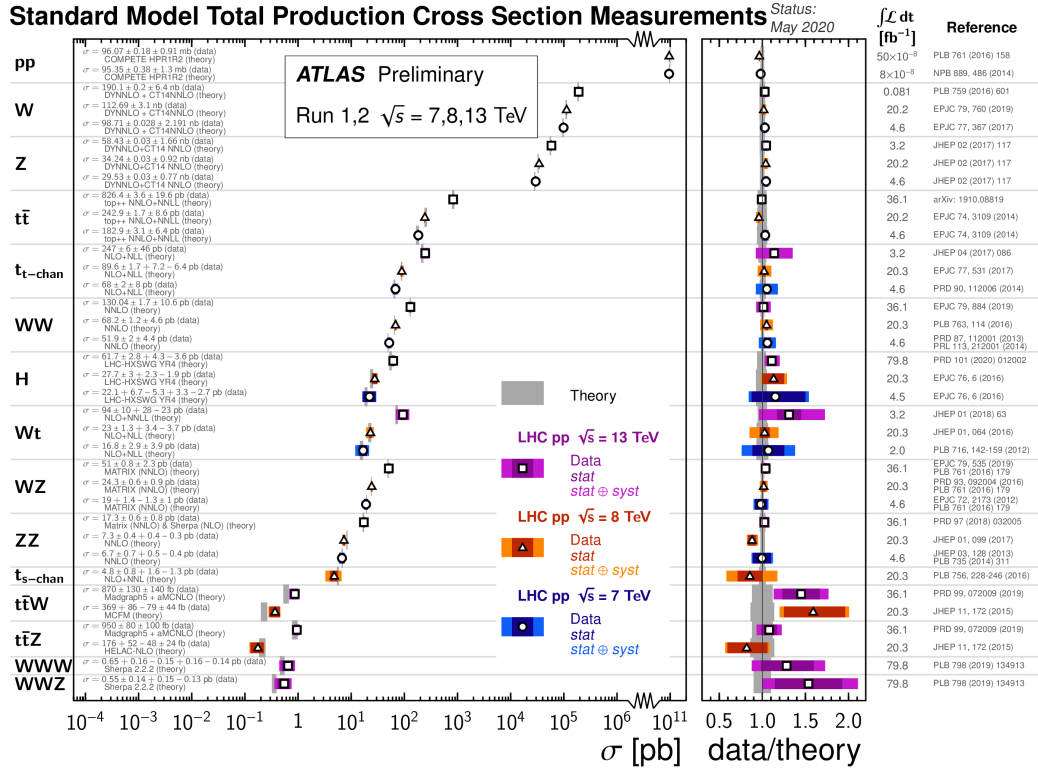


Figure 1.2: Summary of several SM total production cross section measurements, corrected for branching fractions, compared to the corresponding theoretical expectations and ratio with respect to best theory. [12].

the three angles and one complex phase of the CKM matrix, θ_{12} , θ_{23} , θ_{13} , δ_{13} ; and nine Yukawa couplings, y'_i (see Sec. 1.3.4).

Therefore, precise SM measurements are essential to extract values for these free parameters of the theory.

1.5 Standard model shortcomings

Despite the many SM theoretical predictions and experimental confirmations that have proven a great success, the model shows both conceptual and experimental deficiencies.

The SM is completely agnostic of the gravitational interaction and fails to reconcile with present gravitational theories. The SM also fails in accommodating important experimental results, e.g. neutrino masses and dark matter.

These reasons all together are a clear sign for the presence of new physics *beyond the standard model* (BSM).

1.5.1 Quantum theory of gravity

The SM is constructed on a flat spacetime and does not account for any type of gravitational interaction.

At the Planck scale $\Lambda \simeq 10 \times 10^{19}$ GeV quantum gravitational effects are expected to become relevant, but attempting to apply the usual prescriptions of quantum field theory to gravity results in a not renormalisable theory that therefore cannot be used to make meaningful physical predictions.

As a result, reconciliation of *general relativity* with quantum mechanics is seek elsewhere. Examples of these different researches are *string theory* and *loop quantum gravity*.

1.5.2 Dark matter

Various astrophysical observations indicate that 85% of the cosmological gravitational source in the known universe is likely not to be of the kind described by the SM.

In the *lambda-cold dark matter* (Λ CDM) model, which is today's standard theory in cosmology, this gravitational source is called *dark matter*. DM is called dark because it does not appear to absorb, reflect or emit electromagnetic radiation, making it therefore difficult to detect.

In the Λ CDM model the total mass-energy of the universe contains about 5% of ordinary matter and energy (described also by the SM), about 27% of dark matter and about of 68% of a form of energy called *dark energy* (DE).

Currently, the SM does not include any particle that can account for the large measured fraction of dark matter.

1.5.3 Neutrino oscillations

The SM contains three left-handed massless neutrinos, but the observation of neutrinos oscillation, which mixes neutrino flavour eigenstates with neutrino mass eigenstates, requires neutrinos to have non-zero masses.

The experimental evidence of non-zero masses for the neutrinos requires either the existence of right-handed neutrinos or that that they are Majorana particles with $\nu_L = \bar{\nu}_L$. In both cases, as a consequence of their non-zero masses, lepton numbers are violated.

1.5.4 The hierarchy problem

The naturalness or hierarchy problem represents the tension of the discrepancy between the Higgs mass scale $O(100 \text{ GeV})$ and the ultraviolet cut-off Λ_{UV}

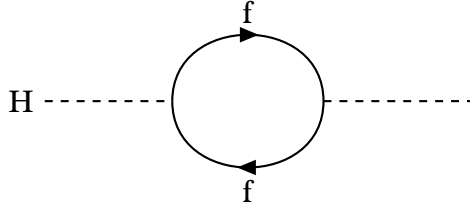


Figure 1.3: Fermion one-loop quantum correction to the Higgs propagator, which corresponds to $\Delta m_{h_0} = -\frac{\lambda_f^2}{8\pi^2} \Lambda_{UV}^2$ [13].

$O(1 \text{ TeV})$.

This is not really an issue within the SM itself as a phenomenological description of nature, but rather a disturbing sensitivity of the Higgs potential to new physics in any imaginable extension of the SM.

The presence of new physics, as so far suggested, would induce a Higgs mass correction of the order of $\Delta m_{h_0}(\Lambda_{UV}^2)$. The cancellation of this dependence in the renormalised mass is usually an indicator for the presence of a symmetry, suggesting that a new symmetry between fermions and bosons, such as *supersymmetry* (SUSY), ought to exist. Unfortunately, this symmetry has not yet been found experimentally.

1.5.5 Dark energy

Dark energy is a form of energy that affects the universe on the largest scale. As expressed in [14], DE is not much of a mystery in contemporary physics, but rather it represents yet another instance of incompatibility between the SM and the Λ CDM model.

The Λ CDM model describes DE very simply as a constant cosmological term Λ in Einstein's field equation

$$R_{\mu\nu} - \frac{1}{2}Rg_{\mu\nu} + \Lambda g_{\mu\nu} = 8\pi GT_{\mu\nu}, \quad (1.50)$$

where $R_{\mu\nu}$ and R represent the Ricci curvature tensor and scalar respectively, g is the spacetime metric, T is the stress-energy tensor and G is the universal gravitational constant.

There is currently no known way to derive the value of the cosmological constant from within the SM and the interest for exploring alternative theoretical scenarios is a current field of research in physics.

Top quark physics at the LHC

The top quark has a very high Yukawa coupling with the Higgs boson field and with a mass of $173.34 \pm 0.27(\text{stat.}) \pm 0.71(\text{syst.})$ GeV [15] it is the heaviest among the SM fundamental particles. The top quark is also significantly heavier than the bottom quark, the other quark of the same flavour family.

After the discovery of the bottom quark was experimentally confirmed in 1977, the existence of a quark with a $2/3$ charge, in the third generation was expected.

The existence of the top quark was discovered at the *FermiLab Tevatron*, a proton-antiproton ($p\bar{p}$) collider at a center-of-mass energy (\sqrt{s}) of 1.8 TeV, in 1995 by the CDF [16] and DØ [17] collaborations.

The top quark production is now studied by physics experiments at the *Large Hadron Collider* (LHC) [18] accelerator which has a high rate of top-quark production.

Contrary to the lighter quarks, which are confined in hadronic bound states, the top quark has a very short lifetime of approximately 0.5×10^{-24} s and decays before it has the possibility to hadronise. For this reason, the top quark offers a unique opportunity to study the properties of a bare quark.

In addition to SM studies, a precise understanding of the top quark signal is crucial for possible claim of new physics since the top-quark production is a background in many searches for physics beyond the SM.

2.1 The Large Hadron Collider

The *Large Hadron Collider* (LHC) is the world's largest and highest-energy particle collider. It was built by the *European Organisation for Nuclear Research* (CERN) near Geneva, approximately 100 m underground beneath the France

Switzerland border, in a circular tunnel about 27 km long. It was designed to accelerate bunches of protons and to bring them to collision at the centre of four particle detectors with a centre-of-mass energy of $\sqrt{s} = 14 \text{ TeV}$ and a luminosity of $10^{34} \text{ cm}^{-2} \text{ s}^{-1}$.

The proton beams in the LHC are made up of bunches with each one containing more than 100 billion protons. The machine is designed to support bunches which are spaced about seven metres apart from each other, corresponding to about 25 ns at the speed they are travelling. This machine parameter is called *bunch spacing*. The maximum possible number of bunches that can be reached with the beam preparation method used is 2556.

The LHC physics programme is very broad and diverse, it ranges from precise SM measurements to the search for new physics phenomena BSM.

2.1.1 Machine parameters

To quantify the production of a process, it is necessary to measure its cross-section. Classically, the cross section is a quantity describing the process of interaction between two bodies and it has the dimension of an area measured in *barn* (b).

The total inclusive cross section of a process at the LHC considers all the possible scattering processes that occur during the proton-proton collisions (Fig. 2.1). The most general cross section expression is given by

$$\sigma = \frac{N}{\varepsilon L}, \quad (2.1)$$

where N is the number of observed events corresponding to a specific process, ε is the efficiency of the detector and L is the *integrated luminosity*. L is defined as the integral of the *instantaneous luminosity* \mathcal{L} :

$$L = \int \mathcal{L} dt. \quad (2.2)$$

The generic expression of the instantaneous luminosity for two Gaussian distributed beams colliding head-on is given by

$$\mathcal{L} = \frac{1}{4\pi} \frac{N_1 N_2 N_b}{\sigma_x \sigma_y} f, \quad (2.3)$$

where N_1 and N_2 are the number of protons contained in each colliding bunch, N_b is the number of bunches, σ_x and σ_y are the Gaussian width of the protons distribution along the orthogonal axes with respect to the beam direction and f is the collision frequency.

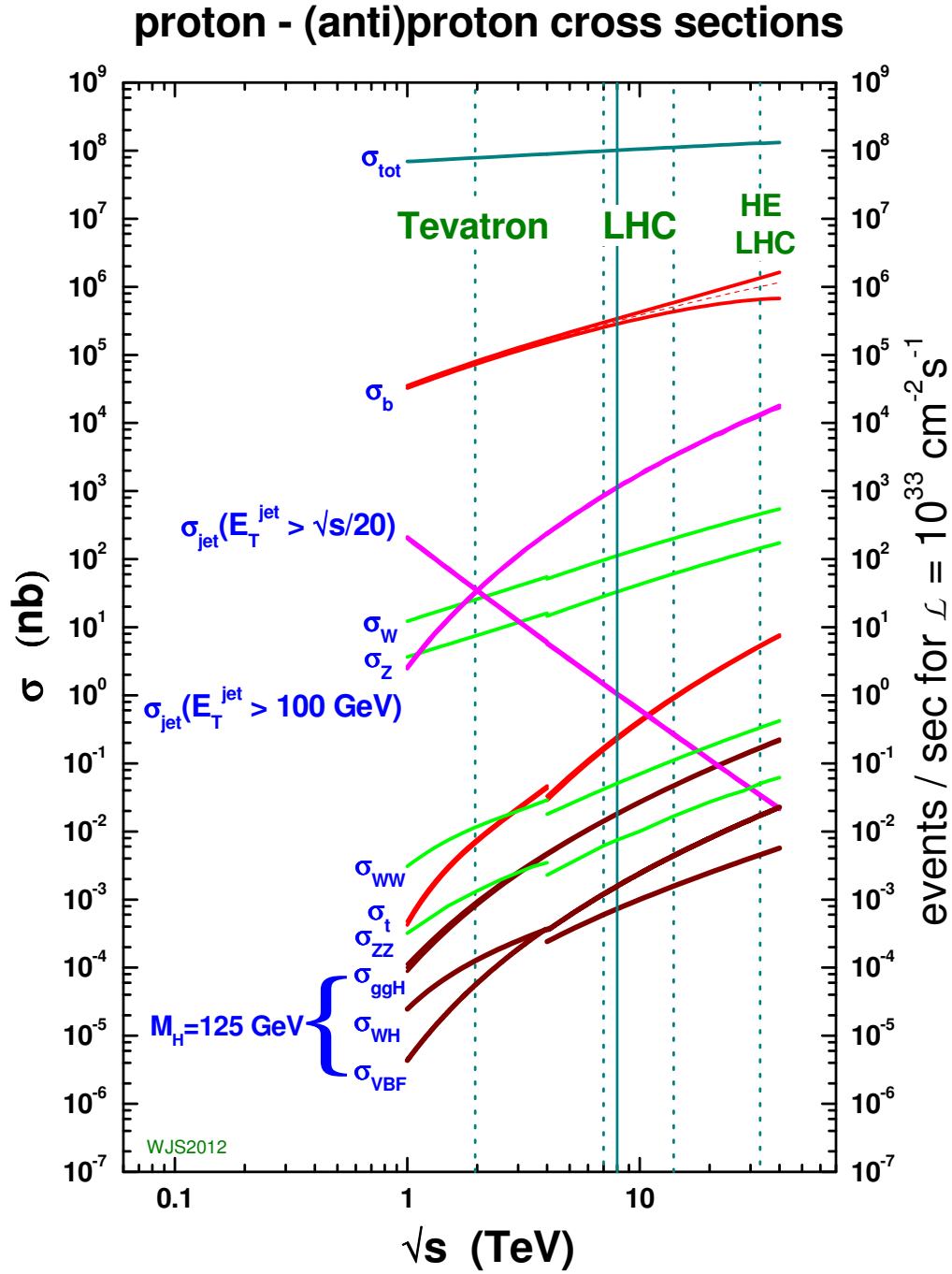


Figure 2.1: Proton-(anti)proton cross sections for various centre-of-mass energy values. Vertical lines are drawn to show the LHC at 8 TeV and 14 TeV. The discontinuity at 4 TeV is due to a switch from proton-antiproton to proton-proton. [19]

The additional proton-proton interactions in the bunch-crossing that do not produce hard scattering are called *in-time pile-up*. Usually the probability of producing more than one proton-proton collision, which generates a hard scattering event per bunch crossing is pretty low. But as the instantaneous luminosity goes up, effectively due to an increase in the density of protons in the interaction region where the beams overlap, the likelihood of interaction between the constituent quarks and gluons of additional proton-proton pairs increases.

Overlapping detector responses due to neighbouring bunch crossings interactions are instead called *out-of-time pile-up*. A distance of just 25 ns between two proton bunches is faster than the read-out response of many of the ATLAS sub-detectors, thus a crucial task of the data acquisition system is to be able to identify from which bunch crossing each particle was originated.

The generic term *pile-up* includes in-time and out-of-time effects, as well as events due to other effects such as beam halo, beam gas and cavern background.

2.1.2 The experiments at the LHC

Two experiments, ATLAS [20] and CMS [21], are general purpose detectors, designed to look for expected and unexpected physics at the highest possible energy. The LHCb [22] experiment is instead built to precisely measure the properties of B -mesons in order to investigate the nature of CP violation. The ALICE [23] experiment is designed to look at the result of heavy ions collisions, investigating the *quark gluon plasma* state of matter.

The TOTEM [24] experiment is placed on either side of the CMS detector at a distances of 147 m and 220 m, and is designed to measure the total pp cross section and to study elastic and diffractive scattering.

The LHCf [25] experiment is located on either side of the ATLAS interaction point, 140 m away. It is designed to measure the very forward production of neutral particles from pp collisions to study air shower models for cosmic ray detection.

2.2 Top quark production and decay modes

The top quark can be produced in pairs via QCD interactions and as a single particle in EW processes. The strong processes have a higher cross-section with respect to the EW production.

The production cross-section for top quarks, both in pairs and as a single quark, strongly depends on the collision energy. And as the top quark decays before

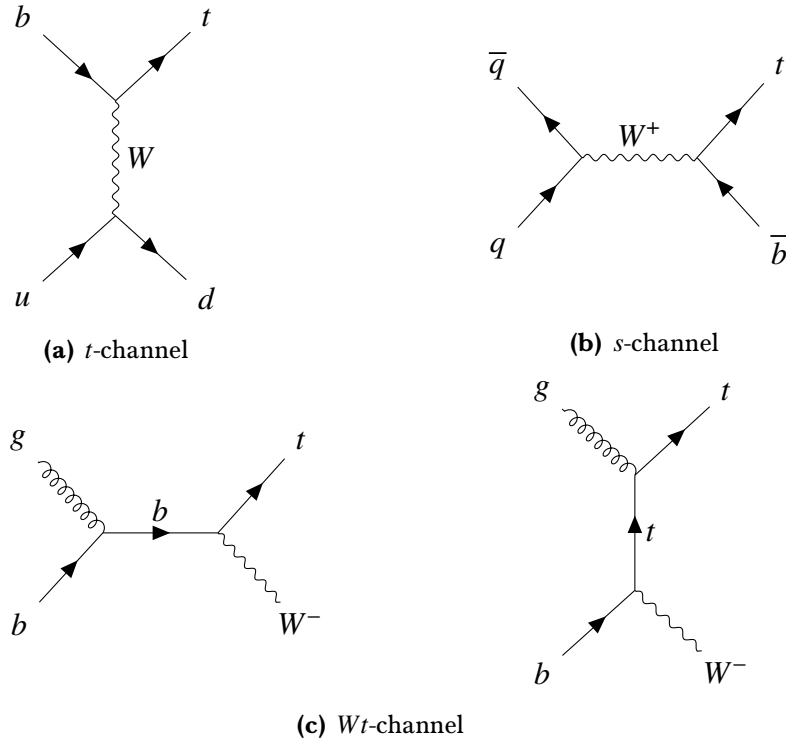


Figure 2.2: Feynman diagrams for the single-top quark production in the three different channels.

hadronising, detectors installed at particle accelerator laboratories are able to measure only its decay products.

2.2.1 Single top quark production

The single-top quark production is mediated by EW interaction and depending on the way the W boson is involved it can be categorised into three production modes: the t -channel, the s -channel and the Wt -channel.

In the t -channel, a virtual W boson converts a b -quark into a top quark. In the s -channel, a W boson is produced by the fusion of a quark-antiquark pair. In the Wt -channel, the top quark is produced in association with a real W boson.

The Feynman diagrams for the three channels are shown in Fig. 2.2.

2.2.2 Top quark decay modes

The probability for each type of the down-type quarks d_i to occur as a decay product of the top quark is given by the CKM matrix elements (Eq. (1.49)). Since the CKM element V_{tb} is close to 1, the top quark decays almost exclusively into a W boson and a bottom quark b . In terms of branching ratio this can be

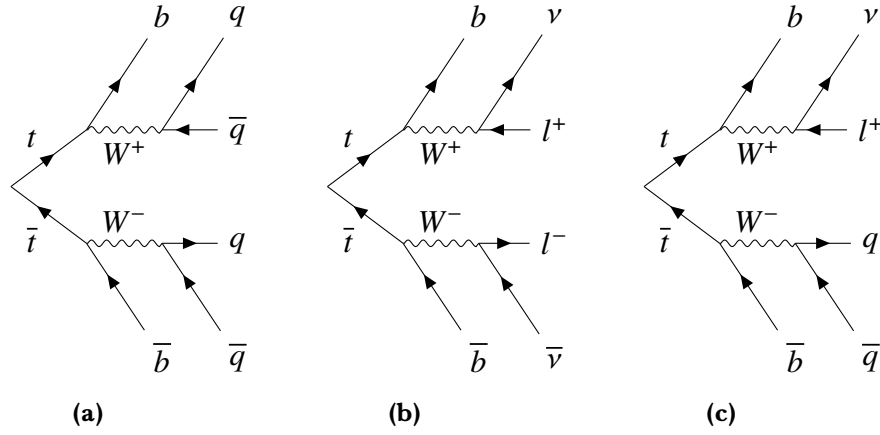


Figure 2.3: Feynman diagrams of the top quark pair decay modes for the (a) fully hadronic, (b) dilepton and (c) ℓ +jets channels.

written as

$$\frac{\mathcal{BR}(t \rightarrow Wb)}{\mathcal{BR}(t \rightarrow Wq)} = \frac{|V_{tb}|^2}{|V_{td}|^2 + |V_{ts}|^2 + |V_{tb}|^2} \approx 1. \quad (2.4)$$

The decay signatures of the top quark or the anti-top quark are categorised according to the decay modes of the W boson: either leptonic or hadronic. In the leptonic decay mode, the W boson decays into a lepton or anti-lepton and in its associated neutrino or anti-neutrino. In the hadronic decay mode, the W boson decays into a $q\bar{q}$ pair.

Analogously, the $t\bar{t}$ events are classified according to decay modes of the two W bosons, resulting in the three main decay channels.

When both W bosons decay hadronically, the event is classified as *fully hadronic*. This is the decay channel with the highest branching ratio ($\approx 46\%$).

When both W bosons decay leptonically, the event is classified as *dilepton*. This channel has the lowest branching ratio ($\approx 10\%$).

Finally, when one of the two W bosons decays leptonically while the other decays hadronically, the event is classified as *semileptonic*, often referred to as ℓ +jets.

Feynman diagrams of the three decay modes are shown in Fig. 2.3.

2.3 Top quark pair production

At *leading order* (LO), the first perturbative order of α_S , top quark pairs can be produced by either gluon-gluon fusion or $q\bar{q}$ annihilation. The Feynman diagrams for the two production modes are shown in Fig. 2.4.

At the Tevatron collider, in $p\bar{p}$ collisions, the dominant process was the $q\bar{q}$

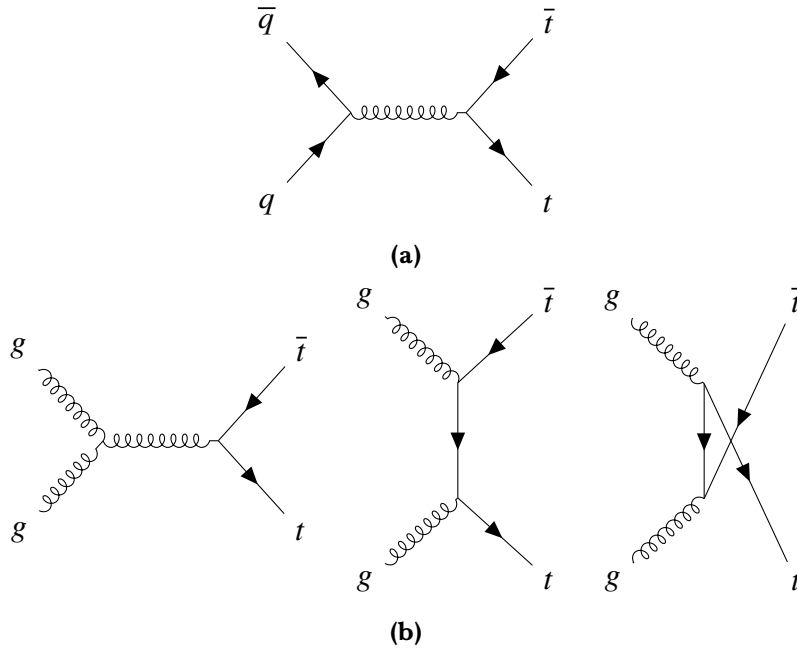


Figure 2.4: Leading order Feynman diagrams of top quark pairs production for (a) $q\bar{q}$ annihilation and (b) gluon-gluon fusion.

annihilation, whereas at the LHC, in pp collisions, the dominant production process is the gluon-gluon fusion.

At *next-to-leading order* (NLO), the second perturbative order of α_S , the processes are also a mixture of quark-gluon or antiquark-gluon.

2.3.1 Parton distribution functions

At the centre-of-mass energy reached at the LHC, quarks and gluons in the protons can be considered as quasi-free particles. Therefore, the processes involved in the pp collisions can be described in terms of interactions between the proton constituents, called *partons*.

The hard scattering process of two protons can be seen as interaction between the constituents partons of the protons, where the probability density to find a parton i inside a proton carrying a fraction x_i of the proton's momentum is described by a *parton distribution function* (PDF) $f_i(x_i, \mu_F^2)$, where μ_F is the factorisation scale, another energy scale dependence introduced by the factorisation mechanism.

The PDFs are not predicted by the theory but are determined from *deep-inelastic-scattering* (DIS) cross section measurements.

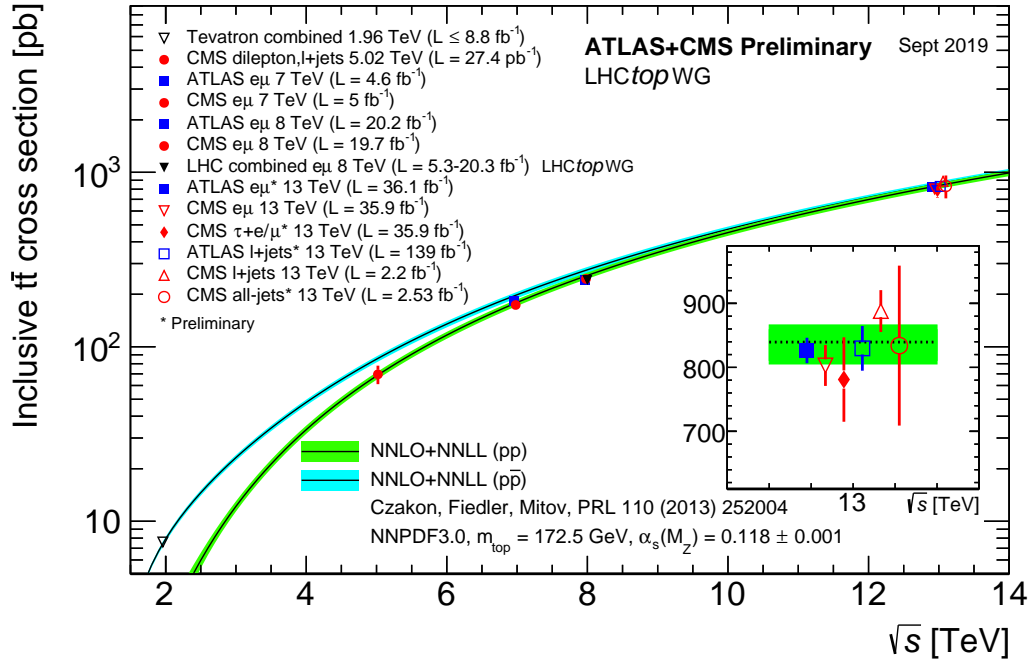


Figure 2.5: Summary of LHC and Tevatron measurements of the top-pair production cross-section as a function of the centre-of-mass energy compared to the NNLO QCD calculation complemented with NNLL resummation (top++2.0). The theory band represents uncertainties due to renormalisation and factorisation scale, parton density functions and the strong coupling. The measurements and the theory calculation are quoted at $m_{\text{top}} = 172.5 \text{ GeV}$. Measurements made at the same centre-of-mass energy are slightly offset for clarity.

2.3.2 The inclusive top-quark pair production cross section

The inclusive production cross section of the $pp \rightarrow t\bar{t}$ process can be calculated using the *factorisation theorem* [26].

The cross section convoluted with the PDFs corresponds to

$$\sigma_{pp \rightarrow t\bar{t}} = \int f_i(x_i, \mu_F^2) \int f_j(x_j, \mu_F^2) \hat{\sigma}_{ij \rightarrow t\bar{t}}(x_i, x_j, \alpha_s(\mu_R^2), \mu_F^2, \mu_R^2) dx_i dx_j, \quad (2.5)$$

where f_i and f_j are the PDFs for the two partons i and j involved in the process, $\hat{\sigma}_{ij \rightarrow t\bar{t}}$ is the partonic cross section, and μ_R and μ_F are the renormalisation and factorisation energy scales respectively. These two energy scales are generally chosen of equal values.

In Fig. 2.5 is reported a summary of the inclusive top-quark pair cross section as a function of the centre-of-mass measurements by the experiments at the LHC and Tevatron.

2.3.3 The differential cross section

The differential cross-section measurements are cross-section measurements given as a function of an observable.

The differential cross sections can be measured either at *parton level* or at *particle level*.

At the parton level, the objects considered in the measurement are taken after radiation, but before decay. At particle level, the objects are after decay, parton shower and hadronisation.

The first experimental results of differential top quark pair cross sections have been obtained at Tevatron by the CDF and DØ collaborations, as function of the $t\bar{t}$ system invariant mass [27] and of the top-quark transverse momentum [28], respectively.

Several differential cross-section measurements with an increasing amount of statistics, have been performed also by the ATLAS and CMS collaborations at a centre-of-mass energy of 7, 8 and 13 TeV in the dilepton, ℓ +jets and fully hadronic channels at both particle and parton levels.

2.4 Top-quark mass

Indirect computation of the top quark mass (m_t) derived from the computation of the W -boson mass is an important consistency test of the SM which can be obtained from precision measurements of the EW parameters.

In Fig. 2.6 are reported direct measurements of the top-quark mass, obtained by the ATLAS and CMS collaboration. The results are also compared to the LHC and Tevatron+LHC combinations.

Specifically, the mass of the W boson can also be expressed as

$$m_W^2 = \frac{\pi g / \sqrt{2} G_F}{\sin^2(\theta_W)(1 - \delta_r)}, \quad (2.6)$$

where g is the electromagnetic coupling constant, G_F is the Fermi constants, θ_W is the electroweak mixing angle and δ_r is another parameter which contains contributions from higher order electroweak loop.

The δ_r parameter depends quadratically from the mass of the top quark:

$$\delta_r = -\frac{3G_F}{8\sqrt{2}\pi^2 \tan^2(\theta_W)} m_t^2. \quad (2.7)$$

Since the expression of δ_r also contains contributions from loop diagrams in-

volving the Higgs boson, with a logarithmic dependence on the mass of the Higgs boson, it is possible to obtain direct constraints on mass of the Higgs boson from global EW fits which include direct measurements of the mass of the top quark.

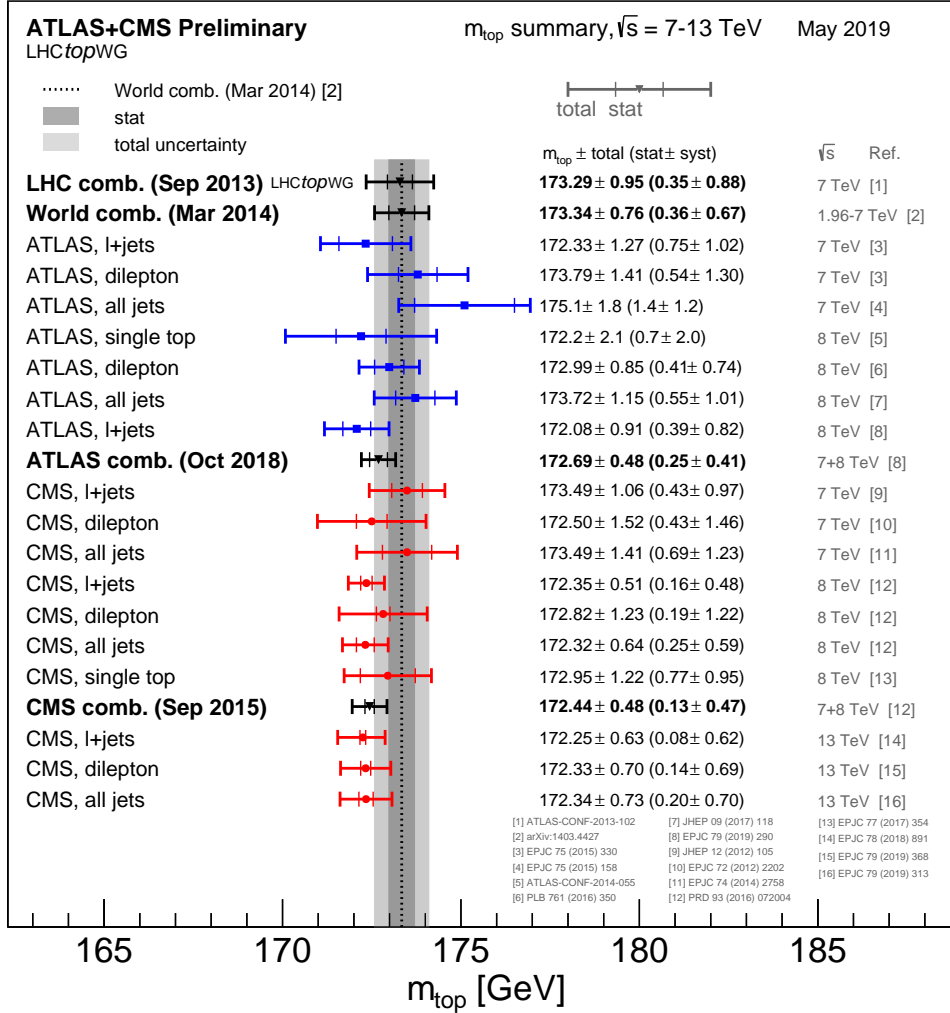


Figure 2.6: Summary of the ATLAS and CMS measurements from top quark decay. The results are compared with the LHC and Tevatron+LHC m_{top} combinations. For each measurement, the statistical uncertainty, the *jet scale factor* (JSF) and *b-jet scale factor* (bJSF) contributions (when applicable) as well as the sum of the remaining uncertainties are reported separately. The JSF, bJSF contributions are statistical in nature and apply to analyses performing in-situ (top quark pair base) jet energy calibration procedures.

The ATLAS detector

The ATLAS experiment is a general purpose detector. The detector was designed to fulfil the requirements that LHC imposes for high multiplicity and high rate of bunch crossing.

The ATLAS layout is based on the traditional onion-shell structure used in collider experiments; it is about 45 m long, more than 25 m high, and weighs about 7000 tons.

The central region of the ATLAS detector is called *barrel* due to its geometrical shape. Additional detectors are placed on both sides to provide *end-cap* coverage. This configuration makes sure that all directions around the interaction point are covered as much as possible.

Part of the detector is a toroidal magnetic system designed to bend the charged particle trajectory in order to permit measurement of their momentum.

The detector is conventionally divided into five main subdetectors. Specifically, the five subdetectors are the *inner detector* (ID), the *electromagnetic liquid argon calorimeter* (LAr), the *hadronic calorimeter* (Tile), the *muon spectrometer* (MS) and the *forward detectors* (Lucid and BCM). Figure 3.1 shows a tridimensional image of the whole apparatus and its subdetectors.

Each subdetector has a different task. The ID provides high resolution tracking and vertex reconstruction to help in the identification of long-lived particles. The calorimeter system provides energy measurement for electrons, photons and jets. It is also used for the identification of photons, electrons, muons and taus. The calorimeters provide a near hermetic coverage, allowing for a good measurement of the total and missing energy. The MS, which is the most external part of the ATLAS detector, provides triggering, identification and momentum measurement for muons. The forward detectors measure the

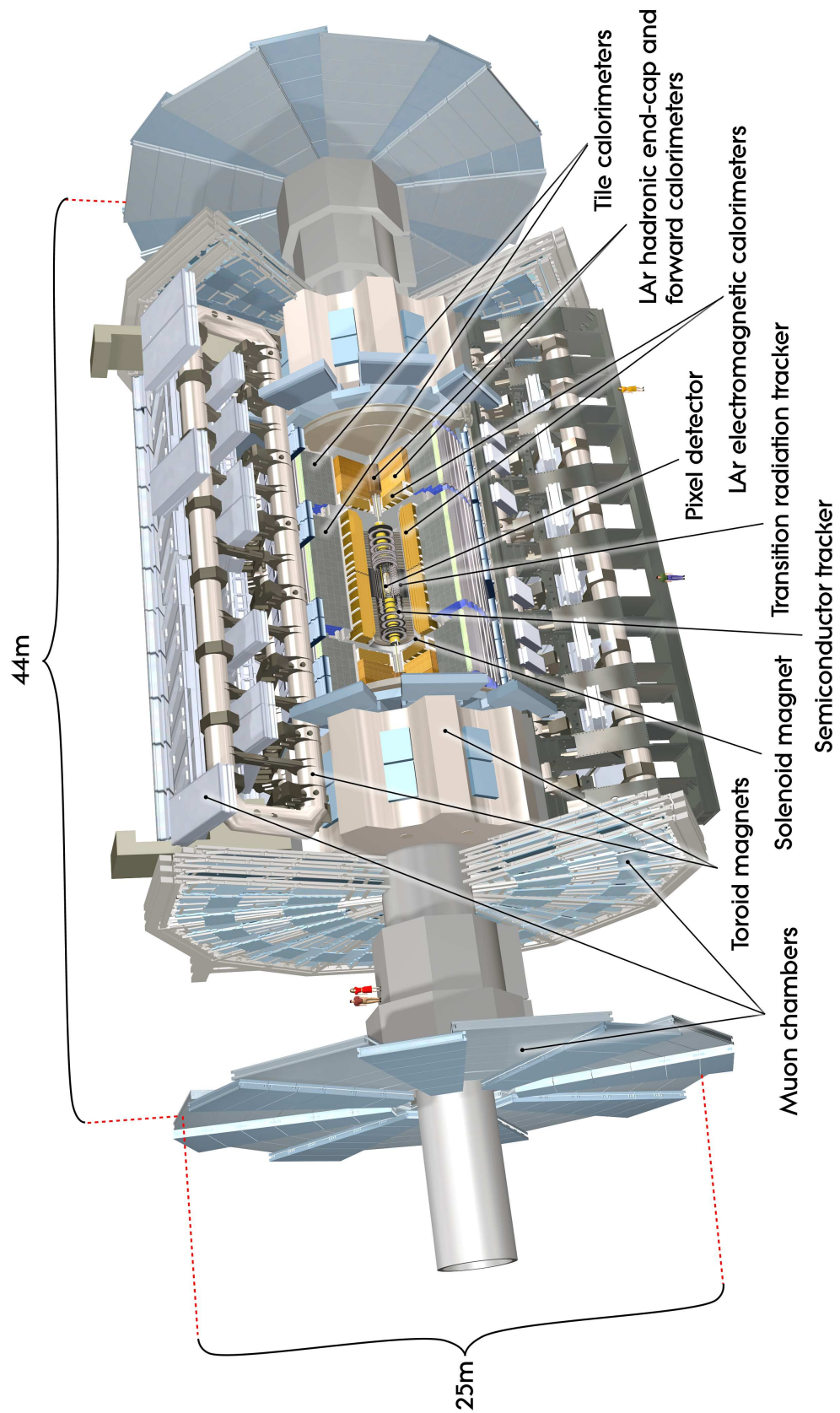


Figure 3.1: Cut-away view of the whole ATLAS detector.

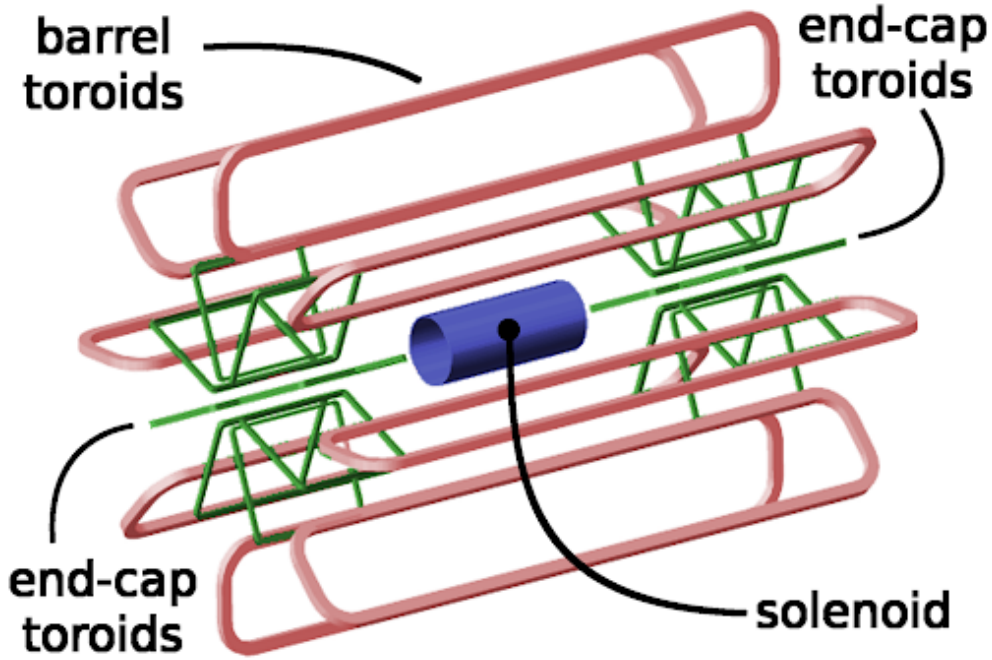


Figure 3.2: Layout of the ATLAS magnet system.

luminosity.

For each bunch crossing, all subsystems measure the outcome of the pp collision event and the data acquisition system has to handle the flow of data at the input rate of 40 MHz. Data needs to be moved reliably among the multi-level trigger system that decides which events to store for physics analysis, and which to reject and lose forever. This selection procedure is called *triggering*.

The trigger is a necessary component, due to the extremely high volume of data that would otherwise need to be stored and the limited offline analysis capabilities. Both factors pose a downstream bottleneck on the data output. For these reasons, the *trigger and data acquisition* (TDAQ) system is designed to reduce the bunch crossing rate of 40 MHz down to an output rate of about 1 kHz. With an average event size of 1.7 MB, these rates correspond to a data bandwidth reduction of about 68 TB/s down to about 1.5 GB/s.

3.1 Magnet system

The curvature of a charged particle trajectory through the detector is measured to determine its momentum. To this end, the tracking detectors are placed in a magnetic field such that the trajectory of charged particles is bent.

The ATLAS detector has a magnet system which consists of four large superconducting magnets. The ATLAS magnet system layout is shown in Fig. 3.2.

This system consists of a *solenoid*, a *barrel toroid* and two *end-cap toroids*. The solenoid is aligned on the beam axis and provides a 2 T axial magnetic field. It is placed around the ID cavity and it has a diameter of 2.4 m with a length of 5.3 m. The barrel toroid and the two end-cap toroids provides a 4 T magnetic field. The barrel toroid has an outer diameter of 20 m and a length of 25 m. The end-cap toroids have an outer diameter of 10 m and an axial length of 5 m.

3.2 Coordinate system

The coordinate system is defined as follows: the x-axis points from the interaction point to the centre of the ring, the y-axis points upwards, and the z-axis points along the beam axis.

The azimuthal angle around the beam axis is called $\phi \in (-\pi, \pi]$, while the polar angle with respect to the positive z axis is $\theta \in [0, \pi]$. However, the polar angle is usually measured in units of pseudorapidity $\eta = \log(\tan \theta/2)$.

Pseudorapidity is better suited for use in collider experiments because the density of particles coming from a collision is approximately equal per unit of η for all values of η , and moreover, $\Delta\eta$ is invariant under boosts in the z direction.

Angular distances between two objects are expressed in terms of $\Delta R = \sqrt{\Delta\phi^2 + \Delta\eta^2}$. The momentum in the plane perpendicular to the beam axis is called transverse momentum, and it is defined as: $p_T = p \sin \theta$.

3.3 Inner detector

The ID is designed to provide tracking information for charged particles and to determine the location of primary and secondary vertices. The ID is composed of three sub-detectors (Fig. 3.3, Fig. 3.4) The *pixel detector* reconstructs vertex location, the *semi conductor tracker* (SCT) provides high resolution points near the interaction region, while the *transition radiation tracker* (TRT) provides high transverse momentum resolution p_T for high p_T tracks. Overall, the ID covers a region of $|\eta| < 2.5$.

3.3.1 Pixel detector

The pixel detector consists of three layers in the barrel and three disks in each end-cap. To provide the needed granularity the pixels have a size of $50 \times 400 \mu\text{m}^2$ each, with a total active area of approximately 1.7 m^2 .

The pixel sensors are mounted on staves, which are placed in a carbon fiber frame and five mount points assure the staves position. The frame is placed

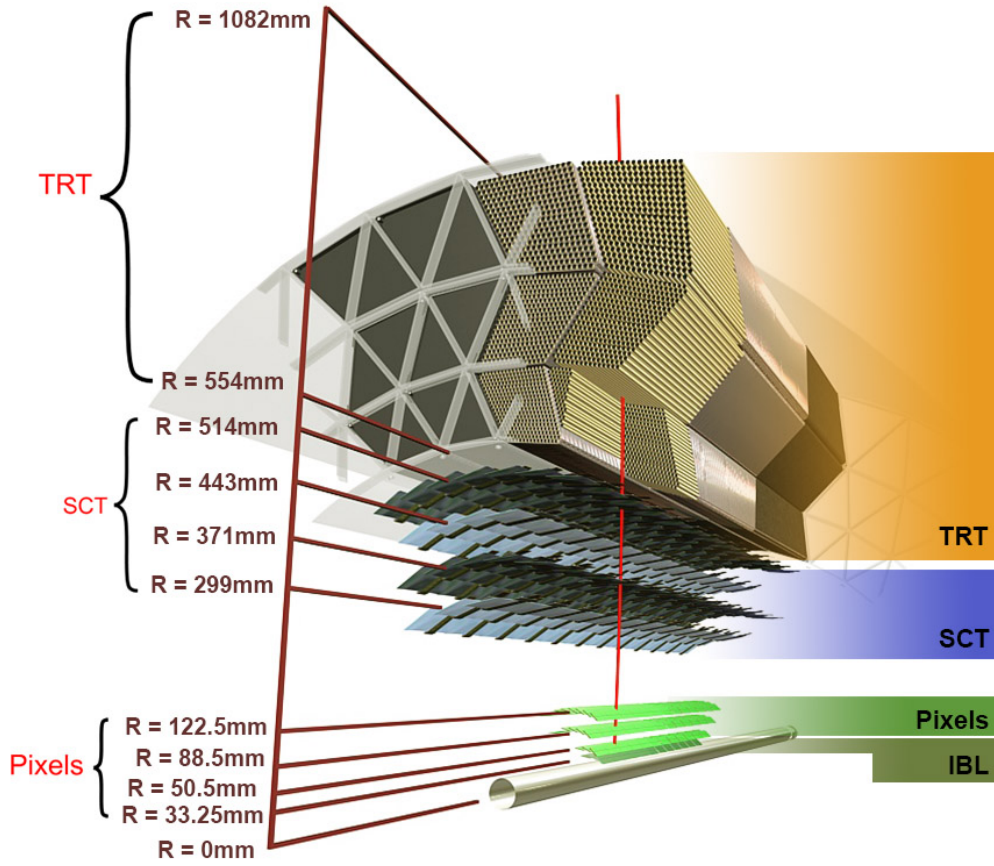


Figure 3.3: Cut-away view of the ATLAS inner detector in the barrel. [29]

inside the SCT with an accuracy of $100\ \mu\text{m}$. The alignment of pixel sensors is critical to achieve the vertex location precision needed.

Insertable B-layer

The *insertable B-layer* (IBL) was inserted at a radius of 3.3 cm between the beam line and the ID during the LHC first long shutdown between 2013 and 2015. The IBL consists of a cylindrical layer 3.5 m long.

This additional layer has increased the efficiency in reconstructing secondary vertices, essential for reconstruction of jets originating from b -quarks. It also improves tracking by providing an additional measurement point.

3.3.2 Semiconductor tracker

At larger radii pixels are no longer necessary to obtain the required granularity and SCT strip sensors are used instead. Each SCT strip is 12 cm long with an average pitch of $80\ \mu\text{m}$.

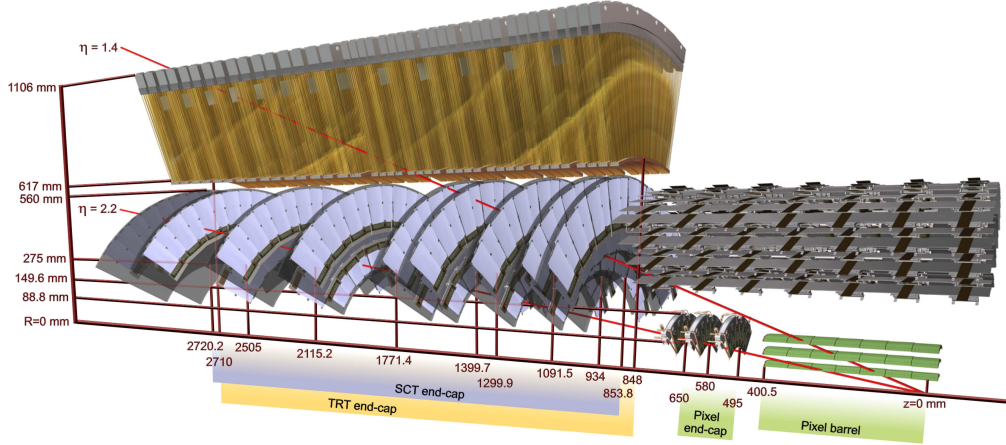


Figure 3.4: Cut-away view of the ATLAS inner detector in the end-cap.

3.3.3 Transition radiation tracker

The *transition radiation tracker* (TRT) consists of drift tubes or *straws*, with a diameter of 4 mm. The straws are 144 cm long in the barrel and 37 cm long in the end-cap. Between the straws there are transition radiation fibers that produce photons when an electron passes through. The stability is provided by carbon fibers, while the anodes are gold-plated tungsten wires. The tubes are filled with a gas mixture, and a high voltage between the tube and the wire induces an avalanche when an ionising particle traverse the tube, which can be collected and read out.

The TRT serves two functions. The first one is to measure the momentum of charged particles, and because of its large radius it can give the most accurate measurement among the ID subdetectors. For this reason the location of a traversing particle is only measured in the bending direction and the measurement has to be combined with the ones from pixel and SCT detectors that are in 3D. The second function of the TRT is to discriminate between electrons and charged pions. This is achieved by using the transition radiation emitted by electrons when traversing the TRT. Overall, the TRT provides coverage for the region $|\eta| < 2$

3.4 Calorimeter system

The ATLAS calorimeter system (Fig. 3.5) consists of electromagnetic and hadronic calorimeters. It provides precise energy measurement for photons, electrons, jets and E_T^{miss} with full ϕ coverage around the beam axis and for $|\eta| < 4.9$. The calorimeter information is also used to distinguish electrons from photons up to $|\eta| < 2.5$ (limited by the ID).

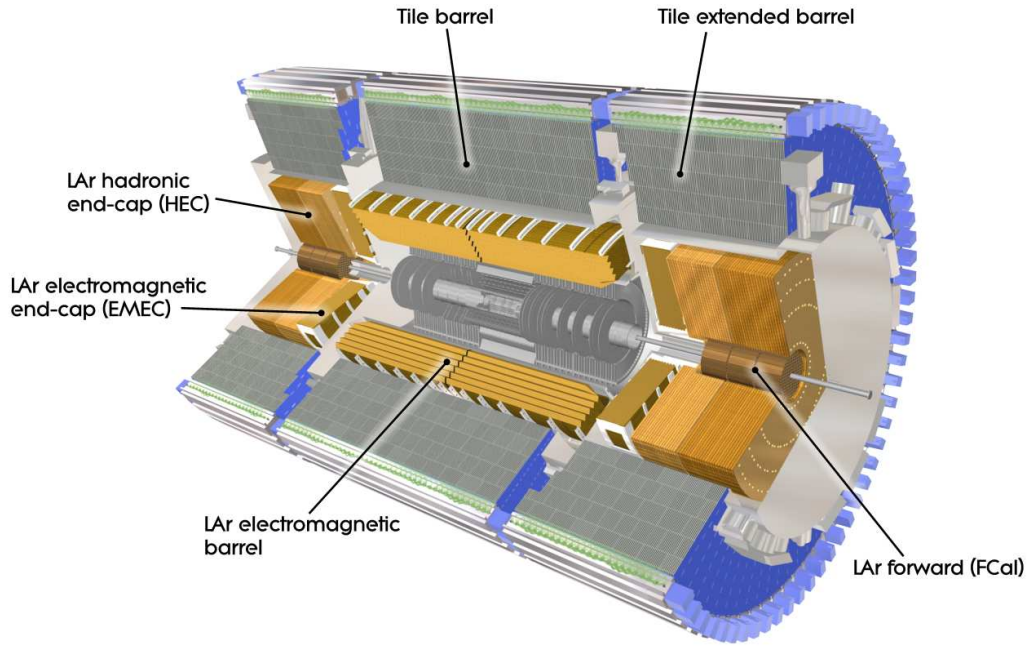


Figure 3.5: Cut-away view of the ATLAS calorimeter [30].

3.4.1 Liquid argon electromagnetic calorimeters

The *electromagnetic* (EM) calorimeter is a lead *liquid Argon* (LAr) detector. Lead absorber plates and kapton electrodes are folded in an accordion shape to provide full and homogeneous azimuthal coverage, while LAr serves as active material. In the barrel it covers $|\eta| < 1.475$ and in the end-cap for $1.375 < |\eta| < 3.2$. The barrel calorimeter is split into two identical halves separated by a 4 mm gap. Both end-cap parts share their own cryostats with the *hadronic end-cap calorimeter* (HEC) and the *forward calorimeter* (FCAL). The EM calorimeter readout is split in separate towers in η and ϕ , and each tower is also split in three layers in R with the inner layer having the finest granularity to precisely pinpoint the start of the shower (Fig. 3.6). The total thickness of the EM calorimeter is at least 22–24 times the mean radiation length X_0 ¹.

3.4.2 Liquid argon hadronic end-cap calorimeter

The HEC is a LAr and copper plate sampling calorimeter that covers $1.5 < |\eta| < 3.2$. It overlaps both the extended barrel and the FCAL providing a smooth transition with respect to the transition regions between the different calorimeter subsystems.

The HEC consists of two wheels separated longitudinally in two layers. The

¹ X_0 is the mean distance over which an electron loses e^{-1} of its energy through electromagnetic interactions.

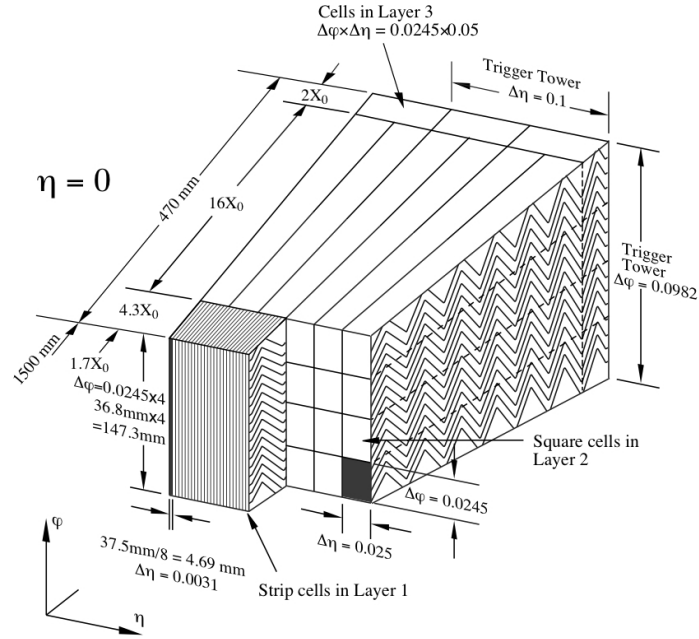


Figure 3.6: Granularity of the LAr electromagnetic calorimeter [20].

cells of the HEC have a size $\Delta\eta \times \Delta\phi = 0.1 \times 0.1$ for the inner layers, and 0.2×0.2 for the outer layers.

3.4.3 Tile calorimeter

The *tile calorimeter* (TileCAL) is the hadronic barrel calorimeter. It is made of steel absorber plates interleaved with scintillator plates as active material. It has three radial layers with coarser granularity in η with increasing radius, and 64 modules in the azimuthal direction.

The total thickness of the detector 9.7 times the nuclear interaction length λ^2 .

TileCAL covers $|\eta| < 1$ for the barrel and $0.8 < |\eta| < 1.7$ for the extended barrel.

3.4.4 Forward calorimeter

The FCAL is housed in the same cryostat as the end-cap LAr calorimeters and provides the required E_{miss}^T measurement by closing the $|\eta| < 4.9$ coverage. The FCAL front is placed about 1.2m further back with respect to the other end-cap calorimeters in order to reduce the neutron background.

The FCAL is divided in three parts. LAr is the active material in all three

² λ is the mean distance over which an hadronic particle loses e^{-1} of its energy through nuclear interactions.

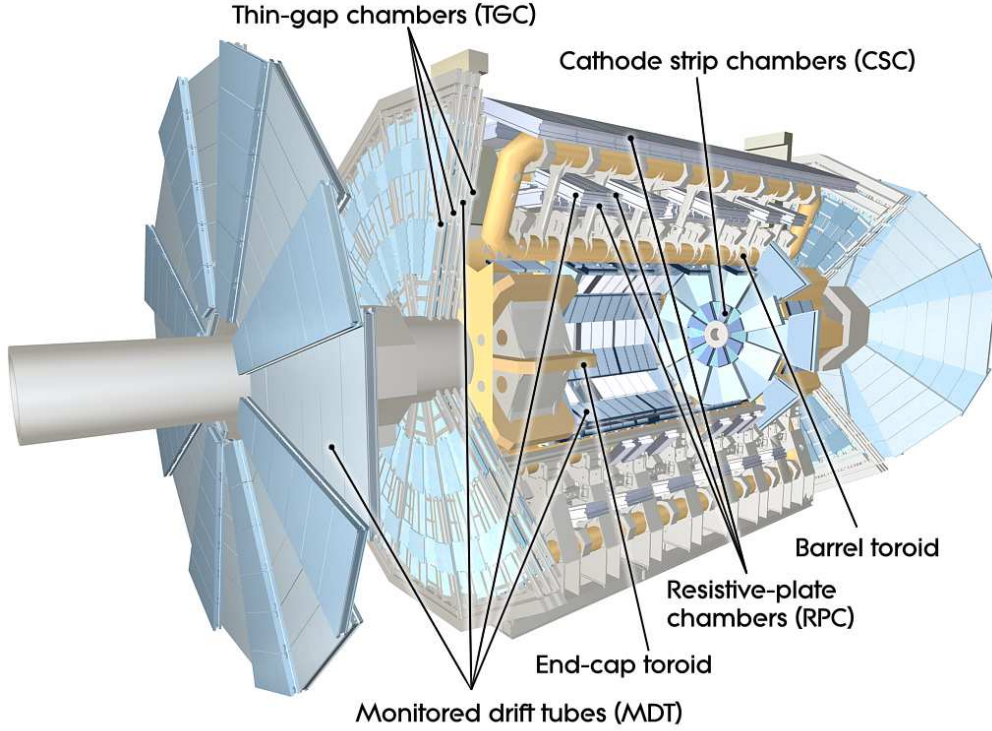


Figure 3.7: Cut-away view of the ATLAS muon spectrometer system.

parts. In the first part the absorber is made with copper for electromagnetic measurement, while in the other two parts tungsten is used as absorber, forming the hadronic part of the FCAL. The FCAL geometry allows for very small gaps (down to 0.25 mm), which avoid ion buildup in the active region of this high-radiation environment.

3.5 Muon spectrometer

The outer layers of ATLAS are formed by the MS (Fig. 3.7). The spectrometer uses four different technologies. The *monitored drift tubes* (MDT) provide precision measurement in the bending η direction for the barrel and a large part of the end-cap, covering $0 < |\eta| < 2.7$.

In the inner layers of the end-cap the radiation levels and occupancy would be too large for the MDT, therefore precision tracking is provided by *cathode strip chambers* (CSC). *Thin gap chambers* (TGC) and *resistive plate chambers* (RPC) provide a fast signal, which is used for triggering and for bunch crossing identification. They also provide a measurement of the second coordinate perpendicular to the bending direction.

The large air-core toroid magnets provides the field in the barrel ($|\eta| < 1.4$). In the end-caps ($1.6 < |\eta| < 2.7$) there is an end-cap toroid magnet and in the

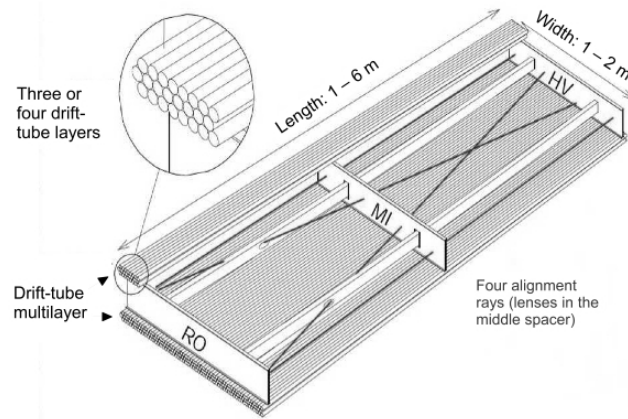


Figure 3.8: Schematic of an MDT chamber.

transition region ($1.4 < |\eta| < 1.6$) a combination of barrel and end-cap toroid magnetic field ensures enough bending power for the muons.

The deflection of the muon trajectories in the magnetic field is measured via hits in three layers of precision drift tube (MDT) chambers for $|\eta| < 2$. In η region of $2.0 < |\eta| < 2.7$, two layers of MDT chambers in combination with one layer of CSC are used. Three layers of RPC in the barrel region ($|\eta| < 1.05$) and three layers of TGC in the end-cap regions ($1.05 < |\eta| < 2.4$) provide the L1 muon trigger.

The limited geometric coverage in the barrel region is due to an opening around $\eta = 0$ to provide space for services of the ID and the calorimeters, the feet and rib support structures of the ATLAS detector, and two small elevators in the bottom part of the spectrometer.

3.5.1 Monitored drift tubes

The MDT tubes are made of aluminium with Ar/CO₂ gas inside, which gets ionised by the passage of the muons. The electrons from this ionisation drift onto the 50 μm thick tungsten/rhenium wire. A high voltage between the wire and the tube wall induces an avalanche close to the wire that amplifies the signal.

The MDT provides a measure of the distance of closest approach of the muon track to the wire by measuring the drift time of electrons. Because the maximum drift time (700 ns) is much higher than the bunch crossing, MDT trigger chambers have an important role in bunch crossing identification. They measure the angular location and provide a time-stamp for each bunch crossing.

One MDT chamber (Fig. 3.8) has two multi-layers separated by a spacer that provides mounting points for high-voltage supplies, readout electronics and B-field sensors. Each multi-layer contains three tubes layers for the outer and

middle detector shells, and four tube layers for the inner shell of the detector.

Each chamber also has an optical alignment system that monitors deformations of the chamber due to thermal variations and magnetic field.

3.5.2 Cathode strip chambers

In the very forward regions $2 < |\eta| < 2.7$ in the inner layer of the spectrometer the MDTs are replaced by CSCs. In this region the hit rate would exceed the level where safe and durable operation for MDTs can be guaranteed. CSC are multi-wire proportional chambers that are read out through segmented cathodes.

The wires are oriented in the radial direction and perpendicular to the wires, there are finely segmented cathode strips that provide the precision measurement in the bending plane. In the second cathode plane the strips, oriented parallel to the wires, provide the second coordinate measurement and a fast signal for bunch crossing identification.

The CSCs are placed in two separate disks. One disk has eight large chambers, while the other has eight small ones. The disks are placed to allow the chambers of one disk to fill the gaps with a small overlap.

The chambers are tilted towards the interaction point to make sure that tracks are perpendicular to the chamber plates, because inclined tracks would reduce the spatial resolution of the chambers. The CSC have a resolution of $60\ \mu\text{m}$ per layer in the bending plane and $5\ \text{mm}$ in the other plane.

3.5.3 Resistive plate chambers

The MDTs and CSCs provide a precise measurement of a track in the bending direction, which results in a precise measurement of muon p_T . The RPCs instead provide the trigger for a muon based on its p_T in the barrel. RPCs are mounted on MDT chambers in three concentric circles.

There are two inner layers around the MDT middle layer and one outer layer mounted on the outside of the MDT large chambers. The level-1 trigger requires a coincidence in inner layers for low- p_T and a third coincidence in the outer layer for high p_T .

Each RPC chamber has two active gas volumes with a read-out made of two plates with orthogonal strips measuring both coordinates. The gas volume is delimited by two resistive plates kept at high-voltage and ground potential by two graphite electrodes. An ionising particle passing through causes an avalanche in the high potential gradient.

3.5.4 Thin gap chambers

TGCs consists of two layers mounted near the CSCs and MDTs inner layer in the end-cap. TGCs provide a finer granularity for track reconstruction, which is necessary for the lower bending radius of muons in the end-cap compared to muons in the barrel at the same p_T .

TGCs are multiwire proportional chamber with a gap between the wires and the cathodes that is smaller than the gap between the wires (1.4 mm and 1.8 mm respectively). The small gap has a short drift time and therefore a small response time is needed for the trigger system.

The chambers are placed with an angle that prevents tracks from passing exactly perpendicular between two wires, where the field gradient is small and long drift times would occur. The wires are read out to provide measurement in the η direction, while cathode strips provide the measurement for the other coordinate.

The coincidence trigger requires three out of four layers of the two doublets or two out of three layers of the triplet modules. In such case, data is then sent to a coincidence matrix which looks for patterns corresponding to muon tracks above a certain threshold.

The ATLAS trigger and data acquisition system

The ATLAS TDAQ system is responsible for collecting and processing the signals generated by the whole detector. It has to perform a large reduction of unwanted high-rate processes, selecting only those events of potential interest for further analysis (Fig. 2.1).

The trigger part of the system is the component that rapidly decides whether to accept or reject a physics event. It is important for the trigger to keep a high efficiency for the desired physics since rejected events are lost forever. In addition, the data acquisition system reliably collects and encodes the detector data for trigger processing and ultimately delivers the accepted events to permanent storage.

4.1 System characterisation

The TDAQ system faces many physics and technological challenges in coping with the demanding LHC parameters (Sec. 2.1.1). The pile-up, which is expected to increase in the course of the years to reach higher luminosity, can have a non-linear impact on the trigger decision time. A bunch spacing of 25 ns fixes the input working point of the TDAQ system at a data volume rate of 60 TB/s. However, the system is limited on the output by a finite storage capacity and the offline computing model. It is simply not feasible to store all the data produced by the detector and there is no point in storing more data than it could ever be possible to analyse. The ATLAS experiment already delivers to permanent storage around 10 PB of data per year. All these limitation factors translate into strict boundaries for the trigger and DAQ system.

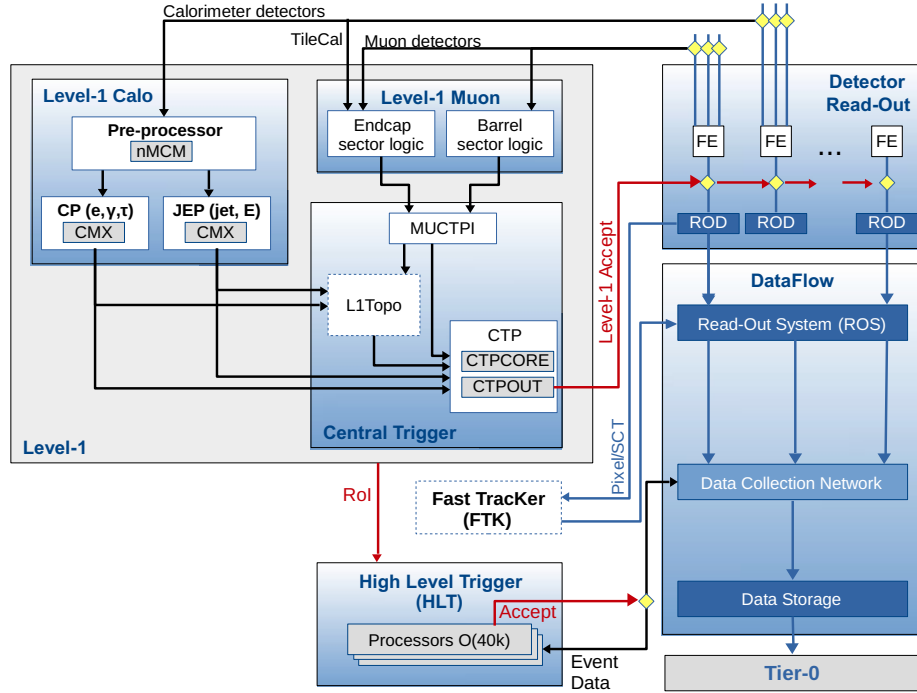


Figure 4.1: Architecture of the Run-2 ATLAS data acquisition system [31].

4.1.1 Multi-layered trigger system

In order to simultaneously meet the physics requirement of high selection efficiency and high background rejection, the ATLAS TDAQ system follows a multi-layered design (Fig. 4.1).

The first level, *level-1* (L1), is based on custom made electronics. It operates at a short fix latency of $2.5\mu\text{s}$ in order to maintain a high efficiency, and it reduces the input event rate of 40 MHz down to 100 kHz. The L1 can only perform a selection based on rough and simple criteria, but is still able to reach a very strong background rejection. The L1 also assembles the triggering data, identifying a *region of interest* (RoI) for each event, that is fed into the next trigger layer.

A fine-grained selection follows in the *High Level Trigger* (HLT), which is software based and implemented on a commodity computing cluster counting more than 2000 machines. The HLT receives an input rate close to 100 kHz from the L1 and performs slower, but more elaborate, selection algorithms. Unlike the L1, the HLT is not bounded by a maximum latency but by a targeted DAQ-BW value of 1.5 GB/s, which for an event size of 1.5 MB corresponds to an average output rate of about 1000 Hz.

Trigger	Typical offline selection	Trigger Selection		Level-1 Peak Rate (kHz)	HLT Peak Rate (Hz)
		Level-1 (GeV)	HLT (GeV)	$L = 1.7 \times 10^{34} \text{ cm}^{-2} \text{ s}^{-1}$	
Single leptons	Single isolated μ , $p_T > 27 \text{ GeV}$	20	26 (i)	15	180
	Single isolated tight e , $p_T > 27 \text{ GeV}$	22 (i)	26 (i)	28	180
	Single μ , $p_T > 52 \text{ GeV}$	20	50	15	61
	Single e , $p_T > 61 \text{ GeV}$	22 (i)	60	28	18
	Single τ , $p_T > 170 \text{ GeV}$	100	160	1.2	47
Two leptons	Two μ , each $p_T > 15 \text{ GeV}$	2×10	2×14	1.8	26
	Two μ , $p_T > 23.9 \text{ GeV}$	20	22, 8	15	42
	Two very loose e , each $p_T > 18 \text{ GeV}$	2×15 (i)	2×17	1.7	12
	One e & one μ , $p_T > 8, 25 \text{ GeV}$	20 (μ)	7, 24	15	5
	One e & one μ , $p_T > 18, 15 \text{ GeV}$	15, 10	17, 14	2.0	4
	One e & one μ , $p_T > 27, 9 \text{ GeV}$	22 (e, i)	26, 8	28	3
	Two τ , $p_T > 40, 30 \text{ GeV}$	20 (i), 12 (i) (+jets, topo)	35, 25	5	61
	One τ & one isolated μ , $p_T > 30, 15 \text{ GeV}$	12 (i), 10 (+jets)	25, 14 (i)	2.1	10
	One τ & one isolated e , $p_T > 30, 18 \text{ GeV}$	12 (i), 15 (i) (+jets)	25, 17 (i)	4	15
	Three loose e , $p_T > 25, 13, 13 \text{ GeV}$	$20, 2 \times 10$	$24, 2 \times 12$	1.3	< 0.1
Three leptons	Three μ , each $p_T > 7 \text{ GeV}$	3×6	3×6	0.2	6
	Three μ , $p_T > 21, 2 \times 5 \text{ GeV}$	20	$20, 2 \times 4$	15	8
	Two μ & one loose e , $p_T > 2 \times 11, 13 \text{ GeV}$	2×10 (μ)	$2 \times 10, 12$	1.8	0.3
	Two loose e & one μ , $p_T > 2 \times 13, 11 \text{ GeV}$	$2 \times 8, 10$	$2 \times 12, 10$	1.7	0.1
	One loose γ , $p_T > 145 \text{ GeV}$	22 (i)	140	28	43
Two photons	Two loose γ , $p_T > 55, 55 \text{ GeV}$	2×20	50, 50	2.6	6
	Two medium γ , $p_T > 40, 30 \text{ GeV}$	2×20	35, 25	2.6	17
Single jet	Jet ($R = 0.4$), $p_T > 435 \text{ GeV}$	100	420	3.3	33
	Jet ($R = 1.0$), $p_T > 480 \text{ GeV}$	100	460	3.3	24
	Jet ($R = 1.0$), $p_T > 450 \text{ GeV}$, $m_{\text{jet}} > 50 \text{ GeV}$	100	$420, m_{\text{jet}} > 40$	3.3	29
E_T^{miss}	$E_T^{\text{miss}} > 200 \text{ GeV}$	50	110	5	110
Multi-jets	Four jets, each $p_T > 125 \text{ GeV}$	3×50	4×115	0.5	16
	Five jets, each $p_T > 95 \text{ GeV}$	4×15	5×85	5	10
	Six jets, each $p_T > 80 \text{ GeV}$	4×15	6×70	5	4
	Six jets, each $p_T > 60 \text{ GeV}$, $ \eta < 2.0$	4×15	$6 \times 55, \eta < 2.4$	5	15
b -jets	One b ($\epsilon = 40\%$), $p_T > 235 \text{ GeV}$	100	225	3.3	15
	Two b ($\epsilon = 60\%$), $p_T > 185, 70 \text{ GeV}$	100	175, 60	3.3	12
	One b ($\epsilon = 40\%$) & three jets, each $p_T > 85 \text{ GeV}$	4×15	4×75	5	15
	Two b ($\epsilon = 70\%$) & one jet, $p_T > 65, 65, 160 \text{ GeV}$	$2 \times 30, 85$	$2 \times 55, 150$	1.2	15
	Two b ($\epsilon = 60\%$) & two jets, each $p_T > 65 \text{ GeV}$	$4 \times 15, \eta < 2.5$	4×55	3.2	13
B -Physics	Two μ , $p_T > 11, 6 \text{ GeV}$	11, 6	11, 6 (di- μ)	2.5	47
	Two μ , $p_T > 6, 6 \text{ GeV}$, $2.5 < m(\mu, \mu) < 4.0 \text{ GeV}$	2×6 (J/ψ , topo)	2×6 (J/ψ)	1.6	48
	Two μ , $p_T > 6, 6 \text{ GeV}$, $4.7 < m(\mu, \mu) < 5.9 \text{ GeV}$	2×6 (B , topo)	2×6 (B)	1.6	5
	Two μ , $p_T > 6, 6 \text{ GeV}$, $7 < m(\mu, \mu) < 12 \text{ GeV}$	2×6 (Υ , topo)	2×6 (Υ)	1.4	10
Total Rate				85	1550

Table 4.1: The main ATLAS triggers used for data-taking with peak luminosity $L = 1.7 \times 10^{34} \text{ cm}^{-2} \text{ s}^{-1}$. The total rate corresponds to the full menu that includes more triggers than the one showed in this table. The typical offline selections are only indicative [32].

4.2 Trigger menu

The ATLAS trigger system selects events according to a trigger menu, which defines a list of selection criteria encoded into specific trigger items. The trigger menu has to maximise the physics output of the experiment and to fit within the rate and bandwidth constraints of the ATLAS detector, TDAQ system and offline computing.

The composition and trigger thresholds are optimised for several luminosity ranges, but to ensure an optimal trigger menu within the rate constraints for a given LHC luminosity, prescale factors can be applied to L1 and HLT triggers and changed during data-taking. In this way triggers can be disabled or only a specific fraction of events can be accepted.

The menu covers a wide range of items for different purposes. In Tab. 4.1 are reported the main menu items used at a luminosity of $1.7 \times 10^{34} \text{ cm}^{-2} \text{ s}^{-1}$. *Primary* triggers are used for physics analysis covering all signatures relevant to the ATLAS physics programme, which ranges for SM precision measurements to BSM searches. Primary triggers are usually unprescaled and include electrons, photons, muons, tau leptons, (b)-jets and E_T^{miss} .

Support triggers are used for efficiency and performance measurements or for monitoring. They usually operate at a very small rate of ~ 0.5 Hz each.

Alternative triggers in the menu are used to compare new or experimental algorithms with the primary or support triggers. *Backup* triggers are switched on in case of emergency. They are set to perform very tight selections and therefore operate at a very low rate.

Calibration triggers are used to acquire information needed for detector calibration. They are usually operated on specific calibration runs and produce a high rate of very small events, where only a fraction of the whole ATLAS detector data is stored.

Naming convention

Trigger names follow the convention to start with the trigger level, L1 or HLT, and L1 items are written in upper case, while HLT items are written in lower case and the prefix HLT is often omitted for brevity. It then follows the particle multiplicity with the particle type with the following convention: g for photon, j for jet, xe for E_T^{miss} and te for $\sum E_T$ triggers. After it follows the p_T threshold in GeV. A few examples are:

- L1_2MU15, which requires at the L1 at least two muons with $p_T > 15$ GeV each;
- HLT_mu40, which requires at the HLT at least one muon with $p_T > 40$ GeV;
- HLT_6j45_0eta240, which requires six jets with $p_T > 45$ GeV and $0 < |\eta| < 2.4$.

Each HLT trigger is configured with an L1 trigger as its seed, but the L1 seed is usually not explicitly part of the trigger name. When it is necessary to distinguish between two HLT trigger items with different L1 seed, the L1 seed is added as a suffix. As shown in the following two examples.

- In HLT_mu20 it is implied that is seeded by L1_MU20.
- While HLT_mu20_L1MU15 is an alternative HLT trigger seeded by L1_MU15.

Further selection criteria, like the type of identification, isolation, reconstruction algorithm and the geometrical region are suffixed to the trigger name. For example:

- HLT_g120_loose requires a photon with $p_T > 120$ GeV and loose identification.

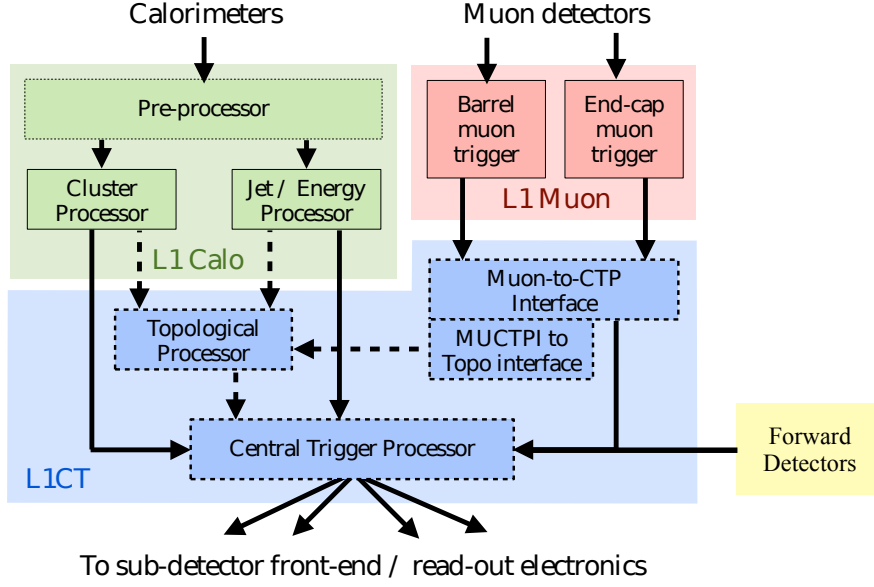


Figure 4.2: Schematic overview of the L1 trigger system. The Central Trigger combines inputs from L1Calo and L1Muon to produce a trigger decision [33].

4.3 Level-1

The L1 trigger uses coarse information from the calorimeter and muon spectrometer to perform the first selection. In particular, it looks for indications of jets, electrons, muons, photons or hadronic taus with large E_T , for events with a large total E_T summed over all calorimeter cells and for events with a large E_T^{miss} . Trigger result bits from the different L1 subsystems (Fig. 4.2) are received and combined in the *central trigger processor* (CTP) producing a *level-1 accept* (L1A): a logical signal to initiate readout of the selected events.

4.3.1 Level-1 calorimeter trigger

The *level-1 calorimeter* (L1Calo) [34] trigger provides clusters, jet multiplicities, E_T and E_T^{miss} , as well as dedicated tau triggers. It receives and processes analogue tower sums from the EM and hadronic calorimeters. In the *pre-processor* subsystem, these sums are digitised and processed to provide calibrated E_T , which is then transmitted to the *cluster processor* (CP) and the *jet-energy processor* (JEP) subsystems [35].

With sliding window algorithms the CP identifies electron, photon and tau lepton candidates with E_T above a programmable threshold and satisfying, if required, certain isolation criteria. The JEP receives 0.2×0.2 sums in $\eta \times \phi$ jet trigger elements and uses these to identify jets and to produce global sums of scalar and missing transverse momentum. Upon L1A, the coordinates and

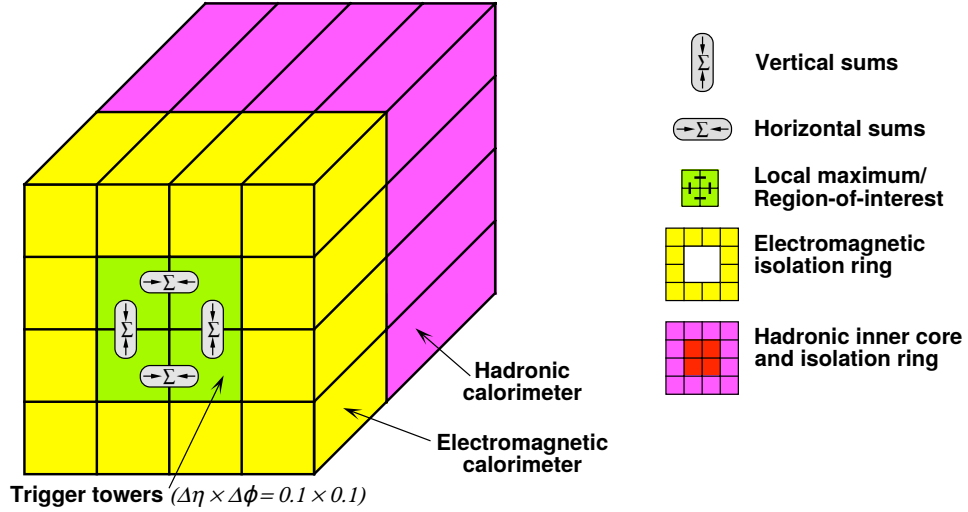


Figure 4.3: Schematic view of the trigger towers used as input to the L1Calo trigger algorithms [34].

thresholds of the identified candidates are passed as RoI.

The RoI identified by electron, photon and tau trigger algorithms, consists in a 2×2 trigger tower cluster in the electromagnetic calorimeter for which the sum of the transverse energy from at least one of the four possible pairs of nearest neighbour towers exceeds a predefined threshold (Fig. 4.3). Isolation veto thresholds can be set for the electromagnetic isolation ring in the EM calorimeter, as well as for hadronic tower sums in a central 2×2 core. The E_T threshold can be set differently for different η regions with a granularity of 0.1 in η in order to correct for fluctuating detector energy responses. The energy response of the trigger towers is calibrated at the *electromagnetic energy scale* (EM scale), i.e. it reproduces the energy deposited by particles in an electromagnetic shower in the calorimeter. On the other side, the EM scale underestimates the energy deposited by hadrons, which will later need to be re-calibrated.

Jet RoIs are defined as 4×2 or 8×8 trigger towers cluster for which the summed electromagnetic and hadronic transverse energy exceeds predefined thresholds, and they must also surround a 2×2 trigger tower core that is a local maximum. The coordinates of the jet RoI is also defined by the location of this local maximum.

4.3.2 Level-1 muon trigger

Muon triggers are based on hits information from a combination of subsystems in the MS (Sec. 3.5), only the inner most layers of TGCs are not used. The total geometric coverage of the L1 trigger is about 99% in the end-cap regions and about 80% in the barrel region.

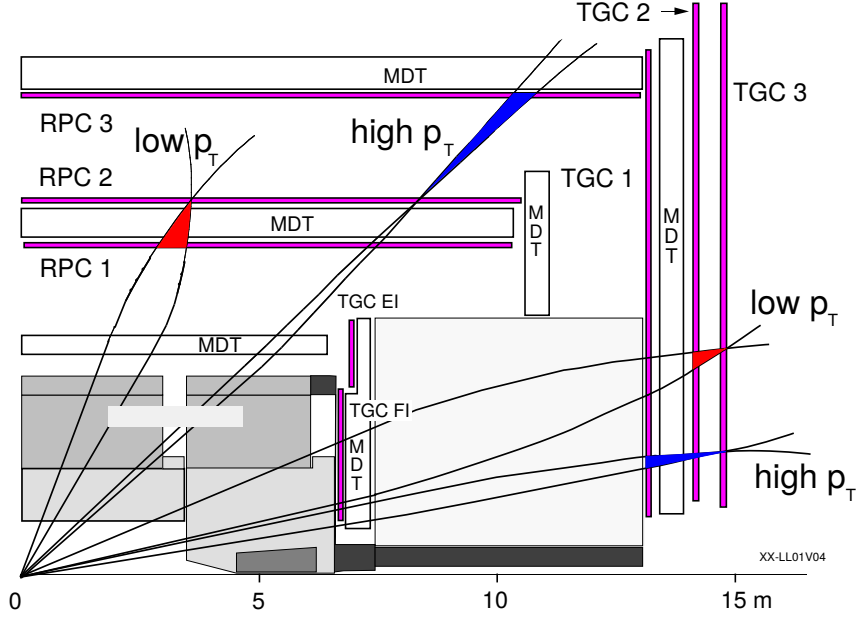


Figure 4.4: Quarter-section of the muon spectrometer subsystems in a plane containing the beam axis. CSC detectors are not shown, but they cover the η region beyond the MDT acceptance. [36]

The *muon-to-CTP Interface* (MUCTPI) receives these muon candidates and applies corrections to avoid double counting of muons coming from overlapping detectors. The total muon multiplicity for each momentum thresholds is then calculated, and together with position information sent to the topological and central trigger processors. Upon L1A this information is sent to be analysed in the HLT.

4.3.3 Level-1 central trigger

The *level-1 topological trigger* (L1Topo) [37], available since Run 2, is part of the L1 central trigger and uses information from the L1Calo and MUCTPI to perform trigger decisions based on the topology of the event, like angles or invariant masses of trigger objects.

The CTP combines input signals from the other subsystems using configurable rules to produce the level-1 trigger decision. It uses lookup tables and content addressable memory to decode the multiplicities of the trigger objects. Once the signals are decoded, they are combined with logical operations into 512 trigger items. The trigger items are put into coincidence with pre-defined patterns which can allow or disallow triggers, and a configurable prescale factor can be applied for every trigger to randomly select a fraction of events.

Trigger items can also be vetoed in case one of the detector readout is busy, i.e. over-occupied, to protect sub-detector front-ends from overflow or data

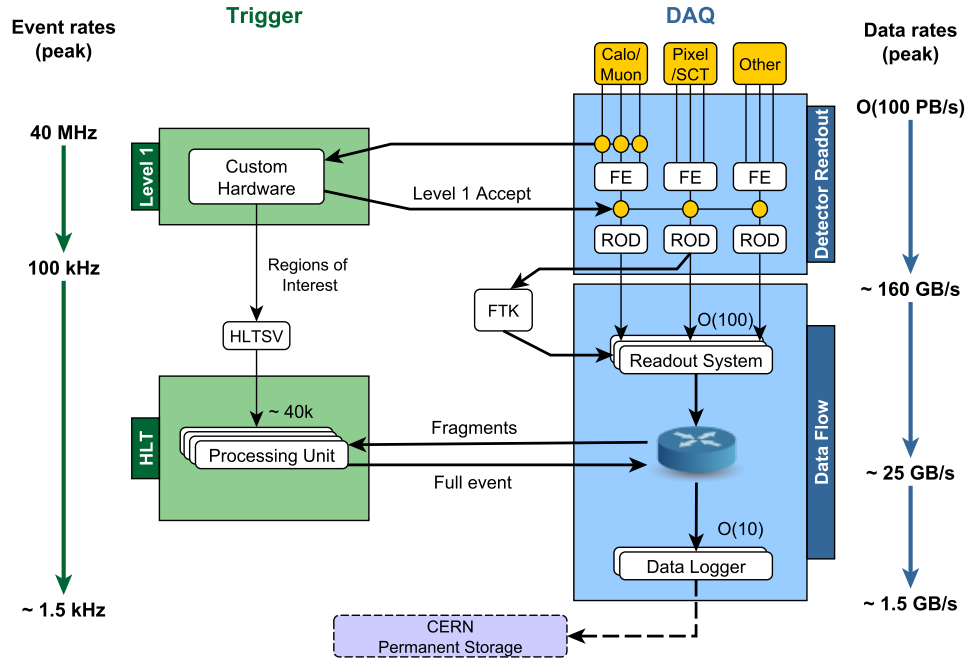


Figure 4.5: Outline of the DAQ system used for the second run of the LHC [38].

corruption. Veto can also be applied based on a configurable dead-time.

The configurable dead-time uses a *simple dead-time*, which consists of a fixed value applied after each trigger, and a *complex dead-time*, which consists of leaky bucket algorithms modelling a derandomiser with fixed size and readout rate.

Finally, if any of the 512 items was triggered and not vetoed, the L1A signal is forwarded to the sub-detectors to trigger the readout of the front-end electronics.

4.4 High level trigger

The *HLT data acquisition* (HLT/DAQ) system is responsible for getting the data selected by the L1 trigger from the detector readout system through the HLT and finally to storage (Fig. 4.5).

Tasks in the HLT/DAQ system are divided into three areas. Each software area has an independent core software and interfaces towards the other subsystems:

- the online infrastructure, responsible of configuring, controlling and monitoring the whole system, allows everything else to run;

- data-flow applications, in charge of handling I/O operations in the DAQ system, are responsible for securely transport data among the different parts of the system and finally save them to storage;
- trigger software, responsible for processing the data in order to take appropriate trigger decisions.

The ATLAS online infrastructure encompasses all software required to configure, monitor and control the data taking activities of the experiment.

There are in total about 30000 applications distributed on about 3000 hosts, all of which need to be configured, controlled and monitored. Given the rarity of the target phenomenology (Fig. 2.1), these three tasks cannot be overlooked as a systematic drop in efficiency would critically compromise the statistical significance of any possible discovery.

The *run control* (RC) is an application responsible of steering the data acquisition through well-defined states in a coherent way, guaranteeing synchronous execution of commands and smooth error recovery. The run control system relies on the *process manager* (PMG) to start and stop applications across the whole computing cluster.

Given the distributed nature of the TDAQ system, its size and complexity, failures and errors are inevitable and must be dealt with. For this reason, fault tolerance is one of the driving principle across the whole system. The system has to recover promptly and effectively, possibly without the need to stop data taking operations. For this reason, the RC is also assisted by the *central hints and information processor* (CHIP), an expert system which supervises data taking, automates operational procedures, handles abnormal conditions and performs advanced recoveries.

When an event is accepted by the L1, its data fragments are distributed to buffers in the *readout system* (ROS) via optical links. At the same time, a software component called *HLT supervisor* (HLTSV) assigns the RoI information to one of the thousands instances of *data collection managers* (DCMs) running on the computing farm.

Each worker nodes hosts one DCM, an application that handles all the I/O of the node *data-flow* (DF). Attached to each DCM there are as many *HLT processing units* (HLTPUs) as there are physical cores on the machine. The DCM starts by collecting the RoI data fragments for the assigned event and turns them to one of the available HLTPU of the node. HLTPU processes are forked from a single parent process to maximise memory sharing and run the HLT event selection software: a framework based on the ATLAS offline reconstruction and analysis environment ATHENA/GAUDI [39].

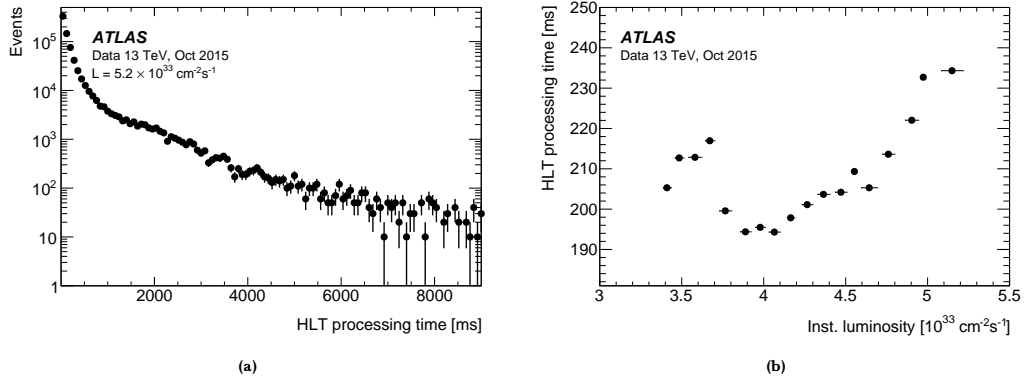


Figure 4.6: HLT Processing time for a L1 rate of 80 kHz and an average pile-up $\langle\mu\rangle = 15$. (a) Distribution showing long tails, but low average ~ 235 ms. (b) Average HLT processing time as a function of the instantaneous luminosity. [31].

The HLTPU starts by first analysing the RoI and proceeds with an incremental *event building* (EB) by requesting and processing more and more data fragments until the event is either rejected or fully accepted. In case of event rejection an instruction is sent to the ROSs to clear the corresponding fragments in order to free the buffers for new incoming data.

In case of acceptance the event is sent to the data loggers, called *sub-farm output* (SFO) for historical reasons, which are responsible for saving the event to disk and for sending the data to permanent storage. Once the SFO acknowledges delivery of an event, a clear instruction is sent to the ROSs.

4.4.1 HLT processing time

The ATLAS HLT computing cluster counts around 2000 nodes and 40000 CPU cores. The HLT processing time of a single event is mainly determined by the trigger menu and the number of pile-up interactions (Fig. 4.6). The increased processing time at low luminosities shown in Fig. 4.6 is due to additional triggers being enabled towards the end of the LHC fill to take advantage of the available CPU and bandwidth resources.

The HLT CPU utilisation depends on the L1 trigger rate and the average HLT processing time. About 40%, 35% and 15% of the processing time are spent on inner detector tracking, muon spectrometer reconstruction and calorimeter reconstruction, respectively [31]. The muon reconstruction time is dominated by the large rate of low- p_T B-physics triggers.

The hardware tracking for the trigger

In this chapter, the hardware tracking for the trigger system is described. The studies carried out as part of this thesis have produced two publications [2, 3]. The tests and estimates carried out have been taken into account by the ATLAS collaboration to drive the upgrade choices.

5.1 The high luminosity LHC

High luminosity LHC (HL-LHC) [41] is the name of a new configuration of the current LHC machine planned for the future, it relies on a number of key innovations to push the current accelerator technology beyond its present limits. The LHC and HL-LHC project schedule is shown in Fig. 5.1.

Phase-0 started with the consolidation of the machine elements during the *first long shutdown* (LS1). At the end of LS1, the LHC operated at a centre-of-mass energy of $\sqrt{s} = 13$ TeV during the *second run* (Run-2) and delivered in the second half of 2017 an instantaneous luminosity in excess of $L = 2.0 \times 10^{34} \text{ cm}^{-2}\text{s}^{-1}$, and an average pile-up of about 60 minimum bias collisions per bunch crossing. By the end of Run-2, the LHC delivered a total integrated luminosity of 156 fb^{-1} to each of the LHC experiments.

Phase-I started with the *second long shutdown* (LS2) in 2019. LS2 was scheduled to end in 2020, but given the impact of the COVID-19 pandemic its finish date has been rescheduled to 2021. During this time, the luminosity production of LHC is consolidated and the ATLAS experiment is being upgraded to record up to approximately 300 fb^{-1} during the *third run* (Run-3) (2022–2024).

At the end of this period, *phase-II* will start with the HL-LHC upgrades of

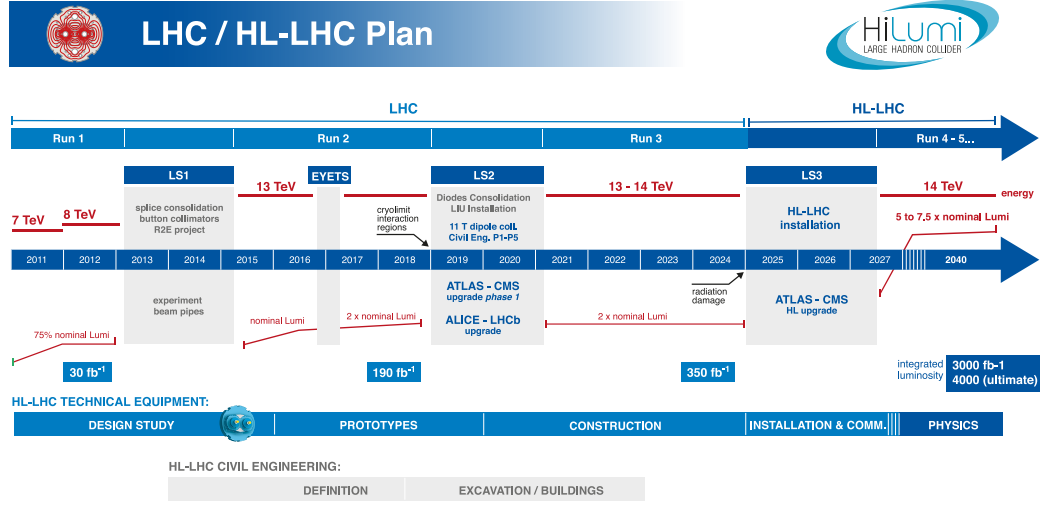


Figure 5.1: Timeline of the planned LHC and HL-LHC upgrade phases. [40]

the LHC machine and of the ATLAS detector that will occur during the *third long shutdown* (LS3) between 2025–2027, allowing full exploitation of the LHC physics programme.

The HL-LHC project is planned to begin collisions in the second half of 2027 and it will allow the ATLAS detector to collect an integrated luminosity of 3000 fb⁻¹ after ten years of operation.

5.2 ATLAS TDAQ for phase-II

The ATLAS TDAQ upgrade project for phase-II involves three systems: the level-0 trigger system, the data acquisition system, and the *event filter* (EF) system. A functional overview of the upgraded design is shown in Fig. 5.2.

The upgraded trigger system will utilise input data from the calorimeters, the muon system and the new *inner tracker* (ITk) [43, 44], which will replace the entire current ATLAS tracking system.

For the calorimeters, input information from both the LAr and Tile calorimeters will be utilised. The readout electronics of these two calorimeters will be upgraded to extend their radiation tolerance limits and to meet the new trigger rates and latencies requirements.

For the muon system, the trigger information will include MDT, RPC, and TGC alongside the newly installed *new small wheel* (NSW) [45]. The trigger electronics of the RPC and TGC will be upgraded, and new RPC detectors

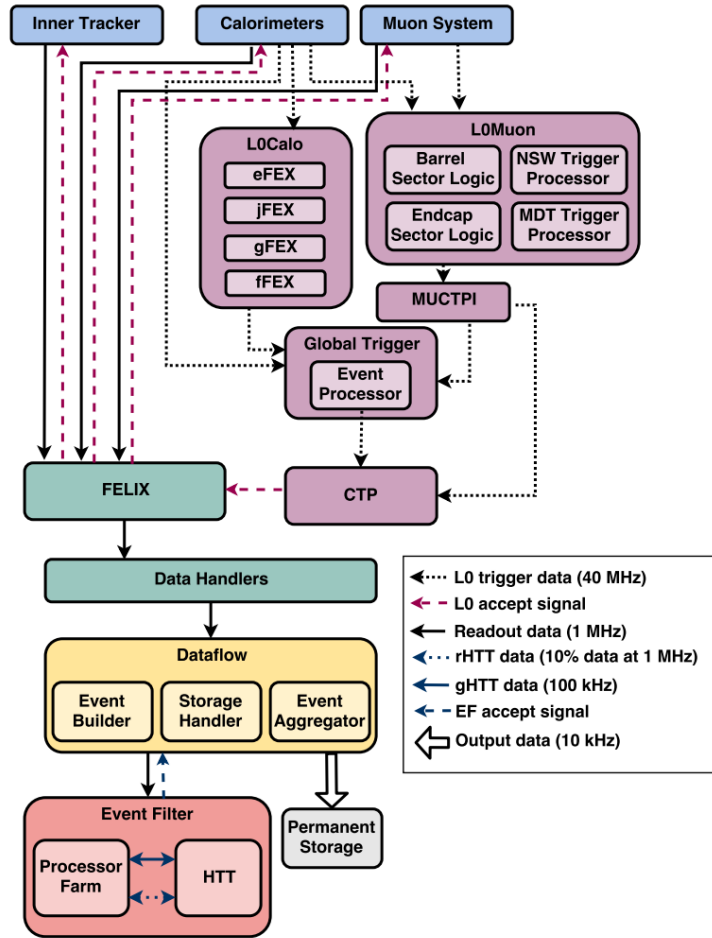


Figure 5.2: Functional overview of the ATLAS TDAQ upgrade design for phase-II. [42]

will be added in the barrel region, corresponding to $|\eta| < 1$, to achieve an increased coverage.

For the inner tracker, the new system will be formed by a combination of silicon strip and pixel detectors distributed in layers to achieve a total geometrical coverage for $|\eta| < 4$.

5.2.1 Level-0

The level-0 trigger system comprises the *L0Calo*, the *L0Muon*, the *global trigger*, and the *central trigger*.

L0Calo and L0Muon are similar in functionality to their predecessors used during phase-I: L1Calo and L1Muon (see Sec. 4.3). They operate at the full bunch crossing rate of 40 MHz to apply an initial event selection and to identify features that could be examined by the subsequent trigger levels.

The MUCTPI provides an interface between the barrel and endcap compon-

ents of the L0Muon system, the global trigger and *central trigger processor* (CTP). The MUCTPI also provides an *overlap removal* functionality by identifying muon candidates that have been counted twice in the L0Muon system by calculating multiplicities for various transverse-momentum thresholds.

The *global trigger* is a new subsystem which will perform offline-like algorithms on full-granularity calorimeter data. It will also identify topological signatures. Information regarding spatial locations, reconstructed energy/momentum values and discriminant variable, is sent by the L0Calo and L0Muon subsystems to the global trigger for processing to refine the electron, photon, tau, muon and jet selections.

Finally, the CTP forms the final level-0 decision by taking into account the trigger menu configuration, the pre-scale factors, and the dead-time requirements. This decision is transmitted as a *level-0 acceptance* (L0A) signal to the other detector systems.

5.2.2 Dataflow

Following the level-0 trigger decision, the detector data is sent through the *front-end link exchange* (FELIX) subsystem to the *data handlers*, where detector-specific processing, like data formatting and monitoring, can be implemented before buffering into the *dataflow* subsystem.

The dataflow subsystem buffers, transports, aggregates, and compresses event data for later utilisation in the EF System. The EF is also planned to be decoupled from the underlying distributed storage system. In this way, the data is buffered in the dataflow subsystem while waiting for the EF selection result.

The overall readout subsystem is designed to handle about 1 MHz of event rate, for a total bandwidth of 5.2 TB/s.

5.2.3 Event filter

A large CPU based computing farm is necessary to cope with the planned 1 MHz input rate. And to aid in this task, a new hardware-based subsystem for track reconstruction will be installed alongside the traditional CPU based computing farm: the *hardware tracking for the trigger* (HTT).

The introduction of the HTT system allows for a fast initial rejection in the EF for single high- p_T lepton and multi-object triggers coming from background processes. This will reduce the EF input rate to around 400 kHz. In the EF, a software-based reconstruction will then follow to achieve further rejection.

Events selected by the EF are transferred to the ATLAS permanent storage system. Since the raw output event size is expected to be of 6 MB and the

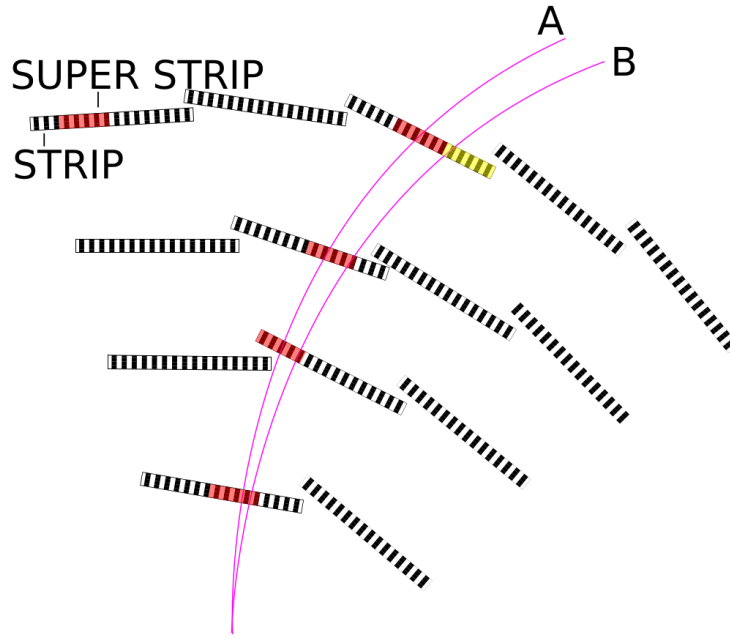


Figure 5.3: Illustration of tracks traversing layers divided into superstrips in a tracker. [42]

total trigger output is expected to be of 10 kHz, the total bandwidth out of the system is expected to amount about 60 GB/s. Which correspond to about 40 times more than the output bandwidth of the current system.

5.3 Hardware tracking for the trigger

The HTT will aid the ATLAS trigger system for the reconstruction of charged particles in the high pile-up conditions of the HL-LHC. It is based on custom-designed *associative memories* (AMs) *application-specific integrated circuits* (ASICs) for pattern recognition and *field programmable gate arrays* (FPGAs) for track reconstruction and fitting.

The HTT processes data registered by the ITk, containing information on the particles interaction points. The strip and pixel data is processed into clusters using clustering algorithms. The clusters are then converted to groups of consecutive silicon strip or pixel channels called *superstrips* (see Fig. 5.3). To each superstrip is assigned a unique *superstrip identifier* (SSID). The choice of superstrip dimensions is closely related to the choice of the number of layers used in the AM processing step.

5.3.1 Associative memory ASICs

The core component of the pattern recognition are the AM ASICs, massively parallel processors able to perform bit-wise comparison of incoming data against

pre-stored patterns.

A large number of single particle tracks in simulated training events is used to form template patterns from a number of layers of the ITk. A collection of these template patterns is called a *pattern bank*. These banks are then stored in AM ASICs.

5.3.2 Trigger processors

The *trigger processor* TP is an *Advanced Telecommunications Computing Architecture* (ATCA) board designed to host two double mezzanine cards. The function of the TP is to receive input data, perform clustering, share data with other TPs and send the particle cluster hits for processing to the mezzanine cards. Once tracks are received back from the mezzanines, duplicate track removal is performed on the TP and then tracks are returned to the EF.

Two different types of mezzanine cards can be mounted on the TP: the *pattern recognition mezzanine* and the *track fitting mezzanine* (TFM). In this way, the physical TP boards can be used to implement two distinct functions: the *associative memory tracking processor* (AMTP) which performs first-stage tracking, and the *second stage tracking processor* (SSTP) which performs the second-stage processing. The AMTP module is implemented housing two PRM on the TP board, while the SSTP module houses two TFM.

The computing power is carried out by the mezzanine cards plugged into the TP.

The PRM is designed to contain about 20 AM ASICs and a large FPGA. The role of the on-board FPGA is to control the mezzanine, prepares the input data to the AM ASICs, receive the matched roads out of the AM ASICs, and perform the first-stage track fitting.

The AM ASICs are distributed over four groups on the PRM. Each group can be controlled independently, receive different data, and process separate events.

The goal of the TFM is to find tracks corresponding to particle hits in all thirteen ITk detector layers.

HTT units

The size of the HTT system can be measured in terms of independent logical tracking units called *HTT units* (Fig. 5.4). Each unit comprises both AMTP and SSTP boards in a 6-to-1 ratio.

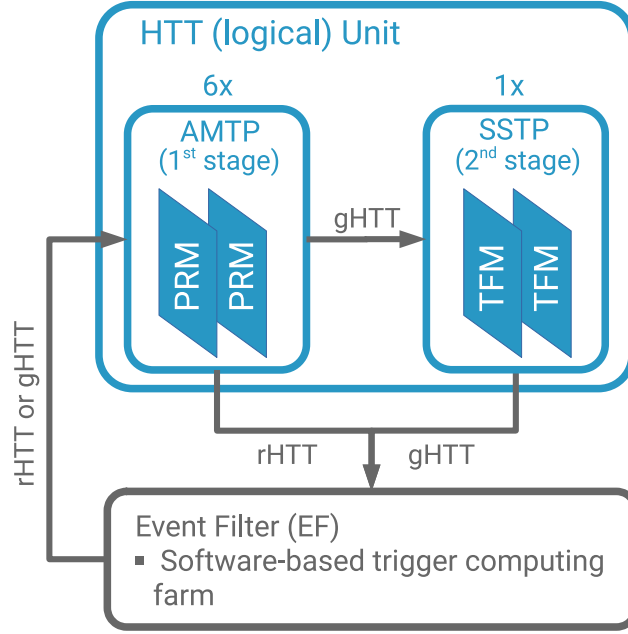


Figure 5.4: Schematic view of the HTT Unit. The AMTP processes ITk data and produces first-stage tracks, which is sent back to the EF in case of rHTT request or to the SSTP in case of gHTT request for further processing. The SSTP uses the AMTP output to process additional ITk data and returns second-stage tracks to the EF.

5.3.3 Regional and global tracking

Depending on the trigger signature two types of track reconstruction requests can be sent from the EF to the HTT system: *regional* (rHTT) or *global* (gHTT) tracking. The rHTT corresponds to carrying out only the first stage of processing, while the gHTT corresponds to both first and second stage of processing.

Regional tracking occurs at a rate of about 1 MHz and it uses up to 10% of the ITk data by selecting tracking modules in regions based on the results of the level-0 trigger system. The rHTT searches for all tracks with $p_T > 2 \text{ GeV}$ in limited $\eta \times \phi$ regions of interest defined by the previous level of trigger decision. It uses only eight ITk detector layers and it processes on average 10% of all ITk detector data in these events.

Global tracking instead reconstructs particle tracks at a rate of about 100 kHz. It produces tracks closer to offline quality, suitable for b -jet tagging, E_T^{miss} soft term calculation, soft jets and pile-up suppression. The gHTT searches for all tracks with $p_T > 1 \text{ GeV}$.

Both rHTT and gHTT cover the full ITk acceptance of $|\eta| < 4$.

5.3.4 Pattern matching layers

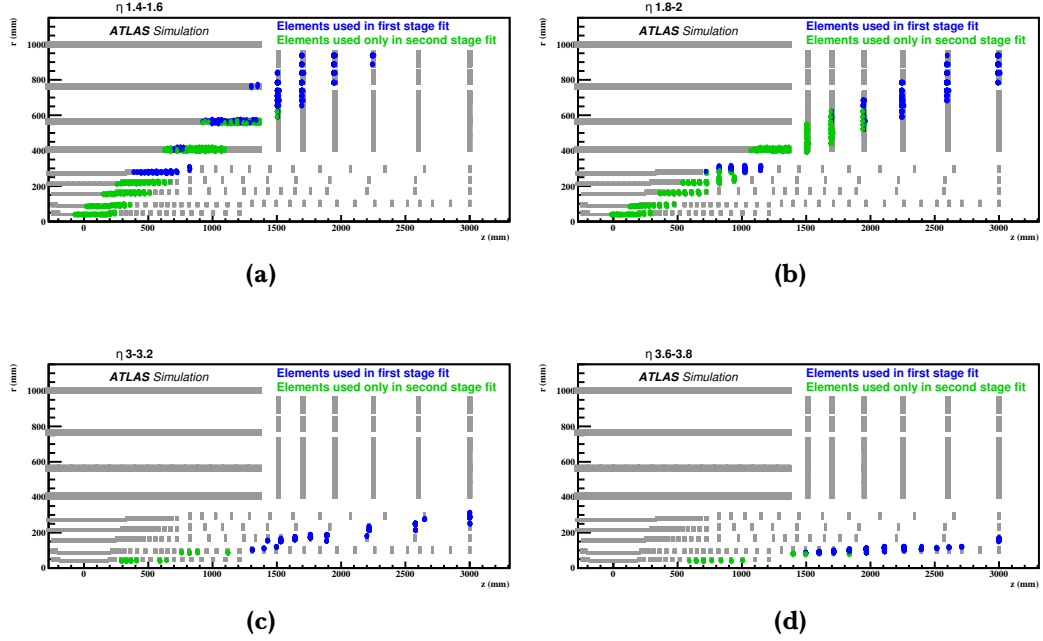


Figure 5.5: Layers used for the first- and second-stage of track fitting in four different η -regions. In blue, the hits from the eight layers used in the first-stage of processing. In green, the hits in layers used in the second stage of processing. [42]

The choice of which ITk layers to use affects the number of patterns required, the number of false matches and the resolution of the fitted track.

Which layers are used depends on the pseudorapidity η of the track. The two sides of the double-sided strip are treated as two separate layers while one physical pixel layer counts as one layer in the pattern bank. A fixed set of layers is used for the barrel region, while multiple sets of layers are defined for the transition and end-cap regions. These sets of layers are chosen depending on which layers are hit in the simulated training events.

Fig. 5.5 shows which ITk layers are used for the first- and second-stage of track fitting in four different η -regions. The first set of layers at low η are all barrel layers. While going to higher η values substitutes progressively more end-cap layers. At very high values of η , tracks do not leave any hit signal in the strip end-cap layers, therefore multiple pixel hits in the end-cap are used.

5.3.5 First processing stage

In the first processing stage of the HTT system, the particle hits from eight ITk layers are clustered into consecutive ITk strip or pixel channels by the FPGA mounted on the TP.

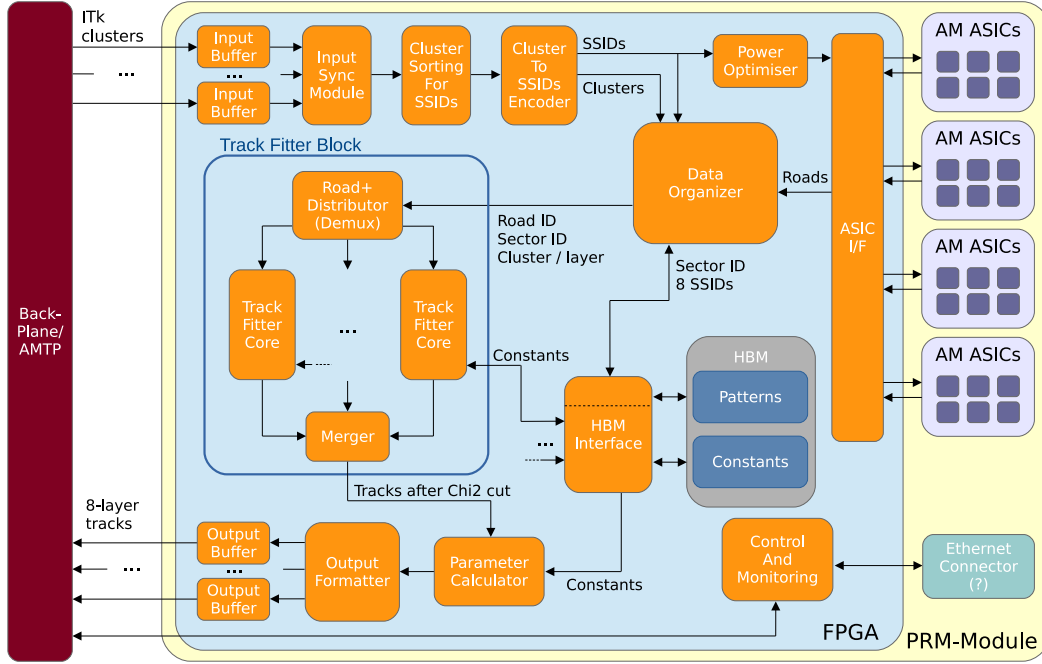


Figure 5.6: Data-flow diagram of the major modules of the PRM FPGA.

The cluster information is then prepared by the TP in the FPGA mounted onto the PRM. Here the data is further prepared and sent to the AMs, where it is compared against the pattern banks stored in them. At this point, the AMs output consisting of the track candidates corresponding to a positive match is sent back to the PRM's FPGA. The quality of the track candidates is assessed inside the PRM's FPGA with a χ^2 method that uses the full-resolution particle hits coordinates. Only the tracks with a corresponding χ^2 value below a certain required threshold are kept. To conclude the first stage of processing, the five track parameters ($d_0, z_0, \phi_0, q/p, \cot(\theta_0)$) are calculated for those tracks.

5.3.6 Second processing stage

The second processing stage carried out in the TFM and refines the first stage of track fitting. The results of the first stage computed by the PRM are sent to the TFM through the TPs. The TFM extrapolates each first-stage track to the other ITk layers and it associates any matching hit by computing a new χ^2 . In a similar way to the first processing stage, if a threshold is met, the track parameters are recomputed. The full-resolution coordinates of the particle hits from every ITk layer are used in order to achieve the best possible resolution.

5.4 Track fitting for the PRM

The first-stage of track fitting computation is carried out by dedicated firmware modules in the PRM's FPGA: the *track fitter block* (TFB) and the *parameter*

calculator (PC). Fig. 5.6 shows a full diagram of the major modules of the PRM firmware architecture design.

The two entities carry out mathematical operations at high rate. Therefore, to achieve the best possible performance, these two entities are developed to leverage the physical *digital signal processing* (DSP) blocks embedded in the FPGA's fabric.

5.4.1 Data-flow

Fig. 5.6 shows the PRM firmware block diagram. The PRM accepts clusters from ITk received from the AMTP. The data that arrives at the input of the PRM is synchronised by the *input sync module*. The clusters are sorted per SSID and per ITk layer by the *cluster sorting for SSID* module. The cluster information is encoded in the corresponding SSID by the *cluster to SSID encoder* module. The SSIDs are sent to the *data organiser* (DO) and to the AM ASICs through an interface module.

The DO stores the cluster information indexed by SSID for faster retrieval later based on which SSIDs have been selected by the AM.

The TFB handles the output of the DO and with a demultiplexer redistributes each input to five different *track fitter cores* (TFCs) which operate in parallel. The main function of each TFC is to perform a linear fit through the computation of a χ^2 .

After a χ^2 cut is applied the PC computes the five track helix parameters as a linear combination of the measured coordinates.

The various TFB and PC constants are fetched from the *high bandwidth memory* (HBM), which is present on certain FPGAs models.

5.4.2 Track fitter block

Inside the TFB, the linear fit is computed according to the following equation:

$$\chi^2 = \sum_{i=1}^{N_f} \left[\left(\sum_{j=1}^{N_{\text{coo}}} S_{ij} x_j \right) + h_i \right]^2, \quad (5.1)$$

where x_j are the full-resolution local coordinates of the cluster; S_{ij} and h_i are constant values computed by simulation; N_{coo} is the number of coordinates used for the fit, i.e. the size of the x_j vector; and N_f is the number of degrees of freedom of the χ^2 , corresponding to the difference between N_{coo} and the number of track parameters to be computed.

The value of the N_{coo} parameter depends on the specific multiplicity of pixel and strip layers used for this stage of processing. Each pixel layer corresponds to two coordinates, while each strip layer corresponds to one coordinate. Therefore, given the design constraint that of the eight ITk layers at least one pixel layer is always included (the outermost pixel layer) and at the most four pixel layers are included, N_{coo} can vary between 9 and 12.

Hit guessing

A requirement for the first-stage track fitting is to be resilient to the absence of cluster hit information from one or two of the eight layers. To be able to do so, the TFB implements the "guessing" of missing coordinates. In the absence of hit information from either one or two layers, the TFB interpolates the other hits to compute likely coordinates for the missing hits in their corresponding layers. This functionality translates to a set of additional operations to be performed before the χ^2 computation.

The missing components of the input coordinates vector x_j are found through the minimisation of the χ^2 presented in Eq. (5.1), which corresponds to solving the following equation:

$$\hat{x}_i = \sum_{j=1}^M C_{ij}^{-1} t_j \quad (5.2)$$

where \hat{x}_i is the vector of size M with the missing coordinates; while C_{ij} and t_j are given by

$$\begin{aligned} C_{jn} &= \sum_{i=1}^{N_f} S_{i\hat{k}_j} S_{i\hat{k}_n} \\ t_j &= - \sum_{i=1}^{N_f} S_{i\hat{k}_j} h_i - \sum_{i=1}^{N_f} S_{i\hat{k}_j} \sum_{\tilde{k}} S_{i\tilde{k}} x_{\tilde{k}}. \end{aligned} \quad (5.3)$$

Once \hat{x}_i is computed, its components can be inserted into the vector x_j in place of the missing coordinates.

5.4.3 Parameter calculator

The PC block follows the TFB in the data-flow (Fig. 5.6). The functional form of the equations that the PC carries out is very similar to the one performed by the TFB in Eq. (5.1). Specifically, it corresponds to

$$p_i = \sum_{j=1}^{N_{\text{coo}}} (B_{ij} x_j + q_i), \quad (5.4)$$

where x_j are the full-resolution cluster local coordinates, while B_{ij} and q_i are constant values unique to the specific sector the coordinates x_j belong to. As there are five track parameters, the index i runs from 1 to 5.

5.4.4 Operations breakdown

A breakdown on the type and number of mathematical operations corresponding to the computation carried out in the TFB is given in Tab. 5.1 and Tab. 5.1. The two tables correspond to the χ^2 computation and the hit guessing respectively.

The most computational intensive case scenario corresponds to $N_{\text{coo}} = 12$ in Eq. (5.1), with four pixels and four strips, and $M = 4$ in Eq. (5.2), with two missing hits in two pixel layers.

General case		$N_{\text{coo}} = 12, N_f = 7$
Nr. sums	$(N_{\text{coo}} + 1)N_f - 1$	90
Nr. mult	$(N_{\text{coo}} + 1)N_f$	91

Table 5.1: Breakdown of the mathematical operations corresponding to the computation of the TFB χ^2 presented in Eq. (5.1).

General case		$N_{\text{coo}} = 12, M = 4$
Nr. sums	$M(N_{\text{coo}} - M) + M(M - 1)$	44
Nr. mult	$M(N_{\text{coo}} - M) + M^2$	48

Table 5.2: Breakdown of the mathematical operations corresponding to the computation of \hat{x}_i presented in Eq. (5.2) and Eq. (5.3).

The breakdown on the type and number of mathematical operations corresponding to the computation carried out by the PC is given in Tab. 5.3.

5.5 Digital signal processing performance test

As part of this thesis, a preliminary test has been carried out to estimate the performance of the TFB and the PC.

Since at their core, the TFB and PC perform matrix multiplications, the test consists in simulating, for the targeted FPGA model, a series of multiply-accumulate iterations corresponding to the multiplication of one matrix row

General case		$N_{\text{coo}} = 12$
Nr. sums	$5N_{\text{coo}}$	60
Nr. mult	$5N_{\text{coo}}$	60

Table 5.3: Breakdown of the mathematical operations corresponding to the computation of the track parameters p_i from Eq. (5.4).

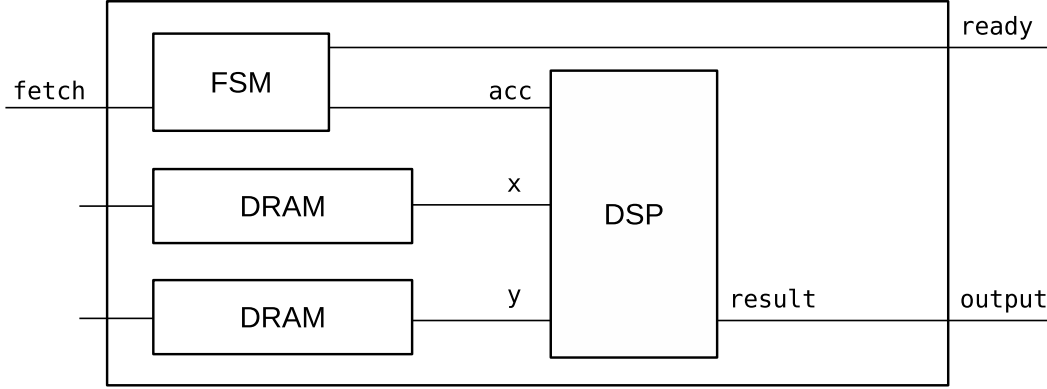


Figure 5.7: Schematic view of the firmware module employed for the DSP performance test. Only the important lines, referenced in Fig. 5.9, are drawn.

with a vector of size twelve. The performance metric in which we are interested is the number of multiply-accumulate operations that it is possible to carry out with one DSP in one second.

A sketch of the *hardware description language* (HDL) implementation used is shown in Fig. 5.7. The DSP block takes two input values, x and y , from two *dynamic random-access memories* (DRAMs) embedded in the FPGA. The DSP is operated in multiply-accumulate mode with all the pipeline register banks enabled (Fig. 5.8). The DSP *accumulate* signal is controlled by a *finite state machine* (FSM) block, which reacts to the *fetch* signal. The FSM also controls the *ready* signal for the output.

This test is coherent with the implementation plan of retrieving the constants from the HBM and keeping them buffered locally to be accessed by the TFB and PC.

The timing diagram shown in Fig. 5.9 reports the sequence of events of how the block is operated. The *fetch* signal initiates the retrieval of x and y from the local DRAMs with a latency of two clock cycles. The accumulate *acc* control signal of the DSP is set to “low” for the first input and then set to “high” for the following eleven. After the DSP internal latency of five clock cycles the *result* register starts holding the partial results: x_1y_1 , $x_1y_1 + x_2y_2$, etc. until at the

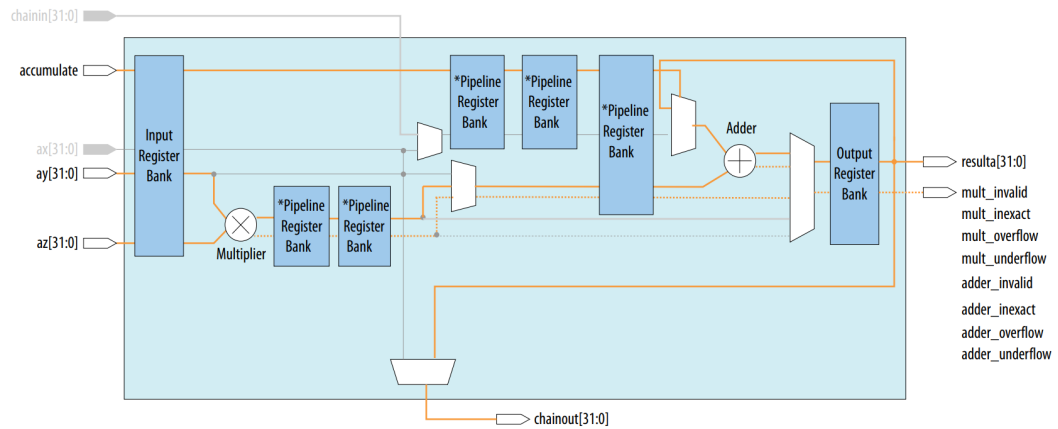


Figure 5.8: Diagram of the Intel Altera Stratix 10 DSP in multiply-accumulate mode. [46]

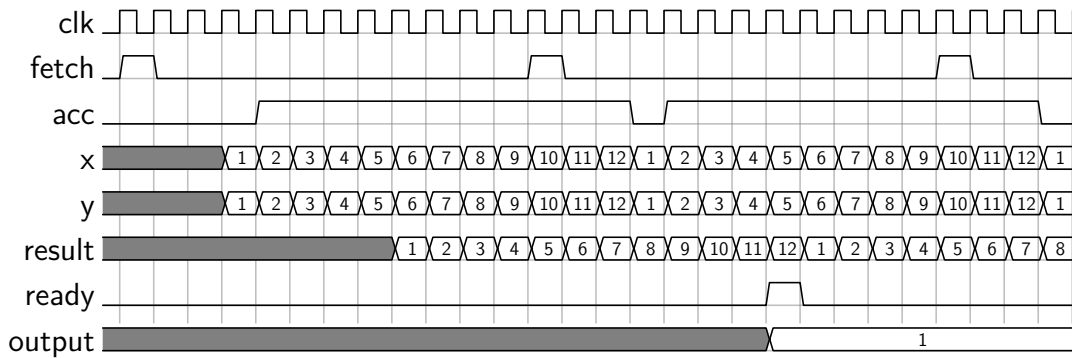


Figure 5.9: Timing diagram for the firmware block sketched in Fig. 5.7 with numeric indices representing the calculation steps.

twelfth iteration it equals $x_1y_1 + x_2y_2 + \dots + x_{12}y_{12}$. This last value is then also made available as *output*, while the second set of input already entered the DSP pipeline without any clock delay, synchronously with the *acc* control signal set to “low” to restart the accumulation.

The diagram shows a total initial latency of seven clock from the fetch signal to when the first partial result is made available in the result signal. Two clock cycles out of these seven are to read the values from the dual port memory, while five clock cycles can be considered due to the internal DSP latency. It is possible to count the DPS internal latency by counting the number of registers enabled in the schematic of Fig. 5.8.

If this initial start-up latency is negligible over the whole length of operation, it is instead important to notice that this design manages to achieve no dead-time between each set of operations. There is no gap in-between the different sets of inputs. As soon as the first twelve input values have been multiplied and summed, the next set can be pipelined into the DSP without any delay. In this way, the DSP is constantly operated, causing a maximum usage of this

resource.

With these settings the firmware simulation was able to run with a clock frequency of 500 MHz for a Stratix 10 FPGA device with -2 speed grade.

As result from this test, a conservative assumption for the performances of the final implementation is to consider the possibility of operating it at about 200 MHz, less than half of the test rate. This assumption translates to consider an overall performance of 200 M *multiply-accumulate* (macc) operations per second for one DSP, i.e. $200 \text{ M} \frac{\text{macc}}{\text{s DSP}}$.

5.6 Resource allocation estimate

The amount of resources available in an FPGA is limited. It is therefore important to assess, during the firmware design phase, that the proposed architecture does not exceeds the capacity of the targeted FPGA model. Specific focus is given to the number of DSPs and the HBM bandwidth.

Each PRM card is required to compute four billion χ^2 values per second inside their FPGA. Numerically, this translates to $4 \frac{\text{Gfit}}{\text{s}}$, where one fit corresponds to the computation of one χ^2 . The TFB is responsible of fulfilling this requirement.

About 20% of the tracks computed by the TFB are accepted to move to the next step, where their track parameters are computed by the PC. Therefore the PC is activated at about 20% the rate of activation of the TFB.

By counting how many mathematical operations are necessary to achieve this PRM requirement, it's possible to estimate how many resources have to be allocated. A breakdown of the mathematical operations has been presented in the previous sections and for ease of reference it is summarised in Tab. 5.4.

For the TFB there are about 140 macc operations that are necessary to compute the χ^2 value for one track candidate. About 90 are necessary to compute the χ^2 value itself of Eq. (5.1), as presented in Tab. 5.1, and about 50 are necessary to guess the missing hits of Eq. (5.2) and Eq. (5.3), as presented in Tab. 5.2. $N_{\text{coo}} = 12$ and $M = 4$ are assumed. The constants are S , h , Sh , S^2 and C^{-1} as defined in Eq. (5.1), Eq. (5.2) and Eq. (5.3). And finally, single-precision floating-point is assumed to compute the size.

For the PC there are about 60 macc operations necessary to compute the five track parameters p_i of Eq. (5.4), as presented in Tab. 5.3. The constants are B_{ij} , q_i as defined in Eq. (5.4).

		Number	Size
TFB	Macc operations per χ^2	140	
	Constants used per χ^2	140	4.5 kb
	Constants stored per χ^2	317	10.1 kb
	Total constants stored in HBM	10 M	320 Mb
PC	Macc operations per set of p_i	60	
	Constants used per set of p_i	60	1.9 kb
	Constants stored per set of p_i	60	1.9 kb
	Total constants stored in HBM	1.9 M	61 Mb

Table 5.4: TFB and PC operational summary.

5.6.1 DSP usage

The following formulas estimates how many DSPs would be necessary to instantiate for the TFB and the PC.

For the TFB, with 140 macc operations to be executed for each fit, in order to reach a target of $4 \frac{\text{Gfit}}{\text{s}}$ with an assumed performance of $200 \text{ M} \frac{\text{macc}}{\text{s DSP}}$, a total of 2800 DSPs would be necessary:

$$140 \frac{\text{macc}}{\text{fit}} \times \frac{4 \frac{\text{Gfit}}{\text{s}}}{200 \text{ M} \frac{\text{macc}}{\text{s DSP}}} = 2800 \text{ DSP}. \quad (5.5)$$

For the PC, with 60 macc operations to be executed for each fit, in order to reach 20% of $4 \frac{\text{Gfit}}{\text{s}}$ (which is the required target for the PC), with an assumed performance of $200 \text{ M} \frac{\text{macc}}{\text{s DSP}}$, a total of 240 DSPs would be necessary:

$$60 \frac{\text{macc}}{\text{fit}} \times \frac{(4 \times 0.2) \frac{\text{Gfit}}{\text{s}}}{200 \text{ M} \frac{\text{macc}}{\text{s DSP}}} = 240 \text{ DSP}. \quad (5.6)$$

5.6.2 High bandwidth memory

The HBM stores the various constants to compute the χ^2 , the possible missing coordinates and the track parameters. The subset of necessary values for each computation is retrieved from the HBM and kept locally in the FPGA, close to the computing core. These cached values are reused about ten times on

	DSPs		HBM usage		HBM BW	
TFB	2800	71%	40 MB	0.7%	224 GB/s	44%
PC	240	5%	7.6 MB	0.09%	192 GB/s	37%
Tot	3040	76%	48 MB	0.8%	416 GB/s	81%

Table 5.5: Resource usage summary. Percentages are expressed with respect to the nominal values for Intel Altera Stratix 10 MX 2100 [47].

average [42]. On average, ten consecutive fits are performed with the same set of retrieved constants, then a new set is requested to the HBM. Therefore, the rate of access of the HBM is about 10% the fit rate.

Therefore, the required HBM bandwidth is estimated by multiplying the access rate with the size of the requested payload.

For the TFB, with an access rate of 0.4 GHz and a payload of 560 B, the required bandwidth is of 224 GB/s.

Analogously, for the PC, with an access rate of 20% 0.4 GHz and a payload of 240 B, the required bandwidth is of 192 GB/s.

The resource estimates for the TFB and PC are reported in Tab. 5.5. The total DSP usage corresponds to about 76% of all DSPs available in the targeted FPGA model. The HBM memory allocation is negligible, while the bandwidth utilisation is at about 80% of the nominal value declared by the FPGA vendor.

Analysis motivation

In the following next nine chapters is presented the data analysis for which the work presented in this thesis has contributed. The analysis has also been published in [1] on behalf of the ATLAS collaboration.

The top quark plays a special role in the SM and in some BSM physics theories. Therefore, measurements of top quark provide an important test of the SM and any observed deviation from the SM predictions could indicate the presence of new physics.

The large top quark mass and the large $t\bar{t}$ pair production cross section in pp collisions make top quark production at the LHC a unique laboratory frame for studying the behaviour of QCD at newly accessible high energy scales.

Measurements of the top quark pair single- and double-differential cross sections as functions of different variables are the object of the analysis presented in this thesis. The measured distributions can be used to strengthen constraints on *parton distribution functions* (PDFs) and tuning of precision cross-section Monte Carlo computations.

The good momentum resolution for both top quarks enables characterisation of the kinematic properties of additional jet radiation accompanying the $t\bar{t}$ system in relation to the top-quark pair kinematics. Correlations between the $t\bar{t}$ system and associated jet production are also measured, and are compared with predictions of matrix element calculations.

The differential distributions are measured in data at both particle and parton level. The particle level covers a fiducial phase space, while the parton level covers the full phase space. Furthermore, the cross-section distributions are presented both absolute and normalised.

The channel considered in this analysis is the fully hadronic decay mode or

hadronic channel, characterised by both W bosons decaying hadronically. The final-state configuration at tree level therefore contains six jets, two of which originate from b -quarks. More jets may be produced by emission of initial- or final-state QCD radiation.

The use of the fully hadronic final state complements measurements in other top-quark decay channels.

Unlike the boosted topology, where one or both of the two top quarks are produced with high momentum resulting in a overlap between the jets, the all-hadronic channel focuses on events in which all decay jets from the top quarks are resolved as separate $R = 0.4$ jets. The all-hadronic jet topology permits probing of lower transverse momentum top quarks compared to those observed in the boosted jet topology, as well as jet radiation emitted nearly collinear to the top quark.

Unlike in the leptonic decay modes, the four-momenta of the top quarks can be determined directly from the quark decay products, as the kinematic ambiguities arising from the production of neutrinos are avoided. This allows to determine the top-quark pair kinematics and makes for a precise measurement of the kinematic correlations between the top quarks and any accompanying jet radiation.

6.1 Observables

This analysis measures the differential cross-sections for a variety of observables sensitive to the kinematics of top quark pair production and accompanying radiation. These variables rely on the reconstruction of the top system.

A series of jet-related observables are also defined to measure the top-quark pair accompanying radiation.

Since each of the decay products in the all-hadronic final state is directly measurable in the detector, this channel is especially suited to determining the kinematics of the individual top quarks and of the $t\bar{t}$ system.

6.1.1 Kinematic observables of the top quarks and $t\bar{t}$ system

Single-differential cross-sections are measured at both particle and parton levels for a series of kinematic observables of the top quarks and $t\bar{t}$ system. For the top quark kinematics, the transverse momentum of the leading and sub-leading top quarks ($p_T^{t,1}$ and $p_T^{t,2}$) and the absolute rapidity of the leading and sub-leading top quarks ($|y^{t,1}|$ and $|y^{t,2}|$) are measured. For the $t\bar{t}$ system, the transverse momentum $p_T^{t\bar{t}}$, the absolute value of the rapidity $|y^{t\bar{t}}|$ and the mass

$t\bar{t}$ are measured. These variables describe the characteristic features of the four-momenta of the individual top quarks and the $t\bar{t}$ system.

Additional differential cross-sections, sensitive to more than one aspect of $t\bar{t}$ production, are also measured to provide further information about the properties of the $t\bar{t}$ system.

$H_T^{t\bar{t}}$ is the scalar sum of the p_T of the two top quarks:

$$H_T^{t\bar{t}} = p_T^{t,1} + p_T^{t,2} \quad (6.1)$$

$|y_{\text{boost}}^{t\bar{t}}|$ is the absolute value of the average rapidity of the two top quarks:

$$|y_{\text{boost}}^{t\bar{t}}| = |y^{t,1} + y^{t,2}|/2 \quad (6.2)$$

$\chi^{t\bar{t}}$ is the exponential of the absolute value of the difference between the rapidity of the two top quarks

$$\chi^{t\bar{t}} = \exp(|y^{t,1} - y^{t,2}|) \quad (6.3)$$

$\Delta\phi^{t\bar{t}}$ is the angular distance in ϕ between top quarks

$$\Delta\phi^{t\bar{t}} = \phi^{t,1} - \phi^{t,2} \quad (6.4)$$

Differential cross-sections that comprise directional observables and transverse momentum ratios are measured at particle level such that they may be used to constrain the modelling of the top quarks and their decay products by various MC generators.

$|P_{\text{cross}}^{t\bar{t}}|$ is the cross products of the jet directions:

$$|P_{\text{cross}}^{t\bar{t}}| = \left| [\hat{b}_1 \times (\hat{j}_1 \times \hat{j}_2)] \times [\hat{b}_2 \times (\hat{j}_3 \times \hat{j}_4)] \right| \quad (6.5)$$

$|P_{\text{out}}^{t,1}|$ is the out-of-plane momentum defined as the projection of the top-quark three-momentum onto the direction perpendicular to the plane defined by the other top quark and the beam axis (\hat{z}) in the laboratory frame:

$$|P_{\text{out}}^{t,1}| = |\vec{p}^{t,1} \cdot (\vec{p}^{t,2} \times \hat{z}) / |\vec{p}^{t,2} \times \hat{z}|| \quad (6.6)$$

These variables are meant to probe possible directional combination effects of the top quarks and system decay jets.

$Z^{t\bar{t}}$ is the ratio of the p_T of the sub-leading top quark to the p_T of the leading

top quark:

$$Z^{t\bar{t}} = \frac{p_T^{t,2}}{p_T^{t,1}} \quad (6.7)$$

R_{Wt} is the ratio of the W -boson p_T to the associated top quark's p_T (leading or sub-leading), while R_{Wb} is the ratio of the W -boson p_T to the associated b -quark's p_T (leading or sub-leading).

6.1.2 Jet observables

A series of jet-related observables are defined and unfolded at the particle level in the fiducial phase space.

For nomenclature reference, jets that are not associated with either top quark by the reconstruction procedure are referred to as *additional jets*. While the *closest* top quark to a given jet refers to the top candidate with the smaller ΔR separation from the jet in question, where the ΔR separation is measured relative to the closest top quark.

The number of reconstructed jets (N_{jets}) is one of the jet-related observables.

The following observables are sensitive to the angular and energy correlations between the additional jets and the top quarks:

- $\Delta R_{t,\text{close}}^{\text{extra1}}$, $\Delta R_{t,\text{close}}^{\text{extra2}}$ and $\Delta R_{t,\text{close}}^{\text{extra3}}$ are ΔR between the leading, sub-leading, sub-subleading extra jet and the closest top quark;
- $R_{t,1}^{\text{extra1}}$, $R_{t,1}^{\text{extra2}}$ and $R_{t,1}^{\text{extra3}}$ are the ratio of the leading, sub-leading, sub-subleading extra jet's p_T to the leading top quark's p_T ;
- $R_{\text{jet1}}^{\text{extra1}}$, $R_{\text{jet1}}^{\text{extra2}}$ and $R_{\text{jet1}}^{\text{extra3}}$ are the ratio of the leading, sub-leading, sub-subleading extra jet's p_T to the leading jet's p_T ;
- $R_{\text{extra1}}^{t\bar{t}}$ is the ratio of $p_T^{t\bar{t}}$ to the p_T of the leading extra jet.

The following observables are defined to constraint correlations between the angles and between the transverse momenta of additional jets themselves, which are of particular interest for multi-leg matrix element calculations:

- $\Delta R_{\text{jet1}}^{\text{extra1}}$ is the ΔR between the leading extra jet and the leading jet;
- $\Delta R_{\text{extra1}}^{\text{extra2}}$ and $\Delta R_{\text{extra1}}^{\text{extra3}}$ are the ΔR between the sub-leading, sub-subleading extra jet and the leading extra jet;
- $R_{\text{extra1}}^{\text{extra2}}$ and $R_{\text{extra1}}^{\text{extra3}}$ are the ratio of the sub-leading, sub-subleading extra jet's p_T to the leading extra jet's p_T .

6.1.3 Double-differential measurements

To better understand the correlations between different aspects of the $t\bar{t}$ system kinematics various double-differential measurements are carried out at both the particle and parton levels.

The following combinations of observables are useful to extract information about PDFs and to measure the top-quark pole mass:

- $p_T^{t,1}, p_T^{t,2}, |y^{t,1}|, |y^{t,2}|, p_T^{t\bar{t}}$ and $|y^{t\bar{t}}|$ in bins of $m^{t\bar{t}}$;
- $p_T^{t,1}$ in bins of $p_T^{t,2}$;
- $|y^{t,1}|$ in bins of $|y^{t,2}|$.

Additional observables combined with the jet multiplicity are useful to tune and constrain the parameters of MC generators:

- $p_T^{t,1}, p_T^{t,2}, p_T^{t\bar{t}}, |P_{\text{out}}^{t,1}|, \Delta\phi^{t\bar{t}}$ and $|P_{\text{cross}}^{t\bar{t}}|$ in bins of N_{jets} .

These are measured at the particle level only.

Data and Monte Carlo samples

In this chapter are described the data and Monte Carlo samples used in the analysis.

7.1 Data samples

The data samples used for the analysis were recorded with the ATLAS detector at $\sqrt{s} = 13$ TeV in 2015 and 2016. They were collected during several data-taking periods characterised by different beam and detector conditions. Only data taken under stable beam conditions and while all sub-detectors were operational are considered. The total integrated luminosity versus time is shown in Fig. 7.1.

The decision to use 2015 and 2016 data only was mostly dictated by the change in available trigger, as from 2017 onward jet triggers applied more stringent requirements on the jet transverse momentum. It was therefore decided to study a broader phase space with lower trigger p_T thresholds on the jets (see Sec. 9.1.1).

The selected data samples correspond to an integrated luminosity of 36.1 fb^{-1} with an uncertainty of 2.1% [48].

The average number of pp interactions per bunch crossing $\langle\mu\rangle$ for this data set is about 23.

7.2 Monte Carlo samples

Three types of physics process have been simulated using various *Monte Carlo* (MC) generators:

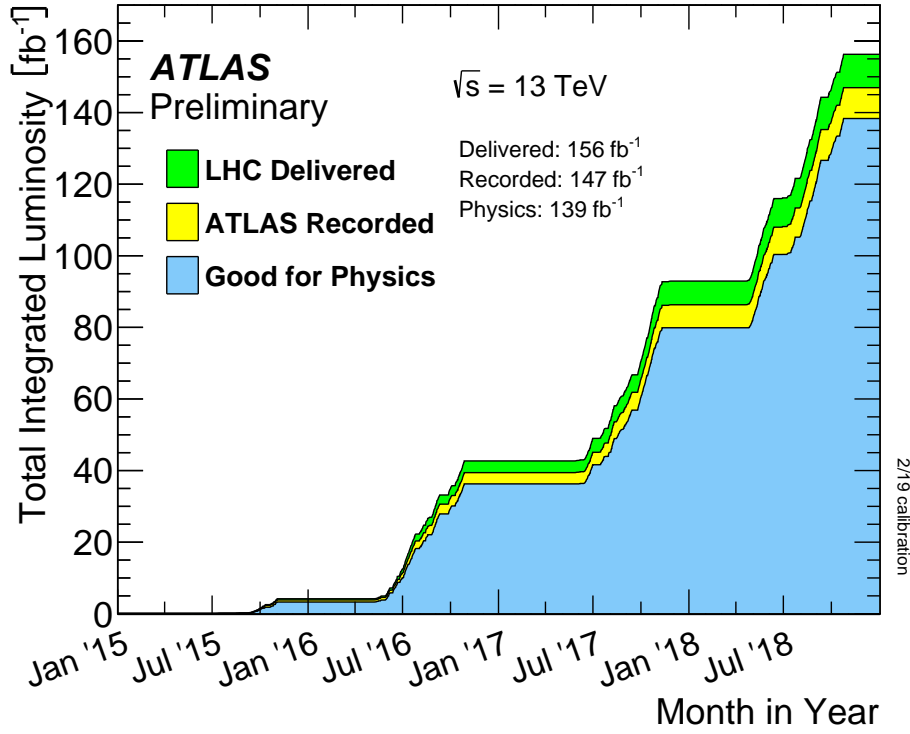


Figure 7.1: Cumulative luminosity versus time delivered to ATLAS (green), recorded by ATLAS (yellow), and certified to be good quality data (blue) during stable beams for pp collisions at 13 TeV centre-of-mass energy in 2015–2018.

- the *all-hadronic signal*: $t\bar{t}$ events where both W bosons decay hadronically;
- the *non-all-hadronic background*: $t\bar{t}$ events where at least one W boson decays leptonically.

The event simulation process comprises various steps.

The first step of the event generation is the *hard scattering* process. This step involves partons from each proton and uses fixed-order perturbative *matrix-element* (ME) scattering probability.

The second step is the *parton shower*. In this step, partons that participate in the hard process, like quarks and gluons, receive a high momentum transfer and radiate virtual gluons. These virtual gluons can in turn emit further gluons or produce quark-antiquark pairs.

Two states identified during these steps are the *initial-state radiation* (ISR) and the *final-state radiation* (FSR).

The ISR is a space-like process is developed on an incoming parton of the hard process when they emit radiation before the interaction with other particles. This state reduces the beam energy prior to the momentum transfer.

The FSR is a time-like process where particles keep losing energy until they split into primary particle and the descendent partons chain is terminated.

The final step of event simulation is the *hadronisation*, which is a non-perturbative generation of the observed final-state hadrons. Hadronisation is only described by phenomenological models.

The different steps of the simulation process are carried out by different software applications. The event generation is performed using either POWHEG [49] or aMC@NLO [50]. The parton shower is performed by using either PYTHIA8 [51] or HERWIG7 [52]. SHERPA [53] is an all encompassing generator that contains a matrix-element for the calculation of hard scattering processes, a parton-shower model and an hadronisation model. Specifically for hadronisation, PYTHIA8 is based on the *Lund string model* [54], while SHERPA and HERWIG7 are based on the *cluster model* [55]. The detector simulation is carried out by either GEANT [56] or ATLASTII [57].

7.2.1 Top-quark pair Monte Carlo samples

Various MC generators have been used to simulate $t\bar{t}$ events and they are listed in Tab. 7.1.

POWHEG+PYTHIA8 is the combination of generators used to produce the nominal sample, which is used for reference. This sample is generated at NLO using the POWHEG-BOX 2 event generator with the NNPDF3.0NLO PDF set [58]. The resummation damping factor h_{damp} , that controls the ME and PS matching and regulates the high- p_T radiations, is set to $1.5m_t$. The main effect of this parameter is to regulate the high- p_T emission against which the $t\bar{t}$ system recoils. Two other parameters, the hadronisation and factorisation scales, μ_R and μ_F respectively, are set to their default dynamic value of $\sqrt{m_t^2 + p_{T,t}^2}$.

PYTHIA8 (version 8.210) is configured to use the NNPDF2.3LO [59] PDF set and the A14 [60] tune set to simulate the parton shower, fragmentation and underlying event.

Two additional samples are used to study the effects of different levels of initial-state radiation. Up and down variation samples are created by applying different settings to POWHEG+PYTHIA8 by tuning the hadronisation and factorisation scales, $\mu_{R,F}$, and the h_{damp} parameter [61].

On the PWG+PY8 Up variation, the factorisation and hadronisation scales are varied by a factor of 0.5, while h_{damp} is increased to three times the mass of the top quark, and the Var3cUp A14 tune variation is used.

On the PWG+PY8 Down variation, the factorisation and hadronisation scales are varied by a factor of 2.0, while h_{damp} is kept at 1.5 times the mass of the

Application	$t\bar{t}$ signal	$t\bar{t}$ radiation syst.	$t\bar{t}$ PS syst.	$t\bar{t}$ ME syst.	$t\bar{t}$ comparison
Generator	POWHEG-BOX v2			MADGRAPH5 / aMC@NLO 2.6.0	SHERPA 2.2.1
σ precision	NNLO + NNLL				
PDF for ME	NNPDF3.0NLO				
Parton shower	PYTHIA8		HERWIG7	PYTHIA8	ME+PS@NLO
PDF for PS	NNPDF2.3LO		MMHT2014	NNPDF2.3LO	
Tune set	A14	Var3cUp	Var3cDown	H7UEMMHT	–
Scales	$h_{\text{damp}} = 1.5m_t$	$h_{\text{damp}} = 3m_t$ $\mu_{\text{R,F}} = 0.5$	$h_{\text{damp}} = 1.5m_t$ $\mu_{\text{R,F}} = 2.0$	$h_{\text{damp}} = 1.5m_t$	$\mu_q = H_T/2$ –

Table 7.1: Summary of $t\bar{t}$ MC samples used in the analysis, showing the generator for the hard-scattering process, cross-section σ normalisation precision, *parton distribution function* (PDF) choices for the hard-process matrix element (ME) and parton shower (PS), as well as the parton shower and hadronisation generator and the corresponding tune sets and scales.

top quark, and the Var3cDown A14 tune variation is used.

POWHEG+HERWIG7 is used to produce an alternative sample to estimate the effects of using different parton shower and hadronisation algorithms. POWHEG is configured identically to the setup used to generate nominal sample. While, differently from the nominal sample, PS, hadronisation and underlying events are simulated using HERWIG7 (version 7.0.4) configured with the MMHT2014lo68cl PDF set and H7-UE-MMHT tune set [62].

MADGRAPH5_aMC@NLO+PYTHIA8 is used to produce an alternative sample to evaluate the impact of the matrix element generator choice. The events are generated with version MADGRAPH5_aMC@NLO (version 2.6.0) and $\mu_q = H_T/2$ for the shower starting-scale functional [63]. As in the nominal samples, the NNPDF3.0NLO PDF set is used for the matrix element and the NNPDF2.3LO set is used for the parton shower.

SHERPA 2.2.1 is used to produce an alternative sample of $t\bar{t}$ events to provide an extra point of comparison. This sample was produced at NLO in QCD for up to one additional parton emission and at LO for up to four additional partons using the MEPSNLO merging scheme [64] with the CKKW merging scale fixed at 30 GeV [63]. Loop integrals were calculated with OpenLoops [65]. The shower, factorisation and renormalisation scales are set to $\mu_{F,R} = \sqrt{m_t^2 + 0.5(p_{T,t}^2 + p_{T,\bar{t}}^2)}$, and the NNPDF2.3LO PDF set is used.

All the samples described are normalised to the cross-section

$$\sigma_{t\bar{t}} = 832_{-29}^{+20}(\text{scale}) \pm 35(\text{PDF}, \alpha_S)\text{pb} \quad (7.1)$$

as calculated with the TOP++2.0 program at *next-to-next-to-leading order* (NNLO) in perturbative QCD including soft-gluon resummation to *next-to-next-to-leading-log order* (NNLL), and assuming $m_t = 172.5$ GeV.

The uncertainties on the cross section of Eq. (7.1) are due to variation of the scale terms $\mu_{F,R}$, PDF and α_S .

7.2.2 Background Monte Carlo sample

The non-all-hadronic background of $t\bar{t}$ events in which at least one W boson decays into a lepton and a neutrino are simulated with $t\bar{t}$ events where one or two leptonic decays were produced with the same settings are used for the nominal signal sample.

Object reconstruction

In this chapter, the reconstruction of physics objects collected by the ATLAS detector is described.

Detector-, particle- and parton-level objects are used to characterise the final-state event topology and to define the fiducial and full phase-space regions of the analysis.

The final state of interest in this measurement includes jets, some of which b -tagged, and it vetoes the presence of any isolated electron-, muon- or τ -leptons.

8.1 Electrons

To reconstruct and identify electrons over the full acceptance of the ATLAS detector, the electron candidates are reconstructed from combining the information regarding clusters of energy deposits in the calorimeter with the track information coming from the inner detector.

8.1.1 Electron reconstruction

The standard electron reconstruction procedure in the central region of the ATLAS detector, corresponding to $|\eta| < 2.47$, is based on three steps. The first step consists in the identification of the energy deposit in the EM calorimeter, the second step consists in the association of the ID tracks with the clusters of energy generated in the EM calorimeter. The last step consists in the reconstruction of the electron candidate.

The EM clusters are seeded from energy deposits with a total transverse energy above 2.5 GeV and are generated using a sliding-window algorithm [66]. The

window size for this algorithm is 3×5 in η and ϕ , and moves by units of 0.025×0.025 .

In the region of the ATLAS tracker detectors, corresponding to $|\eta| < 2.5$, an electron is defined by the existence of one or more reconstructed tracks matched to a cluster. These tracks are extrapolated from their last measured point of interaction to the second layer of the EM calorimeter. The extrapolated η and ϕ coordinates of this hit point are compared to the coordinates of the cluster in the layer, and the track and the cluster are considered matched if the distance between the hit point and the cluster barycentre correspond to $|\eta| < 0.05$.

An electron candidate is reconstructed when at least one track is matched with a cluster. In case two tracks have the same number of hits, the one that better matches the cluster is chosen. In case of absence of matching between the cluster and tracks, the candidate is identified as an absence of a matched photon candidate.

Electrons are distinguished from converted photons by the presence of two close tracks originating from a vertex displaced from the interaction point and by verifying the location of the first hit along the path of the single track.

After successfully matching a track and a cluster, the cluster sizes are optimised to take into account the overall energy distribution in the different regions of the EM calorimeter. In the EM barrel region the window size of the cluster is set to 3×7 in η and ϕ and moves in units of 0.025×0.025 . In the EM endcap regions the size is instead increased to 5×5 .

The total reconstructed electron candidate energy is determined from the sum of various contributions.

8.1.2 Electron identification

An algorithm for electron identification is applied to determine whether the reconstructed electron candidates are effectively electrons. The baseline ID algorithm is a likelihood based method. This method corresponds to a multivariate analysis technique that simultaneously evaluates several properties of the electron candidates while making a selection decision as described in [67].

This method provides a good separation between electrons and jets. The re-optimised ID algorithm for Run-2 is based on MC simulation samples. The identification criteria for electron candidates is based on sequential cuts on calorimeter, tracking and other variables which directly combine the track and cluster information.

Three sets of cuts, *loose*, *medium* and *tight* have been designed to provide an

increasing background-rejection power while decreasing at the same time the identification efficiency.

The loose selection uses shower-shape variables in both the first and the second layers of the EM calorimeter. Additional requirements on the electron track and track-cluster matching improve the rejection of the hadronic background of about a factor 5 in the E_T^{miss} range between 30 and 40 GeV, while maintaining a high identification efficiency.

The medium selection adds discriminating variables to the loose selection. It requires the presence of a hit in the innermost layer of the pixel detector and it applies a loose selection requirement on the transverse impact parameter $|d_0|$.

The tight selection achieves a rejection power a factor of two higher with respect to the medium selection. In addition to the requirements of the medium selection, stricter requirements are applied on track quality when a track extension is present in the TRT detector.

Electrons must satisfy $p_T > 15 \text{ GeV}$ and $|\eta| < 1.37$ or $1.52 < |\eta| < 2.47$ and satisfy the tight likelihood-based identification criteria based on shower shapes in the EM calorimeter.

8.1.3 Electron isolation

In addition to the identification criteria, electrons are required to be isolated to further discriminate between signal and background, where a calorimeter isolation discriminator is used by computing the sum of the transverse energies of topological clusters, excluding the energy of the candidate electron itself, within a cone of $R = 0.2$ around the cluster of the candidate electron.

A tracking based discriminator is used by computing the sum of the p_T of tracks, excluding the associated track of the candidate electron, within a cone of $R = 0.2$ around the track of the candidate electron and originating from the reconstructed primary vertex of hard collisions.

The considered tracks are required to have $p_T > 1 \text{ GeV}$, one hit in the innermost pixel detector layer, at least seven hits in the silicon detectors, and transverse (d_0) and longitudinal (z_0) impact parameters of less than 1 mm.

The isolation criteria ensure efficiencies of 90% for electrons with $p_T > 25 \text{ GeV}$ and 99% $p_T > 60 \text{ GeV}$.

8.2 Muons

The first step of reconstruction for muons is performed independently in the ID and MS subdetectors.

8.2.1 Muon reconstruction

In the ID, muons are reconstructed like any other charged particles, following the same steps of the electron reconstruction.

In the MS the reconstruction starts by identifying hit patterns that form segments inside each muon chamber. The MDT chambers identifies hits which are aligned on a trajectory in the bending plane of the detectors applying a Hough transform [68] algorithm. The RPC and TGC provide measurement of the hit coordinates orthogonal to the bending plane, while in the CSC chambers, segments are build in the η and ϕ planes.

The hit segments coming from all the different MS subdetectors are then fit together to build a track candidates. At least two matching segments are required to build a track candidate. In the barrel-endcap transition region only a single high-quality segment with η and ϕ information is required for the building of the muon track candidate.

Various algorithms can be used to combine the ID and MS muon reconstruction information several algorithms are used, depending on which MS subdetector is used in the reconstruction.

Combined (CB) muons are reconstructed with a global fit that uses the hits from both the ID and MS subdetectors.

Segment-tagged (ST) muons are reconstructed extrapolating the ID track to the MS with at least one track segment in the MDT or CSC chambers.

Calorimeter-tagged (CT) muons are reconstructed with a track in the ID is matched to an energy deposit in calorimeters.

Extrapolated (ME) muons are reconstructed based only on the MS track and a loose requirement on compatibility with originating from the ID. In general, the muon is required to traverse at least two layers of MS chambers to provide a track measurement, but three layers are required in the forward region.

8.2.2 Muon identification

Muon identification is performed by applying requirements that suppress background while selecting prompt muons with high efficiency.

Four muon identification selections, *medium*, *loose*, *tight* and *high- p_T* are defined. In the loose selection, all muon types are used to maximise the reconstruction efficiency. In the medium selection, only CB and ME tracks are used. At least three hits in at least two MDT layers are required, except in the $|\eta| < 0.1$ region where track with at least one MDT layer and no more than one MDT hole layer, are allowed. In the tight selection, only CB muons with hits in at

least two stations of the MS are considered and these also have to satisfy the medium selection criteria.

In the high- p_T selection, for tracks with transverse momentum greater than 100 GeV, only CB muons that have at least three hits in three MS stations and that pass the medium criteria selection are selected.

Muons must satisfy $p_T > 15$ GeV and $|\eta| < 2.5$, as well as the medium identification selection. Isolation criteria, similar to those applied to electrons, are also applied to muons to reduce the background from muons originating from heavy-flavour decays inside jets.

8.3 Jets

Hadronic particles deposit energy in the hadronic calorimeter system are grouped into objects called jets.

The basic structures of the jet reconstruction process in ATLAS are the *topological clusters* (topo-clusters), built from calorimeter's cells. Jets are reconstructed with anti- k_t algorithm [69] with $R = 0.4$.

To reduce the number of jets originating from pile-up, an additional selection criterion based on the *jet-vertex tagging* (JVT) technique [70] is applied. The JVT is a likelihood discriminant that combines information from several track-based variables and this criterion is only applied to jets with $p_T < 60$ GeV and $|\eta| < 2.4$.

8.3.1 Jet energy calibration

The ATLAS hadronic calorimeters are non-compensating and therefore the energy of the hadronic particles is underestimated. In order to correctly reconstruct the energy of the jets, a calibration procedure is carried out [71].

First a jet is corrected to point back to the reconstructed primary vertex. This procedure results in a significant improvement in the η resolution of the jets.

The following step consists of a pile-up correction. The number of additional particles that contaminate the jets due to pile-up effects are proportional to the area of the jet, which acts as a measure of the predisposition of the jet to pile-up. An area based subtraction method is therefore applied by computing an additive correction on the p_T of the jets as

$$p_T^{corr} = p_T^{jet} - \phi A^{jet}, \quad (8.1)$$

where ϕ is an estimate of the the global pile-up activity in each event and A is the area of the jet in the $\eta \times \phi$ plane.

The pile-up energy density of each event is calculated using jets reconstructed in the central ($|\eta| < 2.0$) region. A residual small pile-up dependence on the jet energy remains after the area based correction, and residual correction is further applied.

The following step focuses on the *jet energy scale* (JES) calibration, a correction that relates the reconstructed jet energy to the jet true energy. JES factors are derived from isolated jets using an inclusive jet Monte Carlo sample where the previous corrections have been applied. JES factors have a strong η dependence.

The measurement of the *jet energy resolution* (JER) in data is a multi-step process. To measure the jet energy resolution, for the majority of the jet p_T spectrum, the width of the distributions of the balance between jets and well measured photons or reconstructed Z bosons is used. In addition, the balance between di-jet events can be used to extend these measurements to higher $|\eta|$ and p_T spectrum.

8.3.2 *b*-tagging

The aim of *b*-tagging is the identification of jets originating from the hadronisation of *b*-quarks. This is achieved by using algorithms that exploit the distinctive properties of *b*-quarks. Most noticeably, due to their large lifetime, *b*-quarks travel a measurable distance from the primary interaction point before decaying, producing secondary vertices. Furthermore, their high mass makes for decay products with a larger transverse momentum relative to the jet axis with respect to those found in jets originated by lighter partons.

The MV2c10 [72] is a multivariate *b*-tagging algorithm developed for Run 2. It utilises a multivariate algorithm based on a *boosted decision tree* (BDT).

Three basic *b*-tagging algorithms, which all exploit the relatively long *b*-quark lifetime, are combined into this multivariate discriminant. Additionally, also the jet p_T and jet η are included as BDT training variables to take advantage of the correlations with other variables.

The first *b*-tagging algorithm is a likelihood-based combination of the transverse and longitudinal impact parameters, d_0 and $z_0 \sin \theta$ respectively. These parameters tend to be larger than usual due to the typical *b*-quark topology, characterised by at least one vertex displaced from the point of primary interaction.

The second *b*-tagging algorithm is a second vertex finder, which reconstructs an inclusive displaced secondary vertex within the jet. It tests all track pairs within a jet for a two-track vertex hypothesis.

The third b -tagging algorithm reconstructs of the b -quark multi-vertex decay chain using a Kalman filter. It searches for a common line, connecting the primary vertex to the secondary and tertiary decay vertices.

The jets are considered b -tagged if the value of the discriminant is larger than a threshold applied to the discriminant output value, chosen to provide a specific b -jet tagging efficiency in an inclusive $t\bar{t}$ sample. In this analysis, a threshold corresponding to 70% b -jet tagging efficiency is chosen. The corresponding rejection factors for jets initiated by charm quarks or lighter quark flavours are approximately 12 and 380, respectively [73].

8.4 Hadronic taus

Hadronically decaying τ -lepton (τ_{had}) candidates are reconstructed from hadronic jets associated with either one or three ID tracks with a total charge of ± 1 .

Taus must satisfy $p_T > 25 \text{ GeV}$ and $|\eta| < 2.5$. A BDT with a medium working point is used to discriminate τ_{had} candidates from jets initiated by quarks or gluons. A second BDT with a loose working point is used to eliminate electrons misidentified as τ -leptons.

8.5 Overlap removal

A procedure called *overlap removal* is applied to prevent double counting of reconstructed objects satisfying both the jet and lepton selection criteria. Overlap removal assigns objects a unique particle hypothesis, favouring well-identified and isolated particles.

If a selected electron shares a track with a selected muon, the electron is removed as it is likely to result from FSR.

If a jet and an electron are within $\Delta R < 0.2$ the jet is discarded.

If the distance between a surviving jet and an electron is $\Delta R < 0.4$, then the electron is discarded.

If a muon track is matched to a jet by a procedure called ghost association [69] or if a jet and a muon are within $\Delta R < 0.2$, then the jet is removed if its p_T , total track p_T and number of tracks are consistent with muon FSR or energy loss.

Ghost association consists in using particle tracks scaled to their four-momentum so that they have no effect on the jet clustering result while still being clustered into the jet they most naturally belong to, depending on the jet algorithm.

If the distance in ΔR between a jet and a muon candidate is $\Delta R < 0.4$, the muon is discarded.

If the distance between a jet and a τ_{had} -originated jet is $\Delta R < 0.2$, then the jet is discarded.

8.6 Particle-level objects definitions

Particle-level objects in simulated events are defined to closely match the reconstructed objects at the detector level. Only stable particles, particles with a mean lifetime $\tau > 30$ ps, are used.

In the MC generator event record, electrons and muons are required not to come from a hadron, either directly or through a τ -lepton decay. This ensures that the lepton comes from the decay of a real W -boson, without requiring a direct W -boson match. To take into account final-state photon radiation, the four-momenta of bare leptons are *dressed* to take into account final-state photon radiation by adding the four-momenta of all photons within a cone of size $\Delta R = 0.1$, and not originating from hadron decays.

Dressed electrons are required to have $p_T > 15$ GeV and $|\eta| < 1.37$ or $1.52 < |\eta| < 2.47$.

Dressed muons are required to have $p_T > 15$ GeV and $|\eta| < 2.5$.

Particle-level jets are reconstructed using the same anti- k_t algorithm used at detector level. The procedure takes as input stable particles inside a radius $R = 0.4$. Particle-level jets are required to have $p_T > 25$ GeV and $|\eta| < 2.5$. A jet is identified as a b -jet if a hadron containing a b -quark is matched to the jet using the ghost-association procedure where the hadron must have $p_T > 5$ GeV.

At particle level, no overlap removal is applied between the different objects.

8.7 Parton-level objects definitions

The simulated top-quark four-momenta are recorded after parton showering, but before decays are simulated, and correspond to the parton-level description of the event.

The full phase space is defined by the set of $t\bar{t}$ pairs in which both top quarks decay hadronically.

Event selection

In this chapter, the event selection of the $t\bar{t}$ events is described. Active contributions as part of the work presented in this thesis encompass the production of the latest version of the trigger efficiency curves with the final data and MC samples adopted, based on work already previously done, and the study for a kinematic likelihood fit for system reconstruction, as a possible alternative to the chi-square method.

9.1 Event selection

At particle level a fiducial phase-space is defined applying a series of cuts to particle level objects, analogous to those applied for the reconstructed objects.

9.1.1 Trigger

Data used in the measurements described in this thesis were collected using a multi-jet trigger. This specific trigger, HLT_6j45_0eta240, requires six jets with a p_T of 45 GeV in the central region of the detector. The η acceptance of the six jets changed from $|\eta| < 3.2$ in 2015 to $|\eta| < 2.4$ in 2016 (this change was introduced to reduce the trigger event rates). In the HLT, jets are reconstructed using the anti- k_t jet algorithm [69] using a radius $R = 0.4$.

The HLT_6j45_0eta240 trigger was chosen because it provides a high efficiency for signal events and does not pose any requirement on b -tagged jets, which is crucial for the evaluation of the background contribution in data carried out in this analysis.

Different turn-on curves were produced to estimate if any bias is introduced by using this trigger in the signal and control regions. The following selection was used for both data and Monte Carlo:

- pass the prescaled HLT_5j45 trigger,
- pass the HLT_6j45_0eta240 trigger,
- 5 jets with a p_T of at least 55 GeV to assure that we are on the plateau for the prescaled trigger
- the sixth jet having at least 40 GeV
- exactly 2 b -tagged jet are required
- all jets have the same η requirement that is varied from 2.0 to 2.4.

The first test was performed changing the η requirement of the jets to monitor any dependence on this parameter as the trigger threshold was close to the offline object selection.

Fig. 9.1 shows the trigger efficiency curves as for events containing a six jets with $p_T > 55$ GeV. The trigger is found to be highly efficient, with an efficiency of 96% measured in data. The MC efficiency is found to be higher in all bins, differing by 4% at 55 GeV.

The difference between the efficiency curves for different $|\eta|$ selections is negligible so using a selection of 2.4 is a safe option.

Similar turn-on curves with a requirement of 0 instead of 2 b -tagged jets are shown in Fig. 9.2. The difference is very small and therefore using the nominal trigger in the control region does not impact the background estimation.

9.1.2 Selection criteria

A series of selection criteria are applied to define a *signal region* (SR) containing a pure sample of resolved all-hadronic top-quark pair events.

Events are removed if detector defects or data corruption are identified or if the events do not contain a primary vertex with at least two associated tracks.

Events must contain at least six jets with $p_T > 55$ GeV and $|\eta| < 2.4$ to be in a regime where the trigger is highly efficient.

Exactly two b -tagged jets must be found.

A veto is applied to events containing at least one electron or muon with $p_T > 15$ GeV or a τ -lepton with $p_T > 25$ GeV.

Subsequently, a $t\bar{t}$ reconstruction procedure is implemented to suppress backgrounds from multi-jet production and to calculate the observable to be measured.

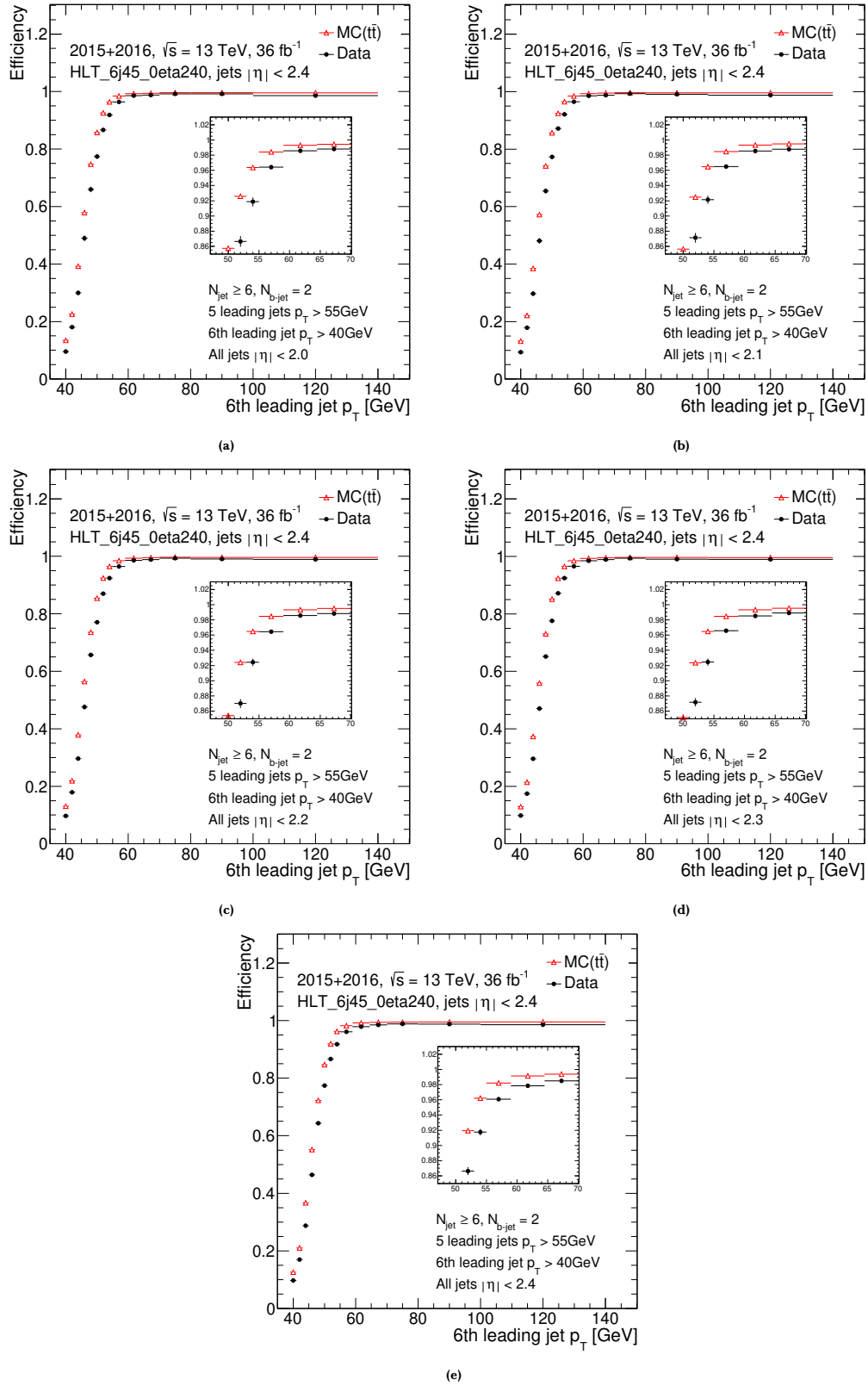


Figure 9.1: Trigger efficiency curves as a function of the 6th jet transverse momentum, for different values of the maximum allowed eta of the jets. These are computed in data and for a $t\bar{t}$ MC sample, selecting events with two b -tagged jets.

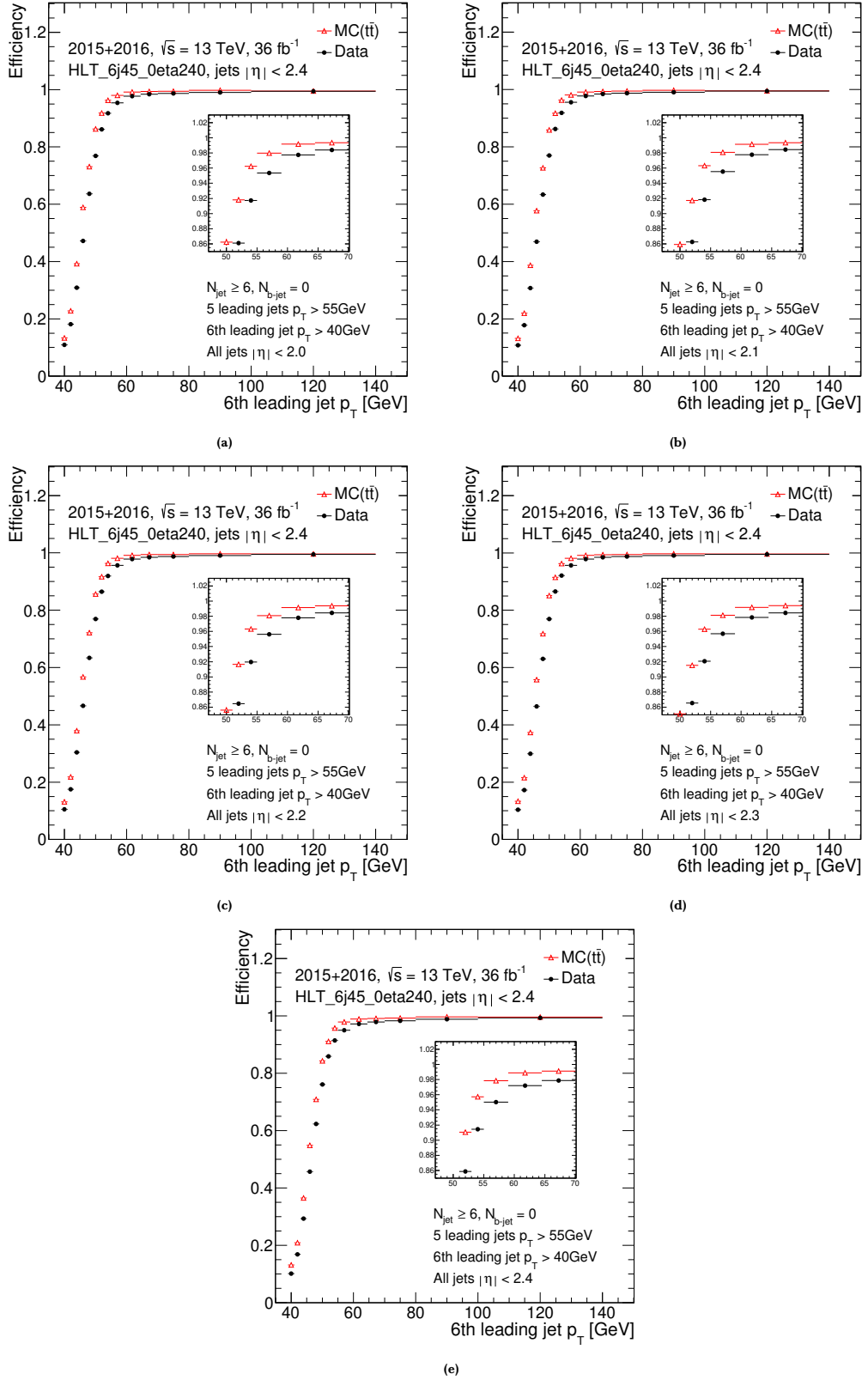


Figure 9.2: Trigger efficiency curves as a function of the 6th jet transverse momentum, for different values of the maximum allowed eta of the jets. These are computed in data and for a $t\bar{t}$ MC sample, selecting events with 0 b -tagged jets.

Requirement	Event selection
Multi-jet trigger	6 jets, $p_T > 45$ GeV
Exactly 0 vertex-matched isolated leptons	μ : $p_T > 15$ GeV, $ \eta < 2.5$ e : $p_T > 15$ GeV, $ \eta < 2.47$, excluding $1.37 < \eta < 1.52$ τ : $p_T > 25$ GeV, $ \eta < 2.5$
At least 6 jets	6 leading jets: $p_T > 55$ GeV Sub-leading jets: $p_T > 25$ GeV
Exactly 2 b -jets	b -tagging at 70% efficiency
Top mass	$130 \text{ GeV} < (m_{t,1}, m_{t,2}) < 200 \text{ GeV}$
Reconstructed χ^2_{\min}	$\chi^2_{\min} < 10.0$
ΔR between b -jets	$\Delta R_{bb} > 2.0$
Maximum ΔR between b -jet and W	$\Delta R_{bW}^{\max} < 2.2$

Table 9.1: Summary of selection requirements.

The events selection at both the detector level and particle level, are reported on Tab. 9.1 for all the objects defined.

In data, 44 621 events pass the full event selection while the signal purity is predicted to be 68% for the nominal all-hadronic $t\bar{t}$ sample.

The fiducial phase space used for unfolding to particle level is basically the same selections to the SR region at reconstruction level. The only two differences are that no trigger selection need be applied at particle level, as the six-jet selection ensures full efficiency. Additionally, in place of the b -tagging requirement, the MC b -hadron label is used.

9.2 Kinematic reconstruction of the $t\bar{t}$ system

A χ^2 method is used to identify which jets in the event correspond to the two top-quark candidates.

The χ^2 discriminant is evaluated for all possible permutation of six jets in the event to judge whether the considered permutation is compatible with the hypothesis of a top-quark pair, using the invariant masses of the W -boson dijet and the top-quark three-jet systems.

The χ^2 is defined as

$$\chi^2 = \frac{(m_{b_1j_1j_2} - m_{b_2j_3j_4})^2}{2\sigma_t^2} + \frac{(m_{j_1j_2} - m_W)^2}{\sigma_W^2} + \frac{(m_{j_3j_4} - m_W)^2}{\sigma_W^2}, \quad (9.1)$$

where $m_{b_1j_1j_2}$ and $m_{b_2j_3j_4}$ are the invariant masses of the jets associated with the decay products of the top quarks; $m_{j_1j_2}$ and $m_{j_3j_4}$ are the invariant masses of the jets associated with the decay products of the W bosons from the top quarks; the mass of the W boson, $m_W = 80.385$, is taken from the PDG [74], while the top mass does not appear explicitly to avoid sculpting the background to resemble the signal; and finally, σ_t and σ_W respectively represent the detector resolutions for the top-quark and W -boson masses.

The resolutions σ_t and σ_W have been determined from simulated $t\bar{t}$ events, where each of the parton-level decay products from the top-quark pair is matched to a reconstructed jet, imposing a $\Delta R < 0.3$ requirement. The mass distribution of the three-jet or dijet systems corresponding to each top quark or W boson are then fitted to a gaussian distribution, whose width is taken to be σ_t or σ_W respectively. For comparison, the same procedure is repeated for jets formed from stable particles, however only the detector-level resolutions are used in the analysis. These values are fixed to $\sigma_t = 17.6$ GeV and $\sigma_W = 9.3$ GeV for reconstruction for reconstruction of detector-level events, and $\sigma_t = 10.7$ GeV and $\sigma_W = 5.9$ GeV for particle-level reconstruction.

As a constraint, the two b -jets in the event cannot be associated to the same top-quark three-jet system and cannot be associated to a W -bosons dijet systems. Therefore, in each permutation, each b -jet is assigned to one top-quark candidate, and permutations are formed for each set of four jets selected from the remaining jets in the event. These four *light* jets are paired to form W -boson candidates, and each W -boson candidate is, in turn, matched with one of the b -jets to form a top-quark candidate.

For the W -boson pairings and b - W pairings, all unique permutations are considered.

The permutation with the smallest chi-square value, χ_{\min}^2 , is chosen as the one best describing the product of a top-quark pair decay in the event.

The χ^2 minimisation successfully matches all jets to top decay partons in approximately 75% of $t\bar{t}$ events with exactly six jets. In events with up to three additional jets, the matching can degrade by 10–30% due to the higher com-

binatorics involved. At particle level, the accuracy is higher at 85% in events with exactly six jets, and 60–70% in events with up to three additional jets.

9.3 Multi-jet background rejection

Various discriminants are used to reject background events.

Since multi-jet background events produce large χ^2 , events with $\chi_{\min}^2 > 10$ are rejected .

The masses of the leading and sub-leading reconstructed top quarks, in p_T ordering, are required to both be in the range between 130 GeV to 200 GeV.

The dominant mechanism for b -jets production in background multi-jet events is $g \rightarrow b\bar{b}$, which typically results in nearly collinear b -jets. However, in signal, the two b -jets are produced at large angles between each other, because the $t\bar{t}$ pair is normally produced back-to-back in the transverse plane. Therefore, the ΔR distance between the two b -jets (ΔR_{bb}) has good discriminant power and is required to be $\Delta R_{bb} > 2$.

Analogously, due to the tendency of the top-quark decay products to be collimated, the angle between a b -jet and its associated W boson is also a good discriminant from background. Since there are exactly two b -jets in the event, there are two of these angles, and the greater of them (ΔR_{bW}^{\max}) is required to be less than 2.2.

9.4 Kinematic Likelihood alternative study

In order to test the performance of an alternative reconstruction method to the χ^2 fit, the observables for the parton-level analysis were reconstructed using a *Kinematic Likelihood* (KL) fit [75] instead of the χ^2 method described in Sec. 9.2. This fit takes into account the decay kinematics of the top and anti-top quarks as well as accounting for mismeasurement of each decay jet, whereas the χ^2 allows only for overall resolution effects on the masses of the W and top quark. Thus, the fit provides a more accurate matching of the reconstructed jets to top decay products, resulting in more diagonal unfolding matrices.

Specifically, the likelihood is written as

$$\mathcal{L} = \mathcal{B}(m_{q1q2q3}|m_t, \gamma_t) \cdot \mathcal{B}(m_{q1q2}|m_W, \gamma_W) \cdot \mathcal{B}(m_{q4q5q6}|m_t, \gamma_t) \cdot \mathcal{B}(m_{q4q5}|m_W, \gamma_W) \cdot \prod_{i=1}^6 W_{\text{jet}}(E_{\text{jet},i}^{\text{reco}} | E_{\text{jet},i}), \quad (9.2)$$

where \mathcal{B} indicates a Breit-Wigner function, while the W_{jet} transfer functions are double-gaussian constraints describing the jet resolutions determined from Monte Carlo with respect to the parton four-momenta.

The reconstructed jets are each identified with a parton (q_n) by minimising \mathcal{L} over different permutations of the jet-to-parton associations. While the fit returns an estimate of each parton four-momentum, only the permutations returned by the fit are used, while the measured energies of the reconstructed jets are used to compute the observables to be unfolded.

Due to the computational cost of evaluating the likelihood, it is necessary to limit the number of permutations considered in the case of events with a large jet multiplicity.

Thus, the KL fit is allowed to use at most 7 jets in each event, allowing for the possibility that one jet originates from additional radiation.

The KL Fitter reconstruction package features several configuration options to define in which way the permutations are built. For clarity, the definitions of relevant KL Fitter configuration options are reported below.

For clarity, the definitions of relevant KL Fitter configuration options are reported below.

- `kNoTag` corresponds to the baseline likelihood fit, using only kinematics and disregarding b -tag information in the evaluation of the likelihood value for each permutation.
- `kWorkingPoint` augments the calculation of the event probability from KL Fitter by incorporating the b -tag efficiency and mistag rate for each of the jets, based on what parton identity KL Fitter has assigned and the b -tag discriminant.
- `kVeto` rejects permutations in which a b -jet is placed in the position of a W boson decay product.
- `kVetoLight` rejects permutations in which a light jet is placed in the position of a b -quark from the top decay.
- `kVetoBoth` rejects permutations that fail the criteria of both `kVeto` and `kVetoLight`.
- `kLeadingSeven` uses the seven leading jets in p_T to generate permutations (in which six jets are assigned to top decay products).
- `kBtagPrioritySevenJets` selects seven jets to generate permutations, adding first b -jets and then non- b -tagged jets.

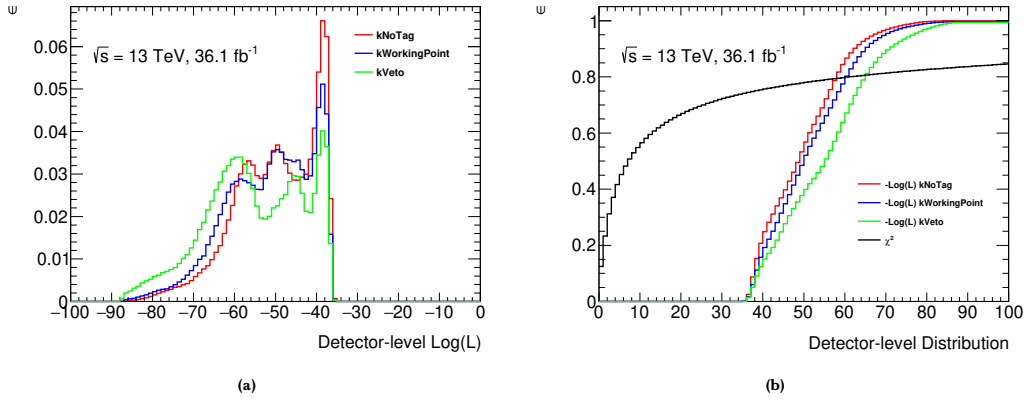


Figure 9.3: (a) Log likelihood distribution for different KLFitter b -tagging options. (b) Cumulative comparison between KLFitter and χ^2 selections, where the x -axis shows the χ^2 value or the negative log likelihood, curves normalised to the KLFitter option NoTag.

Of these options, it has been found that the KLFitter reconstruction incorporating b -tagging information performs better than if the b -tagging information is neglected. Furthermore, the best mean and resolution are extracted in the case of using the kVetoLight and kVetoBoth options, but these are found to be incompatible with the background estimation strategy due to rejecting all events with fewer than two b -jets. The kWorkingPoint option is found to be the best performing of the other options.

Fig. 9.3 shows the distribution and cumulative distribution of the KL fit likelihood for the best permutation. A cut is placed on the log likelihood at -41 , which ensures that only well reconstructed top events are retained. This was found to substantially improve the agreement between the reconstructed and parton level observables, compared to looser selections, relative to a cut at -54 . The KLFitter event probability is required to be greater than zero, which merely ensures that a valid permutation could be found.

The figures of merit used to compare the χ^2 and KLFitter reconstruction methods performance are the mean and RMS of the difference between the reconstructed and parton-level quantities. The results are presented in Fig. 9.4, showing better performance in the case of KLFitter.

After the event selection, the multi-jet background was estimated through the very same data-driven method described in Sec. 10.1.

It may be noticed, however, that in general the KLFitter reconstruction leads to larger detector-systematic uncertainties. An especially large uncertainty arises from the statistics available for the multi-jet background estimation being drastically diminished.

An older version of the analysis software has been used for the results presented

in this Sec. 9.4. This does not affect the validity of the conclusion.

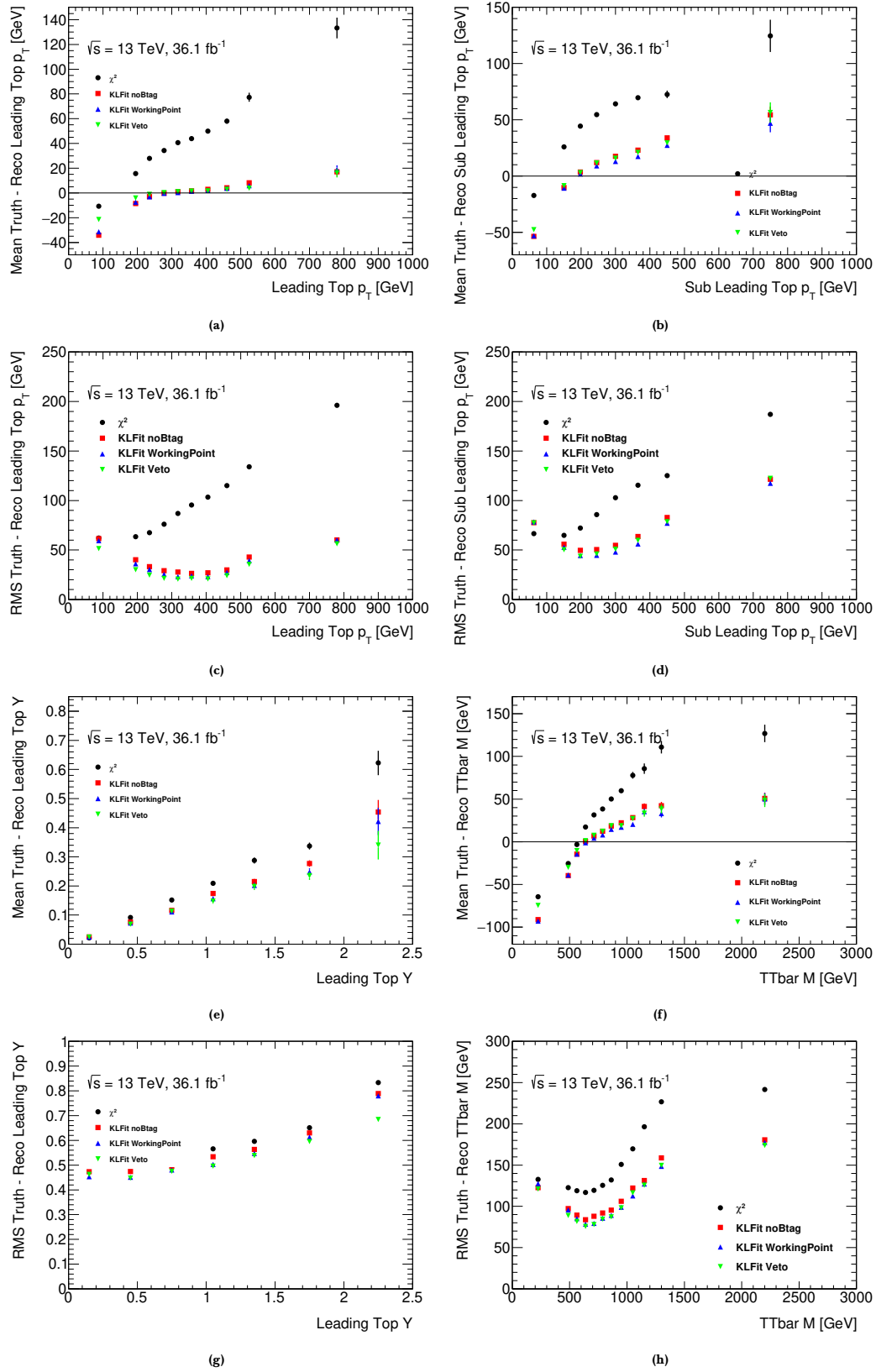


Figure 9.4: Bias and resolution comparison between KLfitter and χ^2 reconstruction for several observables: $p_T^{t,1}$, $p_T^{t,2}$, $y^{t,1}$ and $m^{t\bar{t}}$.

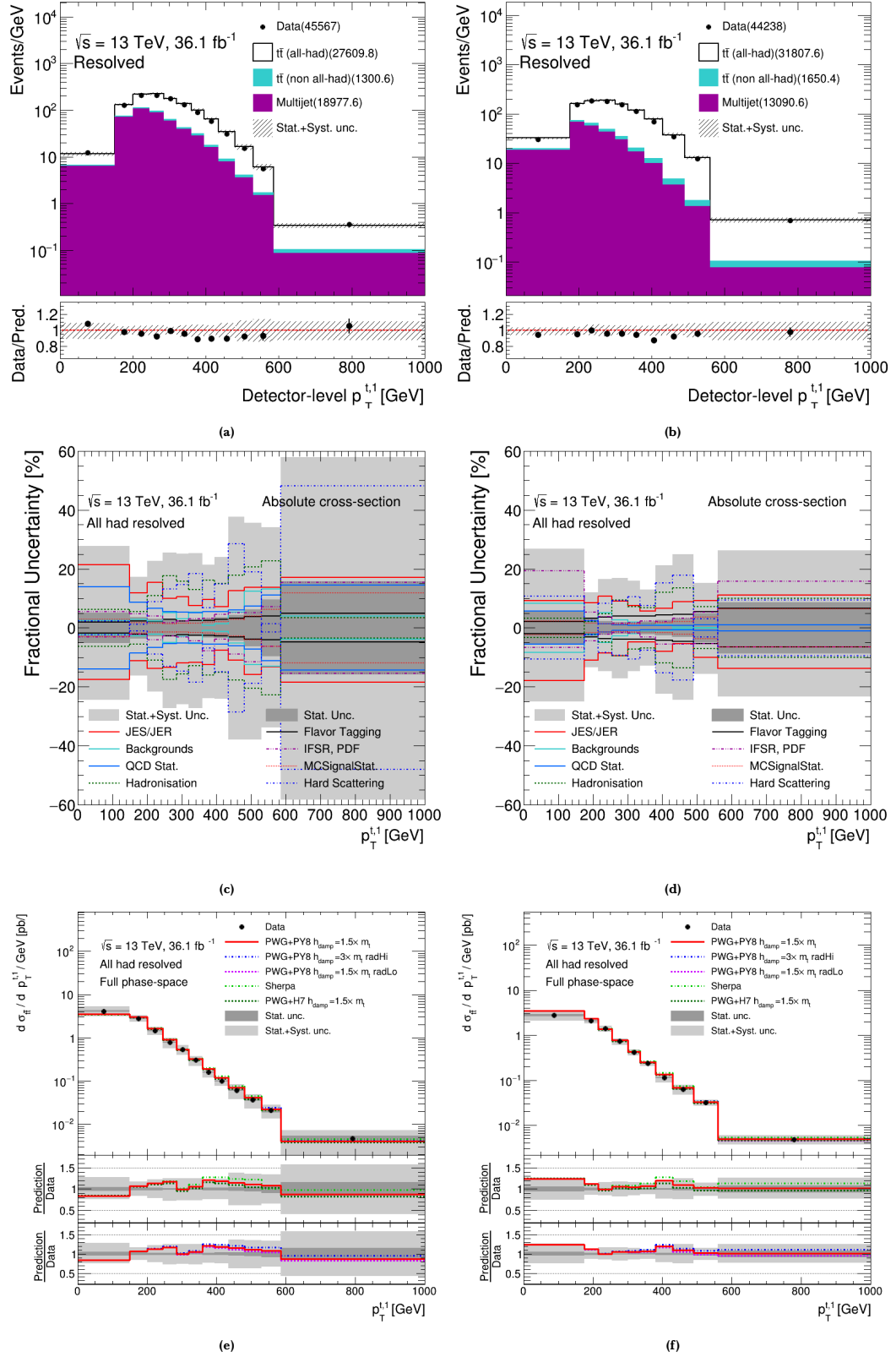


Figure 9.5: Detector-level distributions in the signal regions as a function of the leading top-quark candidate transverse momentum reconstructed with the KLFitter (a, c and e) and χ^2 (b, d, and f).

Background estimate

In this chapter, the procedure adopted to estimate the background component for the analysis is described. All the tables, figures and numbers presented have been produced in the context of the development of the work that lead to this thesis.

Two sources of background contribute to the event yield of the signal region of the resolved all-hadronic topology.

Multi-jet production forms the most significant source of background contamination. It contributes about a third of the total number of selected events. This contribution is estimated using a data-driven procedure, as described in Sec. 10.1.

The contribution of top-quark pairs decaying into non-hadronic final states is instead expected to be 5% of the predicted number of selected all-hadronic events and 3% of the total data yield. This contribution is estimated by requiring at least one leptonic W -boson decay in the same MC simulated samples as for the signal.

The total single-top-quark contribution is estimated to be below 2% of the selected data and well within both the MC and data statistical uncertainties. For this reason it is not considered further.

10.1 Data-driven estimate of multi-jet background

The estimate of the multi-jet background component uses an *ABCD method*. This method involves two variables which provide good signal-background discrimination, while having uncorrelated distributions in the background process.

The pair of discriminating variables are the b -jet multiplicity ($N_{b\text{-jets}}$) and a

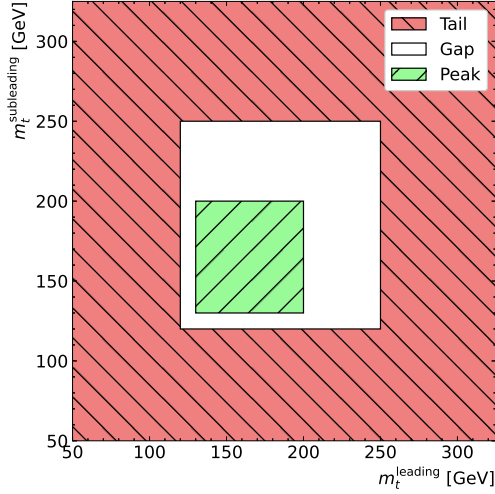


Figure 10.1: Partition of the two-dimensional mass region based on the masses of the leading- and sub-leading top-quark candidates.

Mass region	Condition
Tail	At least one top quark with $m_t < 120$ GeV or $m_t > 250$ GeV
Peak	Both top quarks have $130 \text{ GeV} < m_t < 200 \text{ GeV}$
Gap	Otherwise

Table 10.1: Definition of the mass region based on the m_t of the two top-quark candidates.

custom variable which combines the masses of the two top-quark candidates. Specifically, the two top-quark masses are used to define two different mass regions with an intermediate gap in-between.

The mass regions are defined in Tab. 10.1 and shown in Fig. 10.1.

The *peak* mass region requires the mass of both top-quark candidates to be in the range $130 \text{ GeV} < m_t < 200 \text{ GeV}$. The *tail* mass region requires the mass of at least one top-quark candidate to be either below 120 GeV or above 250 GeV. While the intermediate *gap* region sits between the other two.

To improve the robustness of the estimate, events where the two top-quark candidates do not belong to either the peak or tail mass region are excluded. In these events, the top-quark candidates fall in the intermediate region, ranging within either $120 \text{ GeV} < m_t < 130 \text{ GeV}$ or $200 \text{ GeV} < m_t < 250 \text{ GeV}$. Their exclusion strongly reduces the signal contamination in the control regions with a negligible increase in the total statistical uncertainty.

The various combinations of b -jet multiplicity and mass region are used to

	Tail	Peak	Gap
$N_{b\text{-jets}} = 0$	A_0	B_0	G_0
$N_{b\text{-jets}} = 1$	A_1	B_1	G_1
$N_{b\text{-jets}} = 2$	C	D	G_2

Table 10.2: Division into orthogonal regions according to the $N_{b\text{-jets}}$ variable and a combination of the two top-quark masses as defined in Tab. 10.1.

identify six orthogonal regions (Tab. 10.2). Other than the usual four regions of the ABCD method, two more regions are defined to assess the systematic uncertainty for this method. For the definition of these six regions, the criteria summarised in Tab. 9.1 are also applied.

The signal region D is characterised by $N_{b\text{-jets}} = 2$ and $130 \text{ GeV} < m_t < 200 \text{ GeV}$ for both top-quark candidates. The background control regions are characterised by having either a lower b -jet multiplicity or a different mass region, or both.

The background yields in the control regions are determined bin-by-bin for each differential distribution by subtracting from the data yields the MC $t\bar{t}$ predictions of the $t\bar{t}$ all-hadronic and non-all-hadronic decay modes.

The estimate of the background yield in the signal region D is carried out using the $N_{b\text{-jets}} = 1$ regions as

$$D(X) = \frac{B_1(X) \cdot C(X)}{A_1(X)}, \quad (10.1)$$

where $A_1(X)$, $B_1(X)$ and $C(X)$ represent the background yields for a generic observable X in their respective control regions.

A parallel estimate D' is also carried out using the $N_{b\text{-jets}} = 0$ to assess the systematic uncertainty of the method. This estimate accounts for potential differences between the kinematic properties of the various flavour components of the multi-jet background, and it is defined as

$$D'(X) = \frac{B_0(X) \cdot C(X)}{A_0(X)}. \quad (10.2)$$

Finally, the systematic uncertainty of the nominal prediction D is given by the

Region	Definition	All-hadronic $t\bar{t}$ /Data	Non all-hadronic $t\bar{t}$ /Data
A_0	$N_{b\text{-jets}} = 0$ tail	1.87%	0.19%
B_0	$N_{b\text{-jets}} = 0$ peak	0.96%	0.08%
G_0	$N_{b\text{-jets}} = 0$ gap	0.45%	0.06%
A_1	$N_{b\text{-jets}} = 1$ tail	3.35%	0.69%
B_1	$N_{b\text{-jets}} = 1$ peak	16.1%	1.16%
G_1	$N_{b\text{-jets}} = 1$ gap	6.86%	0.96%
C	$N_{b\text{-jets}} = 2$ tail	16.1%	2.90%
D	$N_{b\text{-jets}} = 2$ peak	66.1%	3.35%
G_2	$N_{b\text{-jets}} = 2$ gap	33.9%	4.21%

Table 10.3: Fractional yields with respect to data from top-quark pair production processes in the different regions, defined by the values assumed by $N_{b\text{-jets}}$ and the two top-quark masses as defined in Tab. 10.1.

difference between the two estimates D and D' :

$$\Delta D = D' - D. \quad (10.3)$$

For each region, Tab. 10.3 shows the fraction of signal and background $t\bar{t}$ events from MC simulation with respect to the data yield. More signal contamination is observed in regions with b -tagged jets, but sufficient background purity is observed in all regions such that signal mismodelling should not substantially bias the background prediction.

The event yields after the signal region selection are shown in Tab. 10.4 for the simulated MC $t\bar{t}$ decay modes and the estimated background. The percentages are calculated with respect to the *total prediction*, which corresponds to the sum of all three contributions. The data event yield in the signal region is also shown.

In Tab. 10.4, uncertainties are quoted as the sum in quadrature of statistical and detector-level systematic uncertainties. The composition of the selected events is also given in terms of the fractional contribution of the signal and background processes to the total yield.

The complete cutflows for data and simulated top quark events are listed in Tab. 10.5, showing a signal efficiency of about 0.2%.

Process	Event yield	Fraction
$t\bar{t}$ (all-hadronic)	$29\,500^{+2000}_{-2500}$	68%
$t\bar{t}$ (non-all-hadronic)	1490^{+140}_{-120}	3%
Multi-jet background	$12\,600^{+1900}_{-1900}$	29%
Total prediction	$43\,500^{+2800}_{-3000}$	100%
Data	44 621	

Table 10.4: Event yields for data, signal and background processes after the signal region selection.

10.1.1 Multi-jet fractions

Fig. 10.2 to Fig. 10.3 present the ratio of multi-jet events over the total prediction for measured differential cross-section distributions.

10.2 Distributions of signal region selecting variables

As mentioned in Sec. 9.1, the observables used to define the signal region are χ^2_{\min} , ΔR_{bb} and ΔR_{bW}^{\max} . Their spectra are presented in Fig. 10.4 in an $N - 1$ requirement configuration, where the plot for a particular variable is made after applying all signal region requirements except the one on the variable being displayed.

The top-quark candidates mass spectra are not shown since those observables are used to define the control regions in the multi-jet estimation.

Although the total predicted event yields do not perfectly reproduce the data distributions everywhere, they are compatible with data within the sum in quadrature of the uncertainties, given for illustrative purposes by the sum of statistical and dominant systematic components. The dominant source of uncertainties in the six-jet case is the $t\bar{t}$ theoretical modelling (parton shower and initial-state radiation), whereas the systematic uncertainty of the multi-jet estimate dominates the inclusive jet distributions. Together, the comparisons indicate an adequate description of the signal and background processes.

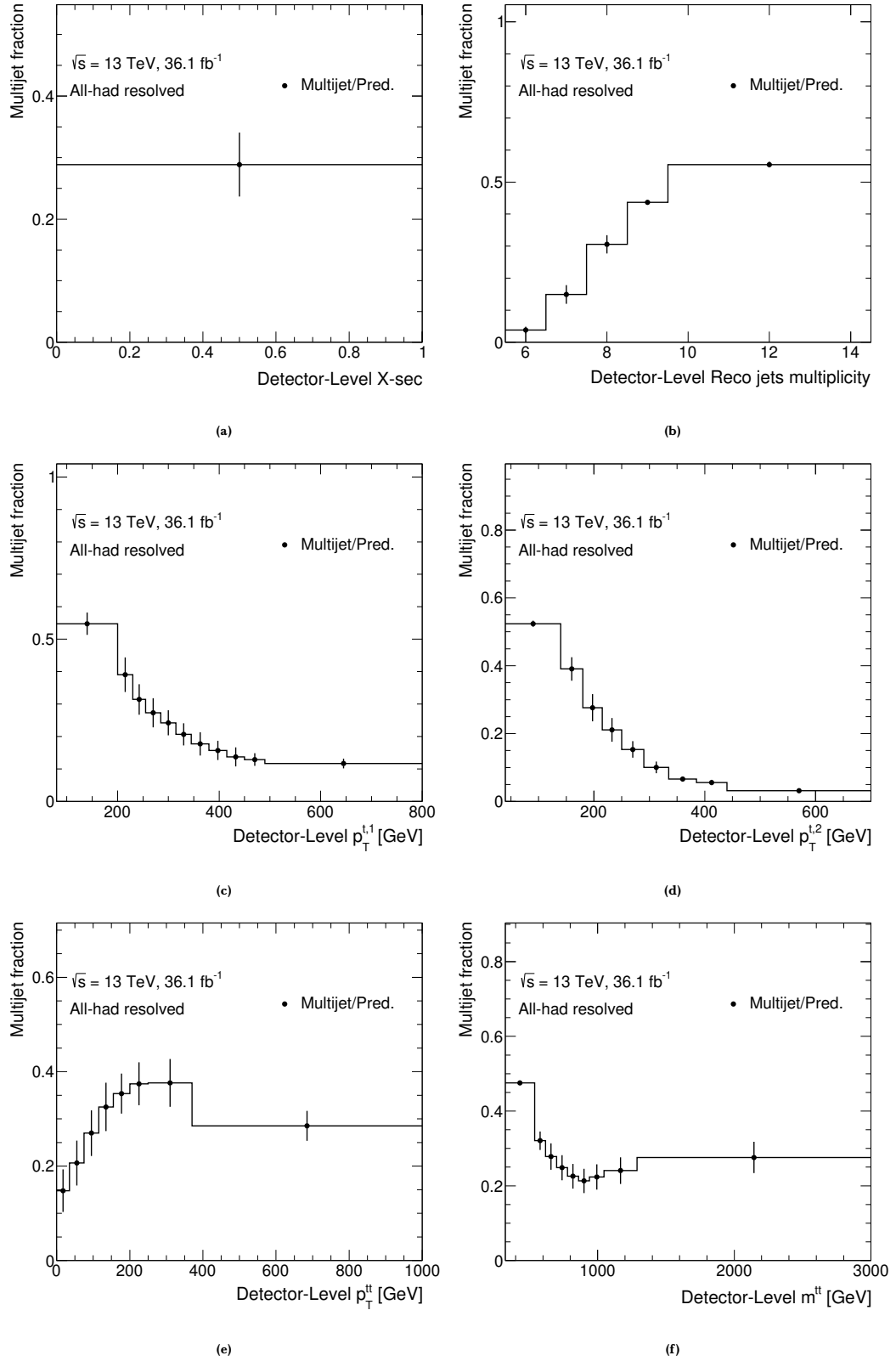


Figure 10.2: Ratio of the multi-jet background over total prediction as a function of (a) $\sigma_{t\bar{t}}$, (b) N_{jets} , (c) $p_T^{t,1}$, (d) $p_T^{t,2}$, (e) $p_T^{t\bar{t}}$ and (f) $m^{t\bar{t}}$. The error bar represents the systematic uncertainty on the multi-jet estimation.

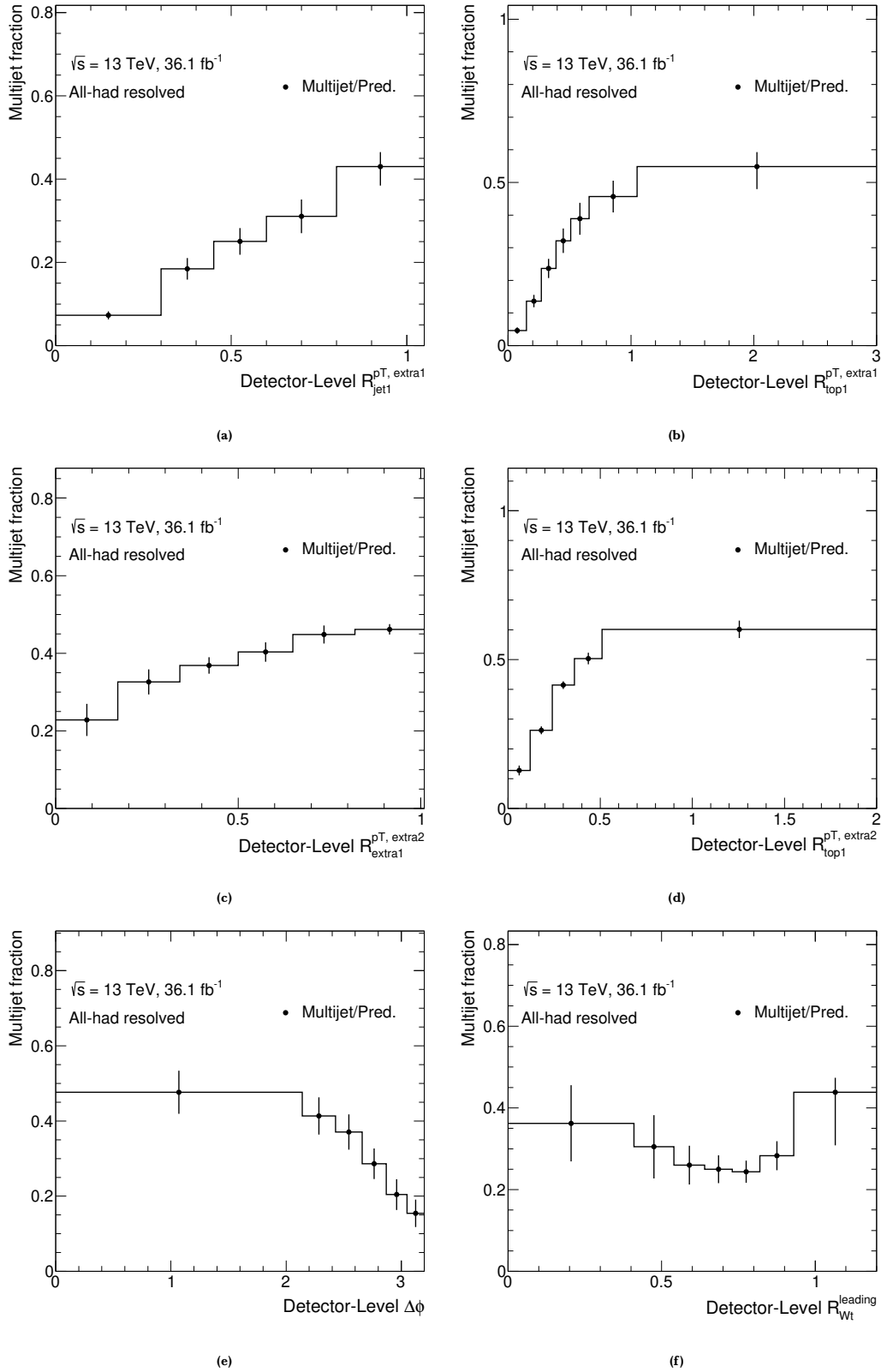


Figure 10.3: Ratio of the multi-jet background over total prediction as a function of (a) R_{jet1}^{extra1} , (b) $R_{t,1}^{extra1}$, (c) $\Delta R_{extra1}^{extra2}$, (d) $R_{t,1}^{extra2}$, (e) $\Delta\phi^{t\bar{t}}$ and (f) $R_{Wt}^{leading}$. The error bar represents the systematic uncertainty on the multi-jet estimation.

Requirement	Data	$t\bar{t}$ all-hadronic signal	$t\bar{t}$ non all-hadronic
Initial	$4.533\,88 \times 10^8$	$1.369\,86 \times 10^7 \pm 2.218 \times 10^3$	$1.631\,18 \times 10^7 \pm 1.527 \times 10^3$
GoodRunList	$4.431\,66 \times 10^8$	$1.369\,86 \times 10^7 \pm 2.218 \times 10^3$	$1.631\,18 \times 10^7 \pm 1.527 \times 10^3$
Good Calorimeter	$4.425\,44 \times 10^8$	$1.369\,86 \times 10^7 \pm 2.218 \times 10^3$	$1.631\,18 \times 10^7 \pm 1.527 \times 10^3$
Primary Vertex	$4.425\,44 \times 10^8$	$1.369\,86 \times 10^7 \pm 2.218 \times 10^3$	$1.631\,18 \times 10^7 \pm 1.527 \times 10^3$
Trigger decision	$5.155\,15 \times 10^7$	$9.531\,70 \times 10^5 \pm 5.850 \times 10^2$	$3.937\,79 \times 10^5 \pm 2.370 \times 10^2$
Jet Clean Loose Bad	$5.152\,60 \times 10^7$	$9.529\,62 \times 10^5 \pm 5.850 \times 10^2$	$3.936\,94 \times 10^5 \pm 2.370 \times 10^2$
Exactly 0 leptons	$5.038\,20 \times 10^7$	$9.215\,03 \times 10^5 \pm 5.753 \times 10^2$	$1.692\,75 \times 10^5 \pm 1.553 \times 10^2$
At least 6 jets	$1.603\,37 \times 10^7$	$3.732\,40 \times 10^5 \pm 3.668 \times 10^2$	$6.463\,92 \times 10^4 \pm 9.615 \times 10^1$
Exactly 2 b -jets	$1.103\,13 \times 10^6$	$1.480\,06 \times 10^5 \pm 3.847 \times 10^2$	$2.661\,14 \times 10^4 \pm 1.631 \times 10^2$
Reconstructed χ^2_{\min}	$3.317\,17 \times 10^5$	$8.090\,41 \times 10^4 \pm 2.844 \times 10^2$	$8.796\,29 \times 10^3 \pm 9.379 \times 10^1$
ΔR_{bb}	$1.559\,94 \times 10^5$	$5.637\,70 \times 10^4 \pm 2.374 \times 10^2$	$5.420\,53 \times 10^3 \pm 7.362 \times 10^1$
ΔR_{bW}^{\max}	$7.265\,70 \times 10^4$	$3.722\,16 \times 10^4 \pm 1.929 \times 10^2$	$2.539\,44 \times 10^3 \pm 5.039 \times 10^1$
Top Mass	$4.462\,10 \times 10^4$	$2.944\,01 \times 10^4 \pm 1.716 \times 10^2$	$1.491\,92 \times 10^3 \pm 3.863 \times 10^1$

Table 10.5: Complete cutflow for data, signal and background Monte Carlo. Only statistical uncertainties are given.

10.3 Multi-jet background for different jet multiplicities

Fig. 10.5 shows the jet multiplicity distribution for selected events in data compared with the total SM prediction.

The background is the sum of the data-driven multi-jet estimate and the MC-based expectation for the contributions of non-all-hadronic $t\bar{t}$ production processes.

This demonstrates that the six-jet bin is essentially pure $t\bar{t}$, with negligible background contamination, and in fact the nominal MC signal yield slightly exceeds the data yield. In higher jet multiplicity bins the combinatorial difficulty in correctly identifying the jets from the top-quark decays increases, resulting in a growing multi-jet background contribution.

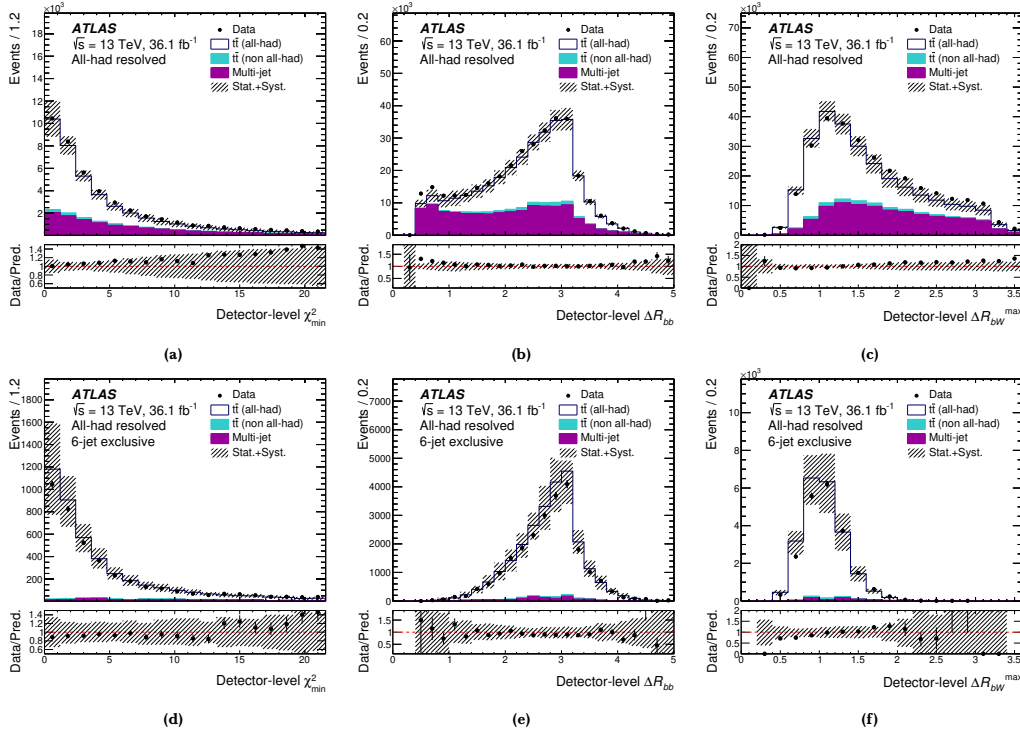


Figure 10.4: Detector-level distributions in the signal regions as a function of the χ^2_{\min} (left), ΔR_{bb} (middle) and ΔR_{bW}^{\max} (right) for all selected events (top) and exclusive six-jet events (bottom). Statistical uncertainties combined with the dominant systematic uncertainties for the applied selection are shown in hatching. Overflow events are included in the last bins.

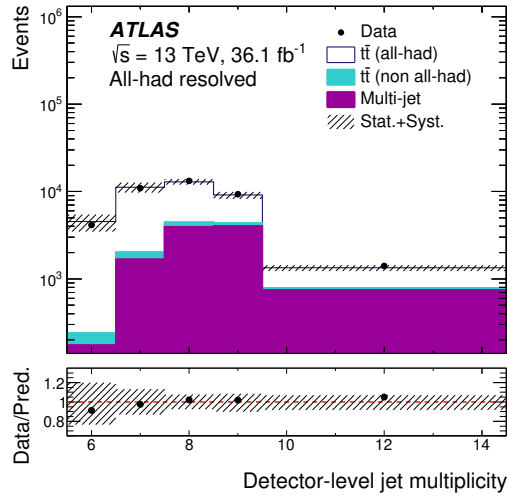


Figure 10.5: Jet multiplicity in the signal region. Statistical uncertainties combined with systematic uncertainties are shown in hatching. Overflow events are included in the last bin.

Unfolding

In this chapter, the unfolding steps of the analysis are described. My contribution has consisted in the production of the input for the first step of the iterative method adopted.

The observables distributions reconstructed from data are transformed using an *unfolding* procedure to correct for detector and reconstruction effects.

The iterative Bayesian unfolding method is used. Then the corrections are applied. All corrections are evaluated using the nominal MC $t\bar{t}$ simulation.

11.1 Iterative Bayesian method

The bayesian probability for a cause C_i given a specific effect E can be expressed as

$$P(C_i|E) = \frac{P(E|C_i)P(C_i)}{\sum_{l=1}^{n_C} P(E|C_l)P(C_l)}, \quad (11.1)$$

which can be interpreted as being proportional to the probability of the cause multiplied by the probability of the cause to produce the effect.

The causes C_i correspond to events in the true bins, while effects E_j correspond to events in the reconstructed bins. Only the events E_j can be measured and it is impossible to determine unequivocally the cause that generated it.

Given the observation of $n(E)$ events with effect E , the expected number of events that can be assigned to a cause C_i is

$$\hat{n}(C_i) = n(E)P(C_i|E), \quad (11.2)$$

where the conditional probability $P(C_i|E)$ describes the cell-to-cell migration.

In the case of n_E possible effects, Eq. (11.1) can be rewritten as

$$P(C_i|E_j) = \frac{P(C_i|E_j)P_0(C_i)}{\sum_{l=1}^{n_C} P(E|C_l)P_0(C_l)}, \quad (11.3)$$

where $P_0(C_i)$ is an a-priori probability of the cause C_i .

The number of events that can be assigned to each cause can be estimated as

$$\hat{n}(C_i) = \frac{1}{\epsilon_i} \sum_{j=1}^{n_E} n(E_j)P(C_i|E_j) \quad \epsilon_i \neq 0, \quad (11.4)$$

where ϵ_i as also be introduced as the efficiency of the selection of the bin i . If $\epsilon_i = 0$ then $\hat{n}(C_i)$ is set to zero, since it means that the experiment is not sensitive to the cause C_i .

Using Eq. (11.3), Eq. (11.4) can be rewritten as

$$\hat{n}(C_i) = \sum_{j=1}^{n_E} M_{ij}n(E_j), \quad (11.5)$$

where M_{ij} is the *unfolding matrix*, defined as

$$M_{ij} = \frac{P(E_j|C_i)P_0(C_i)}{[\sum_{l=1}^{n_E} P(E_l|C_i)][\sum_{l=1}^{n_C} P(E_j|C_l)P_0(C_l)]}. \quad (11.6)$$

An a-posteriori probability of a given cause C_i can be evaluated as

$$\hat{P}(C_i) = \frac{\hat{n}(C_i)}{\sum_{j=1}^{n_E} \hat{n}(C_j)}. \quad (11.7)$$

To obtain a stable solution, the bayesian method is repeated iteratively. A polynomial fit of the posteriori solution is carried out and used in the following iteration as an a-priori solution. The algorithm is stable and at each iteration the estimate is improved.

11.2 Unfolding at particle level

The differential cross-section distributions are unfolded to particle level using the migration matrix as defined in the previous section. Prior to this however, an acceptance correction is applied. This correction is a bin-by-bin factor which corrects for events that are generated outside the fiducial phase-space region but pass the reconstruction-level selection.

The expression of the acceptance correction f_{acc}^j , for the bin j , is defined as the fraction of events which passes both the detector- and particle-level selections over the number of events which passes only the detector-level selection:

$$f_{\text{acc}}^j \equiv \frac{N_{\text{reco} \wedge \text{particle}}^j}{N_{\text{reco}}^j}. \quad (11.8)$$

The resulting distribution is then unfolded to the particle level.

The migration matrix used as input to the unfolding is derived from simulated $t\bar{t}$ samples. The matrix maps the particle-level bin i in which an event falls to the bin j in which it is reconstructed. The probability for particle-level events to be reconstructed in the same bin is represented by the elements on the diagonal, and the off-diagonal elements describe the fraction of particle-level events that migrate into other bins.

The unfolding is performed using four iterations to balance the unfolding stability relative to the previous iteration and the growth of the statistical uncertainty, which is limited to be below 0.1%.

Finally, the efficiency factor ϵ is applied to the unfolded spectrum to correct for the inefficiency of the event selection and reconstruction.

This efficiency correction is applied bin-by-bin to the fiducial phase space. For a given bin i , it is defined as the fraction of the events generated in a particle-level bin i which passes the inclusive reconstruction-level selection:

$$\epsilon^i \equiv \frac{N_{\text{reco} \wedge \text{particle}}^i}{N_{\text{particle}}^i}. \quad (11.9)$$

The extraction of the absolute differential cross-section for an observable X at particle level is then summarised by the following expression:

$$\frac{d\sigma^{\text{fid}}}{dX^i} \equiv \frac{1}{\mathcal{L} \cdot \Delta X^i} \cdot \frac{1}{\epsilon^i} \cdot \sum_j \mathcal{M}^{-1} \cdot f_{\text{acc}}^j \cdot \left(N_{\text{obs}}^j - N_{\text{bkg}}^j \right), \quad (11.10)$$

where the index j iterates over bins of observable X at reconstruction level while the index i labels bins at particle level, ΔX^i is the bin width, \mathcal{L} is the integrated luminosity, and the inverted migration matrix as obtained with the iterative unfolding procedure is symbolised by \mathcal{M}^{-1} . The integrated fiducial cross-section is obtained by integrating the unfolded cross-section over the bins,

and its value is used to compute the normalised differential cross-sections:

$$\frac{1}{\sigma^{\text{fid}}} \cdot \frac{d\sigma^{\text{fid}}}{dX^i}. \quad (11.11)$$

11.3 Unfolding at parton level

The measurements are extrapolated to the full phase space of the $t\bar{t}$ system using the same procedure as extrapolation to the fiducial phase space.

The binning is re-optimised because of the different resolution, leading to similar migration matrices.

Since the measurements are unfolded to the full phase space the acceptance correction is irrelevant, but large efficiency corrections are still needed due to the larger extrapolation.

The extraction of the absolute differential cross-section for an observable X at particle level is then summarised by the following expression:

$$\frac{d\sigma^{\text{full}}}{dX^i} \equiv \frac{1}{\mathcal{L} \cdot \mathcal{B} \cdot \Delta X^i} \cdot \frac{1}{\epsilon^i} \cdot \sum_j \mathcal{M}^{-1} \cdot \left(N_{\text{obs}}^j - N_{\text{bkg}}^j \right), \quad (11.12)$$

where the index j iterates over bins of observable X at reconstruction level while the index i labels bins at the parton level, ΔX^i is the bin width, $\mathcal{B} = 0.456$ is the all-hadronic branching ratio, \mathcal{L} is the integrated luminosity, and the inverted migration matrix as obtained with the iterative unfolding procedure is symbolised by \mathcal{M}^{-1} .

Systematic uncertainties

In this chapter the techniques used to estimate the systematic uncertainties affecting the measurements are described.

The measured differential cross sections are affected by several sources of systematic uncertainties.

To evaluate the uncertainties for a considered source, a bin-by-bin variation of the nominal distribution by one standard deviation is generated. Whenever available, upward and downward variations are evaluated separately. Otherwise in case of a single variation, the single deviation is symmetrised.

Total predictions are computed for both nominal and systematically varied samples. These predictions are the sum of the all-hadronic signal, the non-all-hadronic contribution and the multi-jet background.

The uncertainty is evaluated as the difference between the nominal and the systematically varied total prediction: $\Delta S_{\text{syst}} = T_{\text{syst}} - T_{\text{nominal}}$. Using the total prediction instead of solely the signal samples takes into account the effect of the uncertainties in the background yield. Furthermore, for the estimate of the uncertainty in the signal modelling, the non-all-hadronic events and the multi-jet events are considered fully correlated with the all-hadronic signal sample.

The varied MC detector-level spectrum is then unfolded using the background subtraction and corrections evaluated with the nominal $t\bar{t}$ signal sample and the unfolded result is compared with the corresponding particle- or parton-level distribution.

All detector- and background-related systematic uncertainties are evaluated using the nominal MC generator. As described in Sec. 7.2, alternative generators are used to assess the systematic uncertainties related to the $t\bar{t}$ system modelling.

12.1 Experimental uncertainties

The experimental uncertainties cover empirical uncertainties in object reconstruction and calibration and also the confidence to which the simulated detector response is able to reproduce experimental data for the reconstructed objects.

The impact of a systematic uncertainty is evaluated by replacing the nominal MC prediction for signal and non-all-hadronic $t\bar{t}$ background with their systematic variations. The multi-jet background is then re-estimated and the data is unfolded using the nominal correction factors.

Due to the selected final state, the main experimental systematic uncertainties arise from jet reconstruction and flavour tagging. As events with leptons are removed, the uncertainties associated with lepton reconstruction and identification are negligible.

The uncertainty on the integrated luminosity combining data from 2015 and 2016 is 2.1%.

12.1.1 Jet reconstruction

The uncertainty in the JES was estimated by using a combination of simulation, test beam data and in situ measurements [76].

The JES uncertainty takes into account 29 independent sub-components, among which there are contributions from jet flavour composition, η -intercalibration, punch-through, single-particle response, calorimeter response to different jet flavours and pile-up.

The JER systematic uncertainty is due to the difference between data and MC events. It is evaluated by smearing the MC jet transverse momentum according to the jet resolution as a function of the jet p_T and η .

The uncertainty due to the JVT criterion efficiency was determined from efficiency measurements made on $Z \rightarrow ee/\mu\mu + \text{jets}$ [77] events that are applied as variations of the jet-by-jet efficiency corrections.

Given the all-hadronic final state, the JES modelling is the most important source of experimental uncertainties, contributing at the 5–10% level. The JER systematics are usually at the level of 1%, except where inflated by the statistical uncertainties.

12.1.2 *b*-tagging

The systematic uncertainties related to tagging jets originating from *b*-quarks are separated into three categories: the tagging algorithm efficiency to correctly tag *b*-initiated jets, the rates for misidentification of jets initiated by *c*-quarks and the rates of misidentification for jets originating from light-quark flavours.

These efficiencies were estimated from data and parameterised as a function of p_T and η [78]. And the uncertainties arise from scale factors that are used to correct for the differences between the data and MC. The uncertainties in the simulation modelling of the *b*-tagging performance are assessed by studying *b*-jets in dileptonic $t\bar{t}$ events.

The systematic uncertainties of the *c*-jet and light-jet tagging efficiencies are generally at the sub-percent level. The uncertainty in the *b*-jet tagging efficiency contribute about 5% at the most.

12.2 Signal modelling uncertainties

The specific MC generator used to model the signal has repercussions on the kinematic properties of the simulated $t\bar{t}$ events, the reconstruction efficiencies and the estimate of the multi-jet background.

12.2.1 Matrix element and parton shower

Different generator configurations are used to evaluate the impact of adopting different NLO matrix element calculations, parton shower models and hadronisation models. Both signal and background $t\bar{t}$ events are simulated with configurations different from the nominal one, while the detector simulation is kept consistent for both the nominal and the systematic variations.

The uncertainty due to the generator choice is determined by unfolding a sample generated with MADGRAPH5_aMC@NLO+PYTHIA8 while using corrections and response matrices derived from the nominal sample. The unfolded result is compared with the truth-level spectrum of the MADGRAPH5_aMC@NLO+PYTHIA8 sample and the relative difference is used as systematic uncertainty for the ME generator choice.

Analogously, the uncertainty due to the choice of the parton shower and hadronisation models is determined by unfolding a sample generated with POWHEG+HERWIG7 while using corrections and response matrices from the nominal sample. The unfolded result is again compared with the truth-level spectrum of the POWHEG+HERWIG7 sample and the relative difference is used as the systematic uncertainty for the parton shower and hadronisation choice.

The ME element and modelling systematic uncertainties are found to depend strongly on the variable being evaluated and, among all systematic uncertainties, the matrix element and parton shower variations are the most significant sources of systematic uncertainty. Although for most distributions the effect is at the percent level, in a few cases they affect the tails of the distributions by up to 20%.

12.2.2 Sample size

Pseudo-experiments are used to evaluate the impact of the limited size of the signal MC sample. The event yield in each bin is generated from a Gaussian distribution with mean equal to the bin yield and standard deviation equal to the Poisson uncertainty of the bin yield. The obtained smeared spectrum is then unfolded and the procedure is repeated 10 000 times.

The final statistical uncertainty is evaluated as the difference between the nominal prediction and the average result of the 10 000 pseudo-experiments. The resulting systematic uncertainty was found to be typically below 0.5%, increasing to 1–2% in the tails of some distributions.

12.2.3 Initial-state QCD radiation

$t\bar{t}$ MC samples with modified ISR modelling are used to evaluate its corresponding uncertainty. In particular, the unfolding was performed on samples generated similarly to the nominal sample but with the factorisation and renormalisation scales as well as the value of the h_{damp} parameter varied as described in Sec. 7.2.

The upward and downward variations spectra are unfolded and the corresponding uncertainties are evaluated by comparing the nominal sample with the truth-level spectrum of the ISR samples. Overall, this uncertainty contributes at the level of a few percent for most bins, thus making the ISR variations comparable to the parton shower and matrix element uncertainties.

12.2.4 Parton distribution functions

The impact of the choice of different PDF sets was assessed using the 30-eigenvector set of the PDF4LHC15 prescription [79].

The PDF choice affects the corrections used to correct the spectrum at the detector level to the particle level. The effect of the PDF choice was evaluated by unfolding the nominal POWHEG+PYTHIA8 sample using differently PDF-reweighted corrections.

Unfolded results are then compared with the known central spectrum, obtaining intra-PDF variations which are added in quadrature to define the relative uncertainty as

$$\delta_{\text{intra}} \equiv \frac{\sqrt{\sum_{i \in \text{PDF4LHC15}} (U_i \cdot R_0 - T_0)^2}}{T_0}, \quad (12.1)$$

where the i index iterates over the PDF4LHC15 varied PDF set while the 0 subscript denotes its central set, R represents the distribution at the detector level while T symbolises the distribution at the particle level, and the unfolding procedure is represented by the U factor.

Additionally, a relative inter-PDF variation between NNPDF3.0NLO and the PDF4LHC15 central PDF sets is also evaluated as

$$\delta_{\text{inter}} \equiv \frac{U_{\text{NNPDF3.0NLO}} \cdot R_0 - T_0}{T_0}. \quad (12.2)$$

The PDF uncertainties result to be below the percent level, except for a few variables distributions where bins that are lowly populated show the uncertainty at the level of 1–2%.

12.3 Background modelling uncertainties

The multi-jet background predictions has two sources of uncertainty. One is related to the finite amount of statistics used, while the other represents the intrinsic error of the data-driven method used for the estimate.

The uncertainty related to the finite number of events is evaluated in an analogous way as for the MC sample size, where 10 000 pseudo-experiments are carried out and the average result is then compared to the nominal prediction.

The uncertainty related to the error of the ABCD method is evaluated by comparison with an alternative background prediction. The alternative prediction, corresponding to Eq. (10.2), substitutes the 0- b -tag control regions for the 1- b -tag control regions. And the background systematic error is given by the difference between the unfolded distributions in the two scenarios.

The statistical uncertainty of the multi-jet background estimation is small, usually under 5%. The systematic uncertainty is usually sub-dominant to uncertainties from modelling and JES/JER, occasionally reaching 10%. In a few specific bins the systematic uncertainty can be larger due to a higher background contamination, which amplifies the contribution of the background and the corresponding systematic uncertainty.

Finally, the impact of using a fixed total $t\bar{t}$ cross-section when computing the

Source	Uncertainty [%]	
	Particle level	Parton level
PS/hadronisation	8.2	7.9
Multi-jet syst.	7.7	7.7
JES/JER	6.7	6.7
ISR, PDF	3.3	3.5
ME generator	2.4	5.3
Flavour tagging	2.2	2.2
Luminosity	2.1	2.1
Multi-jet stat.	0.6	0.6
MC signal stat.	0.3	0.3
Stat. unc.	0.7	0.7
Stat.+syst. unc.	14	15

Table 12.1: Summary of the main relative uncertainties in the inclusive cross-section measured at the particle and parton levels. The uncertainties are symmetrised.

background prediction is also evaluated. The nominal background estimation is compared to a variation where the normalisation is varied by the uncertainty of the inclusive cross-section, which in relative terms is 5.2%. The impact of this uncertainty in the measurement is very small, usually less than 1%, given that the background control regions have little contamination from signal.

12.4 Systematic uncertainties summary

A general overview of the dominant systematic uncertainties that affect the inclusive cross-section measurement at both particle and parton level are reported in Tab. 12.1. In the table, the systematic uncertainties are also grouped per type.

The dominant source of uncertainty at both particle and parton level is the hadronisation, followed by the contribution of the multi-jet estimation and the JES and JER uncertainties.

Results

In this chapter, the differential cross section results unfolded and compared with several MC predictions are reported with active contribution in the production of the figures of the ATLAS data and simulated SM predictions comparison.

The cross-section measurement results are presented as both absolute and normalised. The normalised results allow to compare only the shapes of the measured cross-sections and the predictions, reducing the contribution of uncertainties common to all bins of the distributions and highlighting the shape differences relative to the absolute case.

13.1 Data-MC agreement

The level of agreement between the measured data and the theoretical predictions is evaluated with a χ^2 test. The χ^2 variable is computed using the total covariance matrices of the measurement uncertainties, following the relation

$$\chi^2 = V^T \cdot \text{Cov}^{-1} \cdot V, \quad (13.1)$$

where Cov represents the covariance matrix, which incorporates the statistical uncertainty and the systematic uncertainties from detector, signal and background modelling; and each component of the vector V corresponds to the differences between the measured and predicted cross-sections for a bin of the distribution.

The p -values are used to quantify the probability of obtaining a χ^2 result as extreme as the observed value. The p -values are evaluated for each distribution from the observed χ^2 using as degrees of freedom the corresponding number of bins.

Differential cross-sections are obtained by unfolding each varied reconstructed distribution with the nominal corrections, and the results are used to compute the covariance matrix Cov .

For each differential cross-section, the covariance matrix Cov is obtained by performing pseudo-experiments.

First, each bin of the data distribution is varied according to a Poisson distribution, then gaussian-distributed shifts are added for each detector-modelling systematic uncertainty by the expected relative variation of the corresponding systematic uncertainty. The varied distribution is then unfolded with the nominal corrections. If the number of events in a given bin of a pseudo-experiment becomes negative due to the effect of the combined systematic shifts.

At this stage, after unfolding, additional Gaussian-distributed shifts are added for each signal-modelling systematic uncertainty, using the expected relative variations of the corresponding systematic uncertainty. Specifically, the signal-modelling relative variations are defined as the difference between the generated and the unfolded cross-section of a given alternative model, using nominal corrections in the unfolding. Finally, the resulting changes are used to compute the covariance matrix Cov .

For the calculation of covariance matrices associated to normalised differential cross-sections, the varied distributions are normalised to unity after all effects are included.

Furthermore, for normalised differential cross-sections, one of the bin of the distribution is discarded. Therefore, in the χ^2 formula (Eq. (13.1)), one of the component of the vector of differences between data and prediction V is removed and the covariant matrix used is the sub-matrix derived from the full covariance matrix of the normalised measurements by discarding the corresponding row and column is used. The sub-matrix so obtained is invertible and allows for the χ^2 to be computed.

The associated number of degrees of freedom for the χ^2 is the corresponding number of bins minus one. The choice of bin to be discarded does not affect the χ^2 value obtained.

Quantitative and qualitative comparison

Overall, the MC generator that gives the best description of several single-differential distributions is POWHEG+HERWIG7, followed by POWHEG+PYTHIA8. While MADGRAPH5_aMC@NLO+PYTHIA8 and the POWHEG+PYTHIA8 Var3cDown variation are the predictions showing the poorest agreement.

The results for the double-differential cross-sections demonstrate a general

	$p_T^{t,1}$		$p_T^{t,1}$		$R_{W_t}^{\text{leading}}$		$R_{\text{extra1}}^{\text{extra3}}$	
	χ^2/dof	$p\text{-value}$	χ^2/dof	$p\text{-value}$	χ^2/dof	$p\text{-value}$	χ^2/dof	$p\text{-value}$
PWG+PY8	22.7/11	0.02	20.5/9	0.01	12.6/7	0.08	2.9/6	0.82
PWG+PY8 Var. Up	19.5/11	0.05	11.0/9	0.27	15.1/7	0.03	4.9/6	0.55
PWG+PY8 Var. Down	27.2/11	<0.01	35.7/9	<0.01	13.7/7	0.06	2.8/6	0.83
aMC@NLO+PY8	14.6/11	0.20	34.7/9	<0.01	12.1/7	0.10	4.1/6	0.66
SHERPA	26.6/11	<0.01	2.3/9	0.99	112.5/7	0.08	3.7/6	0.72
PWG+H7	8.2/11	0.69	7.7/9	0.56	12.5/7	0.08	6.9/6	0.33

Table 13.1: Comparison for a selection of the measured particle-level absolute single-differential cross-sections with the predictions from several MC generators. For each prediction, a χ^2 and a p -value are calculated using the covariance matrix of the measured spectrum. The number of *degrees of freedom* (dof) is equal to the number of bins in the distribution.

larger difference between MC predictions. Analogously to the case of the single-differential distributions, POWHEG+HERWIG7 provides the best agreement overall, while MADGRAPH5_aMC@NLO+PYTHIA8 and the POWHEG+PYTHIA8 Var3cDown variation show the poorest agreement.

For the parton-level measurements, conclusions similar to those for the particle-level can be drawn. POWHEG+HERWIG7 and POWHEG+PYTHIA8 perform best in terms of reproducing the data, while MADGRAPH5_aMC@NLO+PYTHIA8 does not typically reflect the data.

As shown in Tab. 13.1, the two top-quark p_T observables are described within uncertainties only by POWHEG+HERWIG7 and the POWHEG+PYTHIA8 Var3cUp variation. While, considering the shape of the distributions, $R_{W_t}^{\text{leading}}$ is not well described by any MC prediction. $R_{\text{extra1}}^{\text{extra3}}$ is instead only described accurately by MADGRAPH5_aMC@NLO+PYTHIA8.

13.2 Results at particle level

Kinematic distributions

The single-differential cross-sections for the presented observables can be divided into two categories: the kinematic variables that are characteristic of the top-quark candidates or the top-quark pair system and the variables that compare the identified extra jets with the $t\bar{t}$ system kinematic properties.

The kinematic variables are the transverse momentum of the leading and sub-

leading top-quark candidates ($p_T^{t,1}$ and $p_T^{t,2}$), the top-quark pair p_T and mass ($p_T^{t\bar{t}}$ and $m^{t\bar{t}}$), the azimuthal angle between the two top-quark candidates ($\Delta\phi^{t\bar{t}}$), and the ratio between the p_T of the W boson coming from the leading top-quark candidate and its p_T (R_{Wt}^{leading}).

The extra-jets variables are the ratio between the extra jets p_T and the top-quark p_T ($R_{t,1}^{\text{extra1}}$, $R_{t,1}^{\text{extra2}}$ and $R_{t,1}^{\text{extra3}}$), the ration between the sub-leading extra jet p_T and the leading extra jet p_T ($R_{\text{extra1}}^{\text{extra2}}$), and the ΔR between the leading extra jet and the leading jet ($\Delta R_{\text{jet1}}^{\text{extra1}}$). These observables explicitly differentiate between jets from the top-quark pair system and additional radiation.

Fig. 13.1 shows the measured normalised differential cross-sections as a function of the leading and sub-leading top-quark transverse momenta. For illustration, these are shown alongside the detector-level distributions, which indicate good signal purity. For example, the leading top-quark transverse momentum shows a background contamination of 30% or less for $p_T^{t,1} > 200$ GeV. The breakdown of the systematic uncertainties is shown on Fig. 13.2.

The less collimated top-quark decays at low top-quark transverse momenta lead to a smaller signalbackground separation, which in the case of the sub-leading top-quark p_T distribution causes the background uncertainty to be dominant, whereas the radiation and PDF uncertainties are most important at large p_T .

In the case of the leading top-quark p_T , the dominant uncertainties are from theoretical sources at low p_T , mainly from the matrix element calculation, while at high p_T no individual uncertainty source dominates.

The uncertainties presented in the cross-section measurement distribution also show an analogous trend where the event generators predict a harder p_T spectrum than observed in data. And the slopes in the lower panels are significant compared to the uncertainty bands.

The data are mostly consistent with the predictions from SHERPA, POWHEG+HERWIG7 and POWHEG+PYTHIA8 with increased radiation.

In Fig. 13.3 is shown the particle-level absolute differential cross-section measurement for the leading top-quark p_T , which can be compared with the normalised measurement shown in Fig. 13.1b. The comparison shows how the normalisation reduces the total uncertainties, improving the sensitivity to the mismodelling of the distributions. In particular, the mismodelling originating from the parton shower and hadronisation.

In Fig. 13.4 are shown two features of the $t\bar{t}$ system, the top-quark pair transverse momentum and the top-quark pair mass. The $p_T^{t\bar{t}}$ distribution agrees well with the nominal POWHEG+PYTHIA8 prediction, but there are substantial deviations from the MADGRAPH5_aMC@NLO+PYTHIA8 and SHERPA predictions,

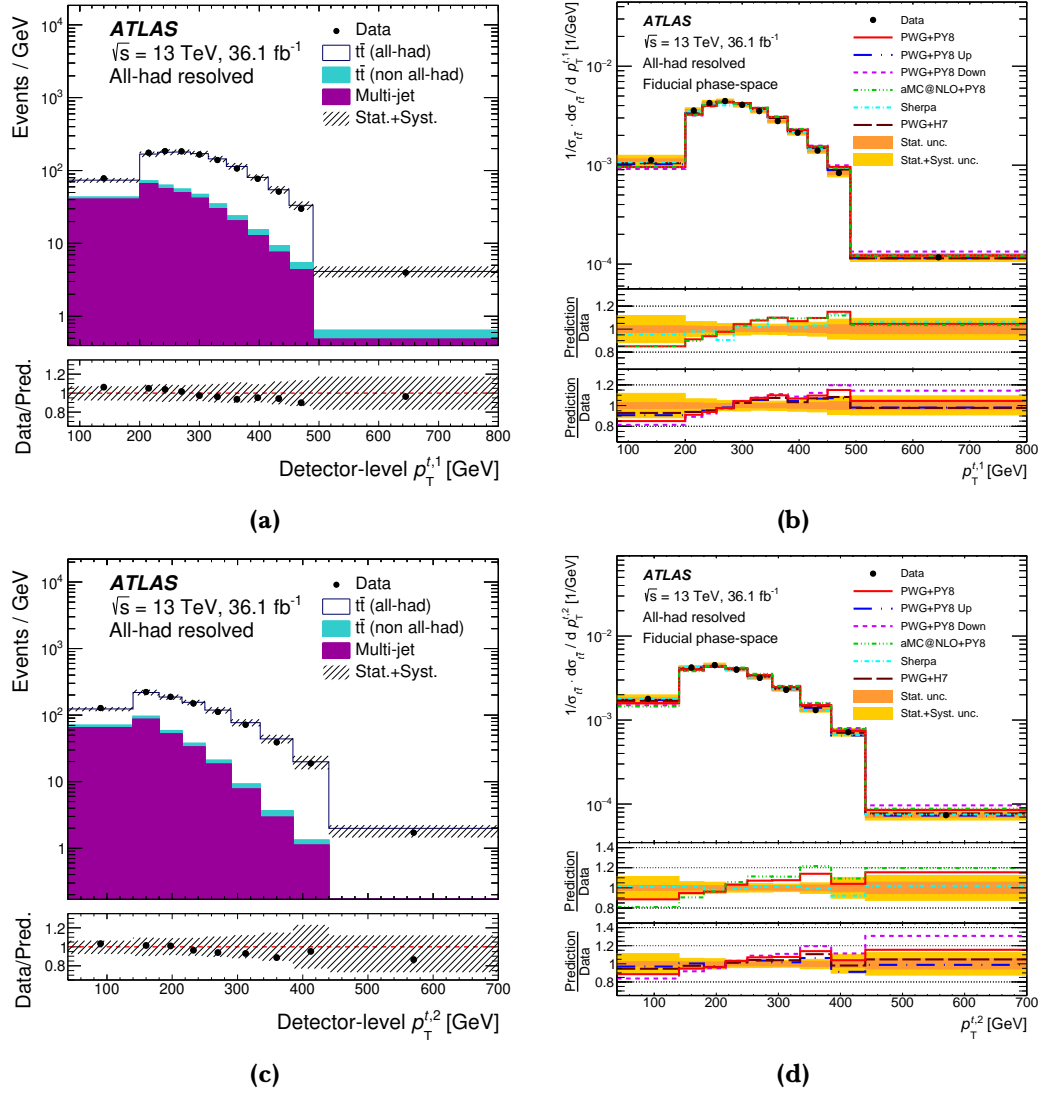


Figure 13.1: Comparison of ATLAS data with MC predictions for the (a) leading and (c) sub-leading top-quark transverse momenta. Single-differential normalised cross-section measurements are unfolded at particle level as a function of the (b) leading and (d) sub-leading top-quark transverse momenta. Overflow events are included in the last bin of every distribution shown.

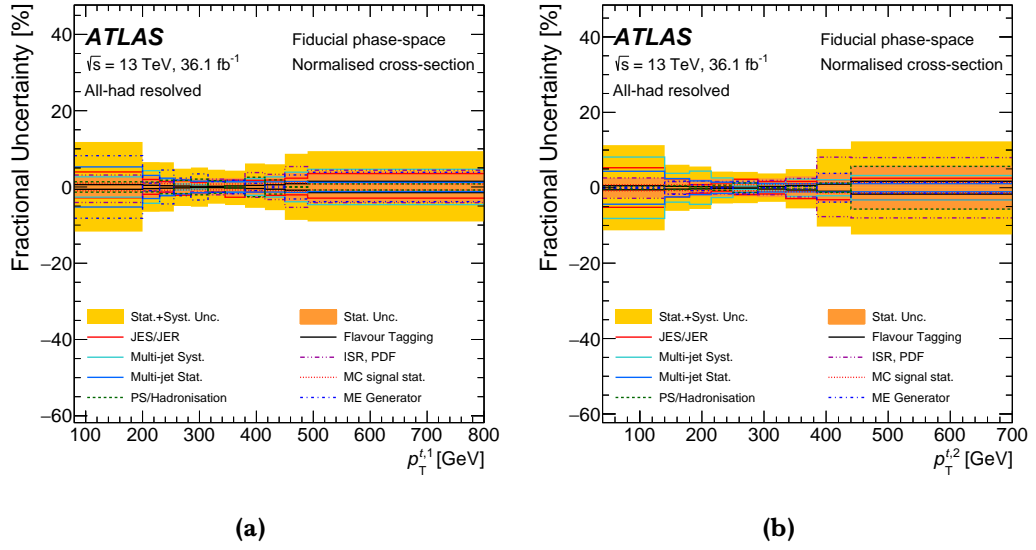


Figure 13.2: Fractional uncertainties for the normalised single-differential distributions unfolded at particle level as a function of the (a) leading and (b) sub-leading top-quark transverse momenta.

which predict spectra that are respectively too soft and too hard at high $p_T^{t\bar{t}}$.

The POWHEG+PYTHIA8 Var3cUp variation is also harder than the data, which is at odds with what is seen for the top-quark transverse momenta in Fig. 13.1, where this generator configuration reproduces the data better than the nominal POWHEG+PYTHIA8 configuration.

The $m^{t\bar{t}}$ distribution shows the same trends as already observed in the individual top-quark p_T distributions. This is consistent with expectations, since for central top-quark production the mass is dominated by the top-quark transverse momenta.

The ratio of the transverse momenta of either W boson to its associated top quark is measured to probe the kinematic correlations in the top-quark decay process.

Fig. 13.5 shows this distribution for the leading top quark.

All MC predictions show poor agreement with data for this observable, with p -values at or below the 10% level (Tab. 13.1). The data indicate a slightly higher proportion of events in the first and last bins where R_{Wt}^{leading} has a value close to 0 or 1.

Angular distributions

Given that in the all-hadronic channel the four-momenta of both top quarks are fully reconstructed, angular distributions are important observables to study in this channel.

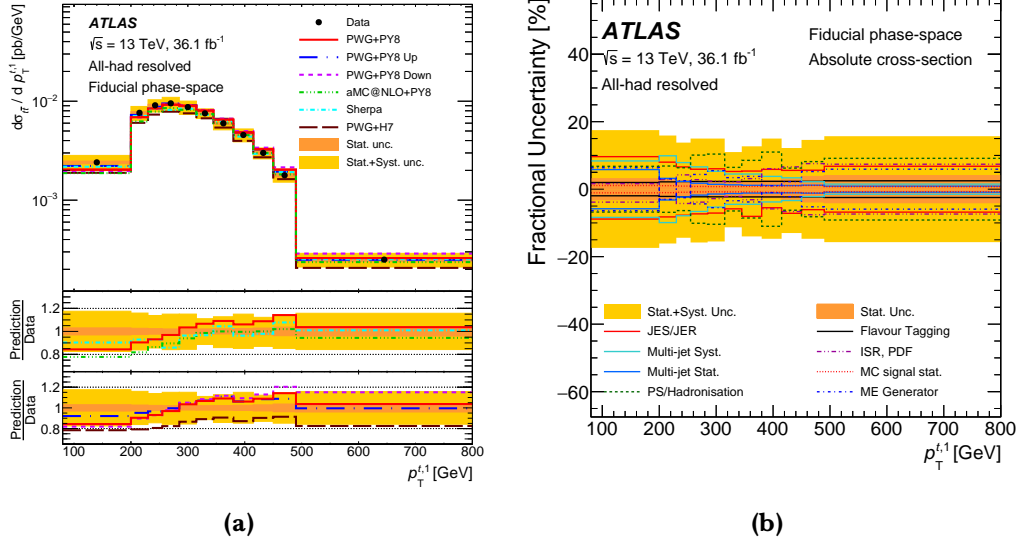


Figure 13.3: (a) Particle-level single-differential absolute cross-section measurement as a function of the leading top-quark transverse momentum. The unfolded data are compared with theoretical predictions. (b) Fractional uncertainties for the absolute single-differential cross-sections as a function of the leading top-quark transverse momentum.

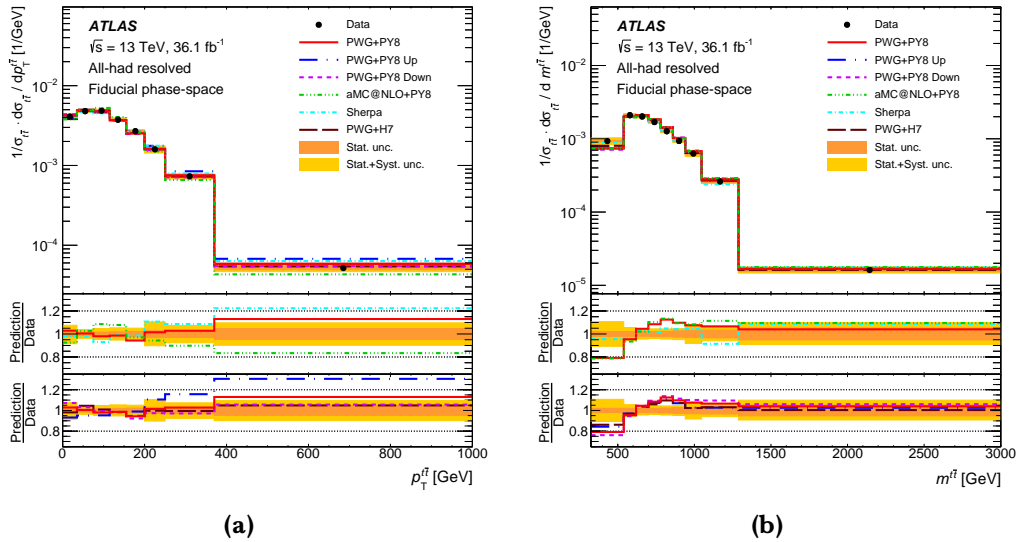


Figure 13.4: Particle-level normalised single-differential cross-sections as a function of (a) the transverse momentum of $t\bar{t}$ system and (b) of the $t\bar{t}$ system mass, compared with different MC predictions.

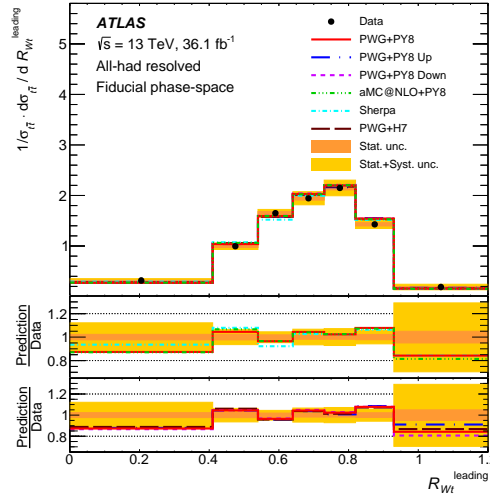


Figure 13.5: Particle-level normalised single-differential cross-section as a function of the ratio of W -boson p_T to parent top-quark p_T for the leading top quark, R_{Wt}^{leading} .

One of the angular observables is the azimuthal separation $\Delta\phi^{t\bar{t}}$ between the top quarks (Fig. 13.6), which is influenced by the $p_T^{t\bar{t}}$ distribution and may be sensitive to BSM couplings [80]. For the nominal POWHEG+PYTHIA8 configuration good agreement with data is observed, but deviations are observed for both POWHEG+PYTHIA8 variation samples and for MADGRAPH5_aMC@NLO+PYTHIA8.

Jet radiation characterisation

One of the chief goals of this measurement is to characterise the modelling of jet radiation accompanying $t\bar{t}$ production.

The signal purity is seen to be relatively good for $N_{\text{jets}} < 10$ (Fig. 10.5) and the background uncertainties in the normalised cross-section (Fig. 13.7b) are small compared with theoretical uncertainties. This indicates that this measurement is to properties of up to at least three emissions.

The unfolded jet multiplicity distribution is shown in Fig. 13.7.

Matrix element, ISR and parton shower/hadronisation uncertainties are dominant in most jet multiplicity bins, while jet energy scale and resolution uncertainties are large both for the seven-jet bin and for events with at least 10 jets.

The data indicate that more radiation is produced than predicted by the nominal POWHEG+PYTHIA8 configuration, while the Var3cUp variation and POWHEG+HERWIG7 are more consistent with the data. While SHERPA and MADGRAPH5_aMC@NLO+PYTHIA8 also reproduce the data fairly well, there is disagreement in the 7-jet bin which corresponds to events with a single hard

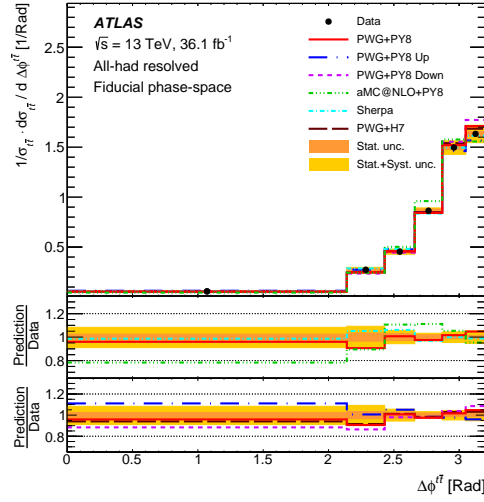


Figure 13.6: Particle-level normalised single-differential cross-sections as a function of the azimuthal separation $\Delta\phi^{t\bar{t}}$ between the two top-quark candidates.

emission.

Fig. 13.8 shows the differential cross-section as a function of the p_T ratio between the leading top-quark and one of the jets originating outside the $t\bar{t}$ decay.

The p_T of the first ISR emission and the leading top-quark p_T are important scales for the $t\bar{t}$ production process. Their ratio $R_{t,1}^{\text{extra1}}$ compares these two scales and shows a significant departure from the data for various generators. Furthermore, it can be noted that the leading extra jet's p_T spectrum has a most probable value at around a quarter of the leading top-quark p_T and exceeds the leading top-quark p_T at a low rate. The second emission p_T peaks slightly lower than the first. While reproduced better than the leading emission, all simulations produce too many events with $R_{t,1}^{\text{extra2}}$ close to 0.3 and too few elsewhere. The third emission p_T does not show significant deviations from the data.

Systematic uncertainties in the background estimation are dominant for the $R_{t,1}^{\text{extra1}}$ distribution but are substantially smaller than the observed deviation. The background uncertainty is comparable to the modelling uncertainties for $R_{t,1}^{\text{extra2}}$, but is also dominant for $R_{t,1}^{\text{extra3}}$.

Consistent with other observations, the nominal POWHEG+PYTHIA8 configuration produces a first emission that is too soft with respect to the data, as does MADGRAPH5_aMC@NLO+PYTHIA8.

In events with substantial ISR, the leading extra jet may provide the relevant scale for the process. The distribution of $R_{\text{extra1}}^{\text{extra2}}$ (Fig. 13.9) tests the second

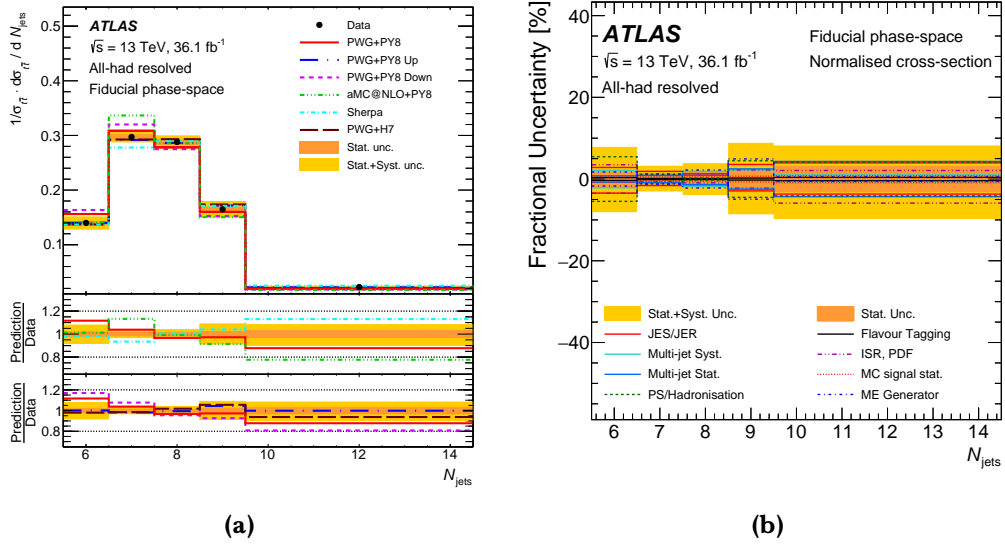


Figure 13.7: Normalised single-differential cross-section measurements at particle level as a function of (a) the jet multiplicity. (b) Fractional uncertainties for the normalised single-differential distributions unfolded at particle level as a function of the jet multiplicity.

emission modelling relative to the leading extra jet p_T . The sub-leading extra jet p_T is broadly peaked just below half the leading extra jet p_T with a skew towards higher values.

Fig. 13.10 shows the separation in ΔR between the first emission and the leading jet in the event, which may or may not originate from the decay of one of the top quarks.

A significant peak is observed at $\Delta R = 0$, demonstrating that in events with at least one extra jet the leading jet is most often from ISR rather than a top-quark decay product.

The distribution of ΔR for events in which the leading jet is associated with one of the top quarks has a tendency towards large values, close to π . In other words, in events where the leading jet is a decay product of one of the top quarks, the first hard emission tends to be emitted in a direction that balances the leading top-quark jet.

Significant mismodelling of this distribution is observed in SHERPA, MADGRAPH5_aMC@NLO+PYTHIA8 and POWHEG+HERWIG7, all of which over-estimate how frequently the leading jet is a decay product of one of the top quarks. For such events, the extra jet is also typically emitted too close to the leading top-quark jet. The same trend is seen to a lesser degree for the nominal POWHEG+PYTHIA8 configuration, whereas the Var3cUp variation reproduces the data well.

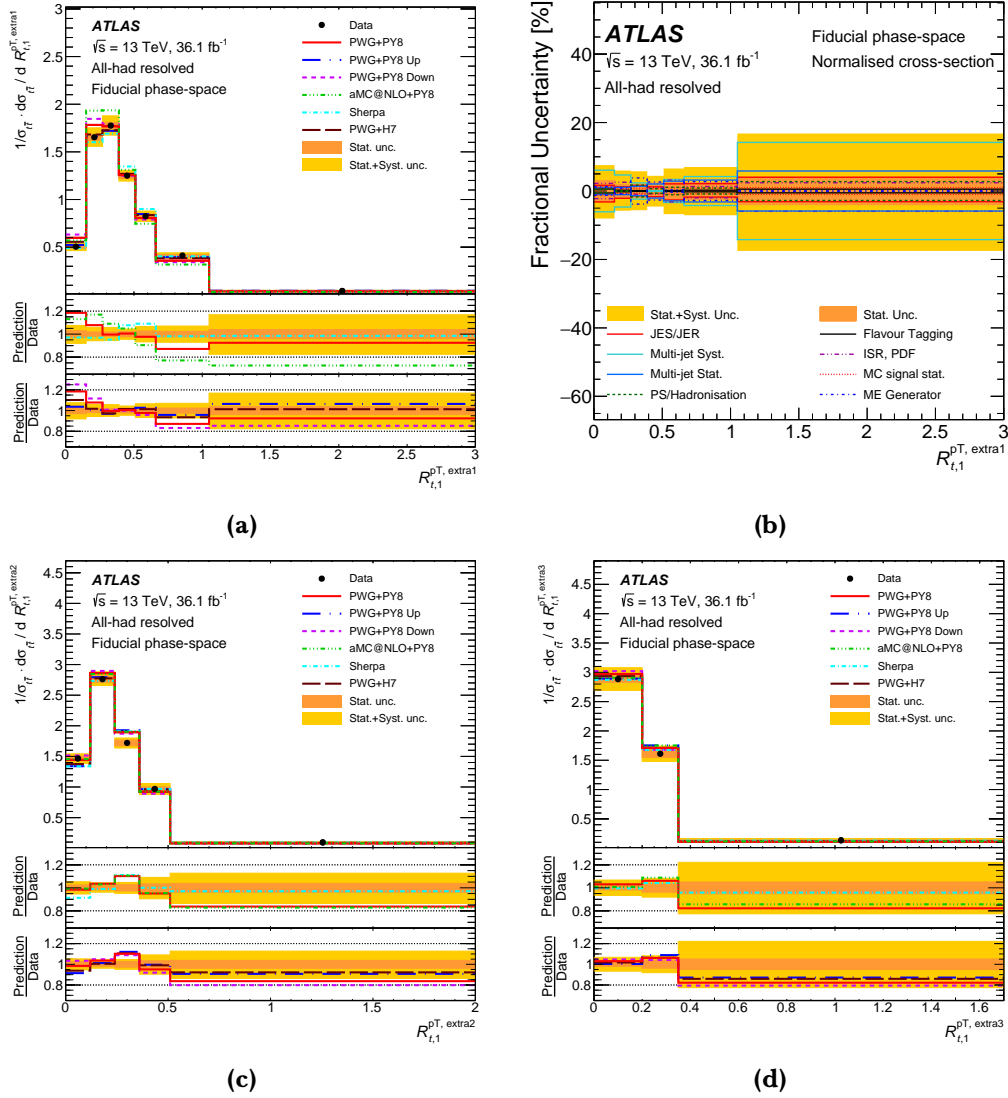


Figure 13.8: Normalised particle-level single-differential cross-sections as a function of the ratio of the (a) leading, (c) sub-leading and (d) sub-subleading extra jet p_T to the leading top-quark p_T . (b) Normalised fractional uncertainties for the single-differential cross-sections as a function of the ratio of leading extra jet p_T with respect to the leading top-quark p_T .

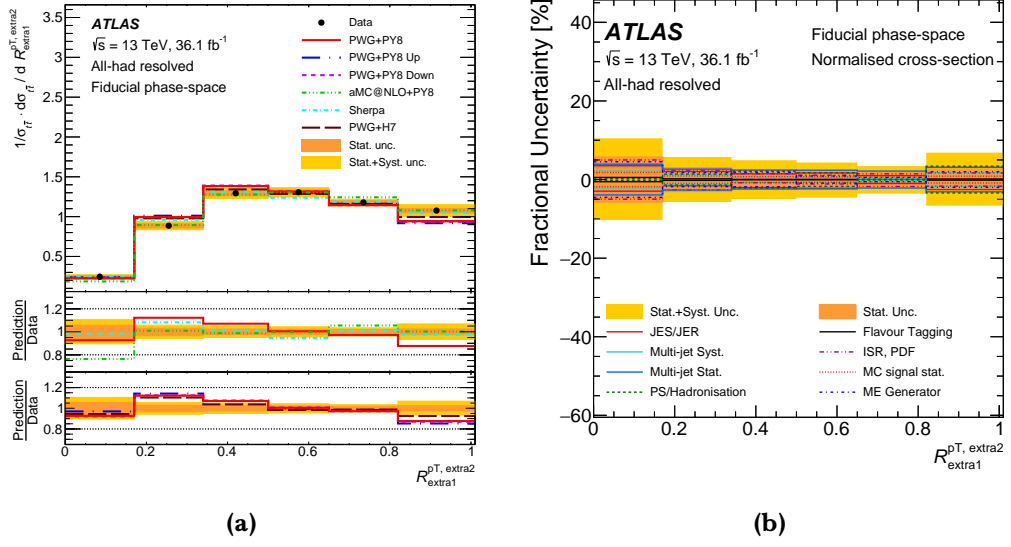


Figure 13.9: Normalised single-differential normalised cross-sections at the particle-level as a function of (a) the ratio of sub-leading extra jet p_T to the leading extra jet p_T . Normalised fractional uncertainties for the single-differential cross-sections as a function of (b) the ratio of sub-leading extra jet p_T with respect to the leading extra jet p_T .

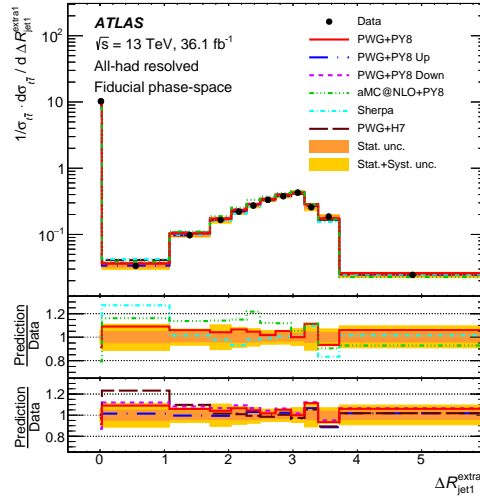


Figure 13.10: Normalised particle-level single-differential cross-section as a function of the angular separation ΔR between the leading jet and the leading extra jet.

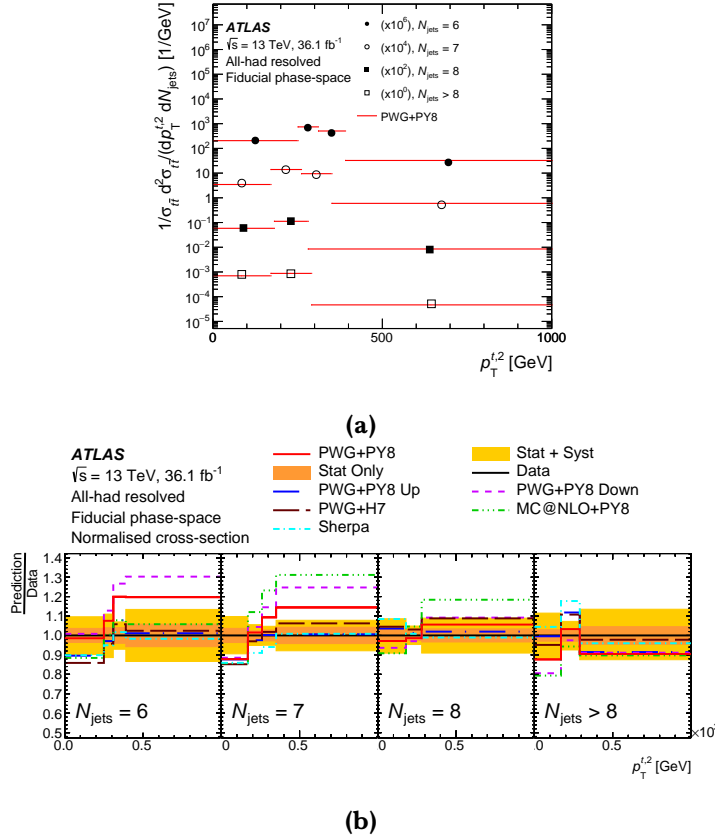


Figure 13.11: Normalised particle-level double-differential cross-section as a function of (a) the sub-leading top-quark transverse momentum $p_T^{t,2}$ in bins of the jet multiplicity N_{jets} , compared with the nominal POWHEG+PYTHIA8 prediction without uncertainties with data points placed at the centre of each bin. $p_T^{t,2}$ is shown on the horizontal axis and different markers are used to distinguish the four bins in N_{jets} . (b) Ratio of the measured cross-section to different MC predictions.

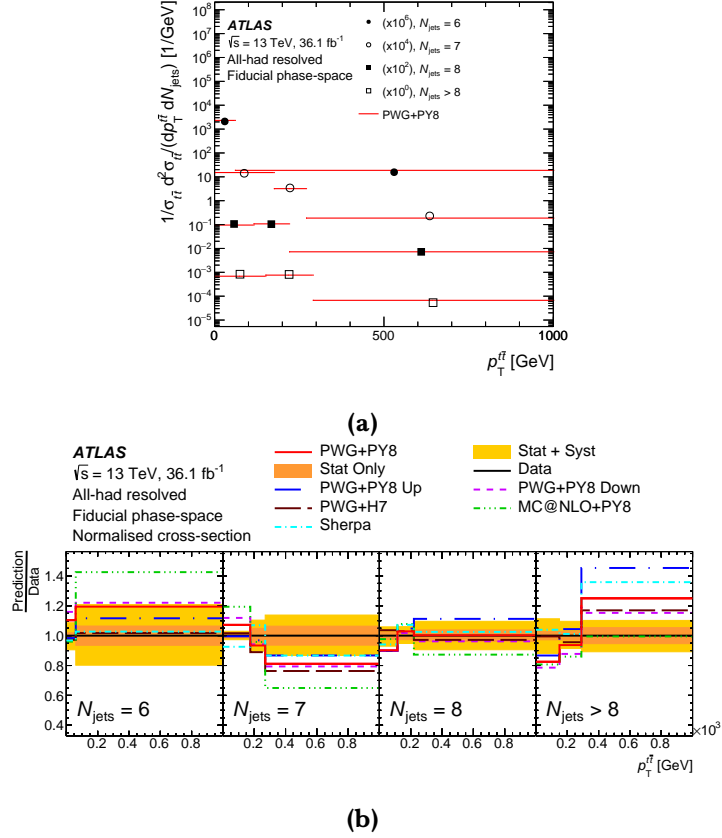


Figure 13.12: Normalised particle-level double-differential cross-section as a function of (a) the $t\bar{t}$ system transverse momentum $p_T^{t\bar{t}}$ in bins of the jet multiplicity N_{jets} , compared with the nominal POWHEG+PYTHIA8 prediction without uncertainties with the data points placed at the centre of each bin. $p_T^{t\bar{t}}$ is shown on the horizontal axis and different markers are used to distinguish the four bins in N_{jets} . (b) Ratio of the measured cross-section to different MC predictions.

Normalised double-differential cross-sections as a function of the sub-leading top-quark p_T and the p_T of the $t\bar{t}$ system in bins of jet multiplicity are shown in Fig. 13.11 and Fig. 13.12, respectively.

For low jet multiplicities, which are relatively pure in signal, the dominant uncertainties are from jet energy scales, PDFs and the modelling of the $t\bar{t}$ radiation. Since the parton shower modelling becomes particularly important at larger jet multiplicities, the corresponding uncertainty grows to be the most significant for both observables.

In both observables, the six- and seven-jet bins show the clearest signs of mis-modelling.

Analogously to what was observed in the single-differential measurement, for the sub-leading top-quark p_T , the MC predictions show the tendency of being too hard. For the $t\bar{t}$ transverse momentum, on the other hand, different trends are seen, where the predictions are typically too soft in the seven-jet bin, where a single hard emission is produced, but too hard in the other bins.

Fig. 13.13 shows the normalised double-differential cross-section as a function of the $t\bar{t}$ azimuthal separation $\Delta\phi^{t\bar{t}}$ and the jet multiplicity.

Contrarily to what was observed for the corresponding single-differential distribution (Fig. 13.6), which shows mostly good agreement between data and simulation, the decomposition of the distribution into different jet multiplicity bins can be seen to be poorly modelled by all event generators.

The common trend is that in the seven-jet bin, the data indicates that the top-quark pair should be more back-to-back, while for events with at least two additional emissions the top-quark pair should be less separated. This observation correlates with the results seen in the double-differential measurement of $p_T^{t\bar{t}}$ versus N_{jets} (Fig. 13.12). There, events where the two top quarks are more back-to-back result in a system with a smaller $p_T^{t\bar{t}}$, as observed in the distribution in the seven-jet bin, while in the case of smaller angular distance, the $p_T^{t\bar{t}}$ turns out to be higher as observed in the distribution of the last N_{jets} bin of Fig. 13.12.

13.3 Results at parton level

At parton level, the normalised single-differential cross-section unfolded to the full phase space as a function of the transverse momentum of the leading top quark is presented in Fig. 13.14.

The corresponding absolute differential cross-section is shown in Fig. 13.15 for comparison.

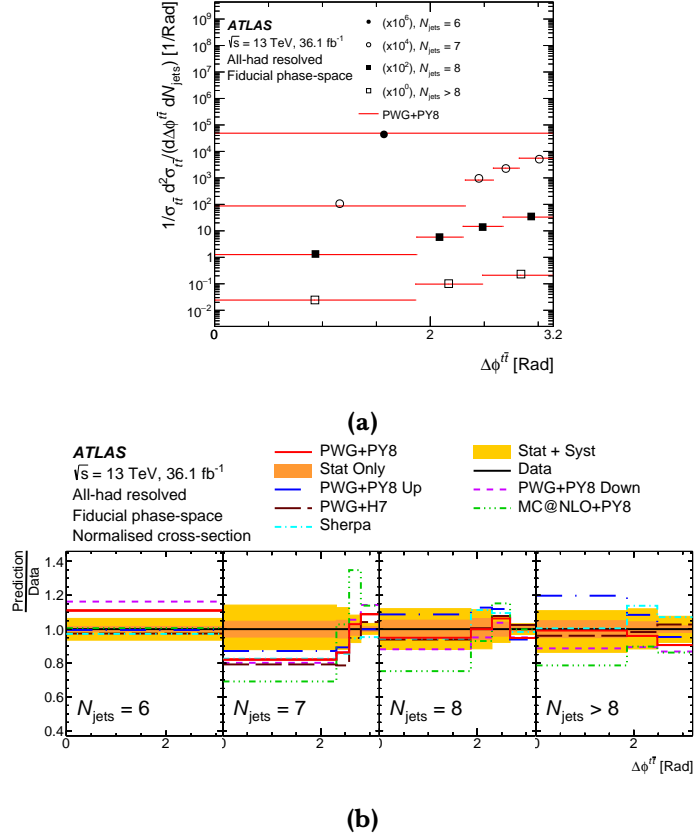


Figure 13.13: Particle-level double-differential normalised cross-section (a) as a function of the azimuthal separation $\Delta\phi^{t\bar{t}}$ between the top quark and the antitop quark in bins of the jet multiplicity N_{jets} , compared with the nominal POWHEG+PYTHIA8 prediction without uncertainties. Data points are placed at the centre of each bin. Different markers are used to distinguish the four bins in N_{jets} , while $\Delta\phi^{t\bar{t}}$ is shown on the horizontal axis. The ratio (b) of the measured cross-section to different MC predictions.

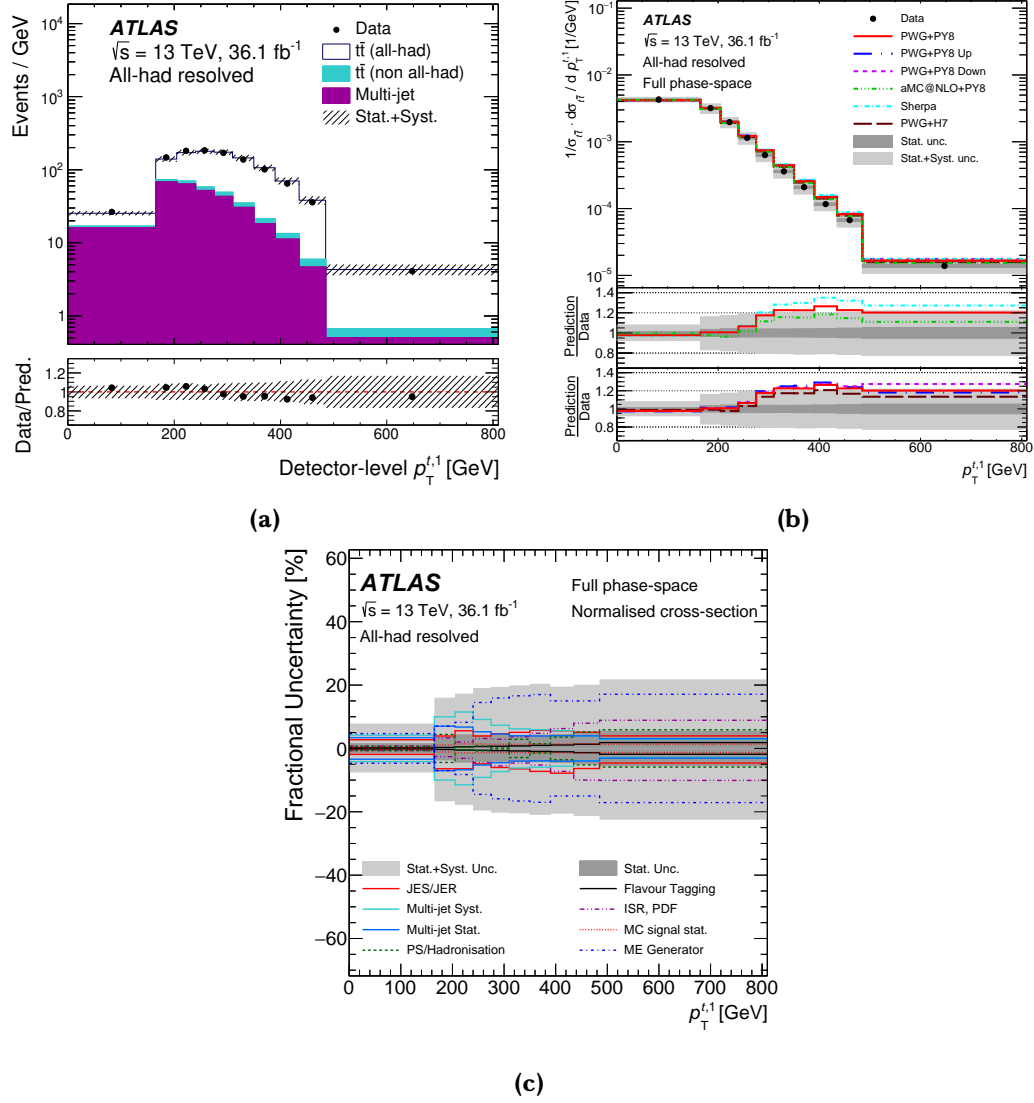


Figure 13.14: Comparison of data with the fully simulated nominal theoretical predictions for (a) the leading top-quark transverse momentum. Normalised single-differential cross-section measurement at parton level as a function of (b) the leading top-quark transverse momentum. Normalised fractional uncertainties for the single-differential distributions at parton level as a function of (c) the leading top-quark transverse momentum. Overflow events are included in the last bin.

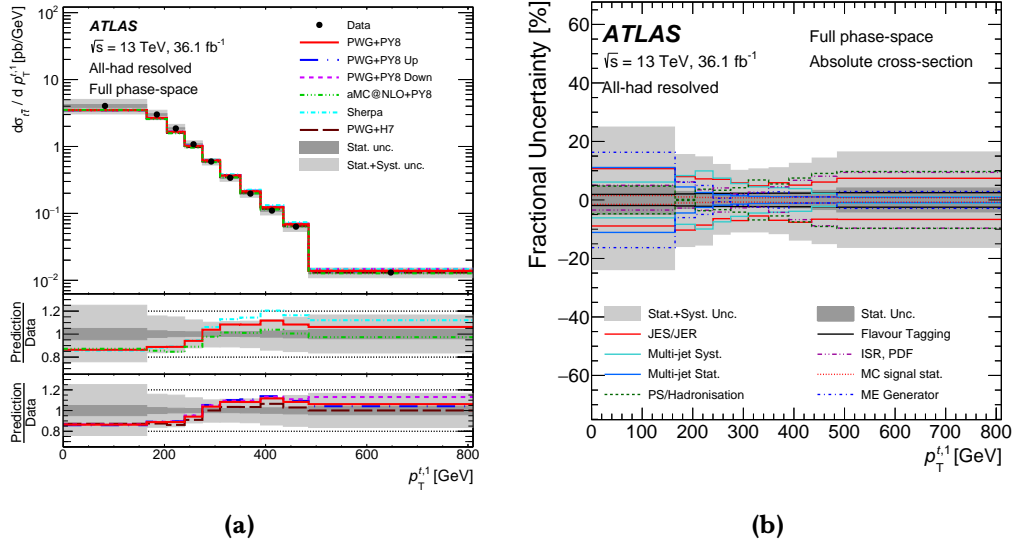


Figure 13.15: Absolute single-differential cross-section measurements at the parton level as a function of (a) the leading top-quark transverse momentum. The data unfolded are compared with the theoretical predictions. Absolute fractional uncertainties for the single-differential distributions unfolded at parton level as a function of (b) the leading top-quark transverse momentum.

The normalised measurement is once more characterised by significant cancellations in the uncertainties (primarily b -tagging and parton shower). However, the normalisation procedure inflates the hard-scatter uncertainty at large p_T , due to the normalisation being influenced mostly by bins at low transverse momentum for which the absolute differential cross-section is affected by a large hard-scatter uncertainty. Even so, the trends are similar to those observed in the particle-level measurements, with the data being best described by POWHEG+HERWIG7.

Two absolute double-differential cross-section measurements are shown at parton level: the dependence of the leading top-quark transverse momentum on the top-quark pair mass in Fig. 13.16 and the dependence of the leading top-quark rapidity on the top-quark pair mass in Fig. 13.17.

The main trend that is observed in former distributions is, once more, that the event generators predict a harder leading top-quark p_T than it is seen in the data. This feature appears in all $m^{t\bar{t}}$ bins. By contrast, the rapidity is fairly well modelled in all bins.

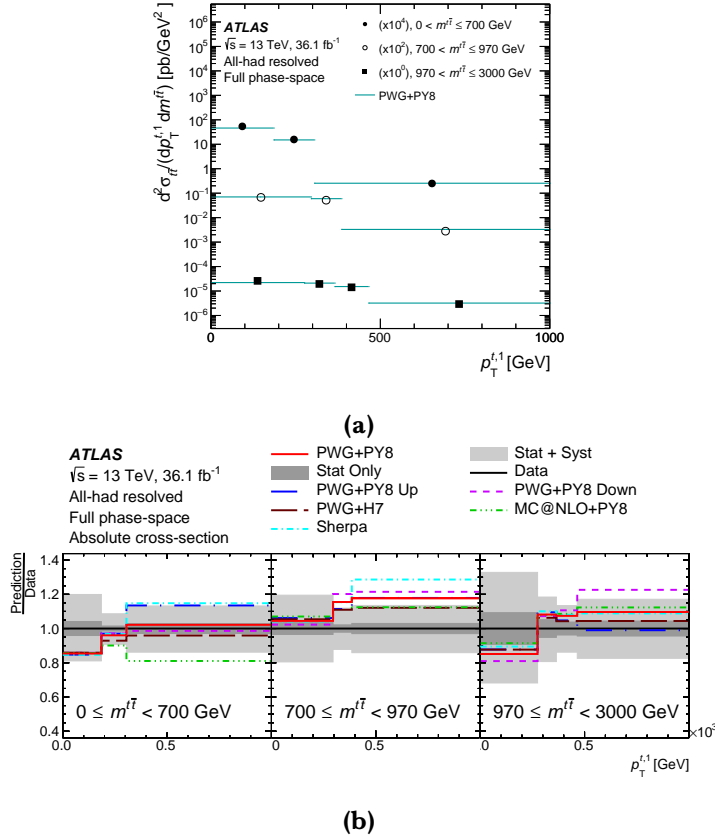


Figure 13.16: Absolute double-differential absolute cross-section at the parton-level as a function of (a) the leading top-quark transverse momentum in bins of the $t\bar{t}$ system mass, compared with the nominal POWHEG+PYTHIA8 prediction without uncertainties with the data points placed at the centre of each bin. $p_T^{t,1}$ is shown on the horizontal axis and different markers are used to distinguish the three bins in $m^{t\bar{t}}$. (b) Ratio of the measured cross-section with respect to the different MC predictions.

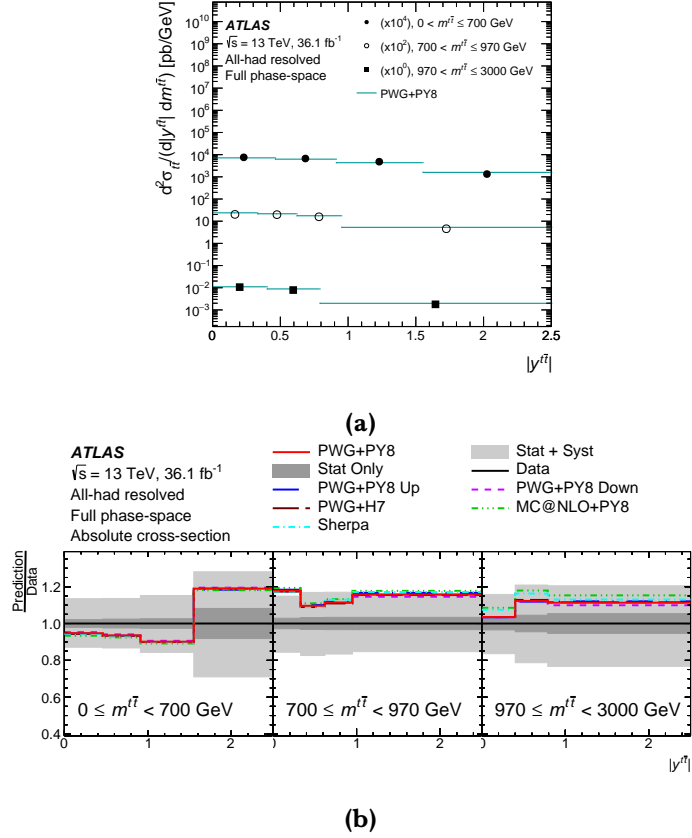


Figure 13.17: Absolute double-differential cross-section at the parton-level as a function of (a) the $t\bar{t}$ system rapidity in bins of the $t\bar{t}$ system mass, compared with the nominal POWHEG+PYTHIA8 prediction without uncertainties with the data points placed at the centre of the bin. $y^{t\bar{t}}$ is shown on the horizontal axis and different markers distinguish between the three bins in $m^{t\bar{t}}$. (b) Ratio of the measured cross-section with respect to different MC predictions.

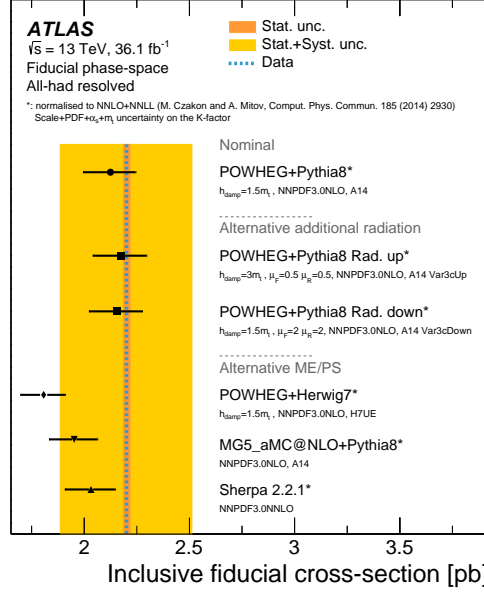


Figure 13.18: Comparison of the measured inclusive fiducial cross-section with the predictions from several MC generators. The yellow band represents the total uncertainty in the data. The orange band represents the statistical uncertainty only. The uncertainty in the cross-section predicted by each NLO MC generator only includes the uncertainty (due to scales, PDFs, m_t and α_s) affecting the K -factor used in the normalisation.

13.4 Total cross-section

The total cross-section obtained in the fiducial phase space is

$$\sigma_{t\bar{t}} = 2.20 \pm 0.31(\text{stat.} + \text{syst.})\text{pb},$$

where the total uncertainty is 14% and the statistical uncertainty is 0.5%. This value is compatible with the MC predictions shown in Fig. 13.18 and in Tab. 13.2. The total cross-section predicted by each NLO MC generator is normalised to the NNLO+NNLL prediction quoted in Ref. [81].

Accounting for all decay modes, the total cross-section in the full phase space corresponds to

$$\sigma_{t\bar{t}} = 864 \pm 127(\text{stat.} + \text{syst.}) \text{ pb},$$

where the total uncertainty is 15% and the statistical uncertainty is 0.5%. This cross-section is compatible with a value of $\sigma_{t\bar{t}} = 832^{+20}_{-29}(\text{scale}) \pm 35(\text{PDF}, \alpha_s) \text{ pb}$ as calculated by the Top++2.0 program at NNLO in perturbative QCD. This value includes soft-gluon resummation to NNLL [81, 82, 83, 84, 85, 86] and assumes a top mass of 172.5 GeV.

Sample	Fiducial cross-section [pb]
PWG+Py8	$2.13^{+0.13}_{-0.12}$
PWG+Py8 Rad. Up	$2.17^{+0.13}_{-0.12}$
PWG+Py8 Rad. Down	$2.15^{+0.13}_{-0.12}$
PWG+H7	$1.81^{+0.11}_{-0.10}$
MADGRAPH5_aMC@NLO	$1.95^{+0.12}_{-0.11}$
SHERPA 2.2.1	$2.03^{+0.12}_{-0.11}$
Data	$2.20 \pm 0.31(\text{stat.} + \text{syst.})$

Table 13.2: Comparison between the measured inclusive fiducial cross-section and the predictions from several MC generators. The uncertainty in the cross-section as predicted by each NLO MC generator only includes the uncertainty which affect the K -factor used in the normalisation: PDFs, m_t and α_s .

Comparison with other ATLAS differential cross-section measurements

In this chapter, a selection of the results obtained is compared with similar measurement of differential cross-sections in other $t\bar{t}$ decay channels.

14.1 Comparison of results with the ℓ +jets channel

Many of the observables measured in this analysis were also measured in the analysis of the ℓ +jets final state for the top-quark pair production [87]. And although the two analysis have several differences in their approaches, they share enough commonalities to allow for a result comparison.

Noticeably, the object selection is significantly different. The object selection usually driven by the trigger, which for this analysis is based on a trigger selection of at least six jets with a p_T greater than 55 GeV, while in the ℓ +jets analysis the trigger selection requires a lepton with $p_T > 20$ GeV and all jets with a p_T of at least 25 GeV.

Therefore, on one side, the extrapolation to the full phase space used for the parton-level results is therefore bigger for the all-hadronic channel and the size of the available data sample is smaller, while on the other side, the all-hadronic channel allows for full event reconstruction from well-measured objects. This in turn leads to better resolution for the observables and allows for the measurement of particular angular and extra jets observables relative to the $t\bar{t}$ system.

	Analysis	$p_T^{t\bar{t}}$		$H_T^{t\bar{t}}$	
		χ^2/dof	$p\text{-value}$	χ^2/dof	$p\text{-value}$
PWG+PY8	all-had	4.8/8	0.78	23.4/11	0.02
	ℓ +jets	22.1/11	0.02	11.1/18	0.89
PWG+PY8 Var. Up	all-had	39.7/8	<0.01	22.8/11	0.02
	ℓ +jets	196.0/11	<0.01	17.7/18	0.48
PWG+PY8 Var. Down	all-had	7.2/8	0.51	32.8/11	<0.01
	ℓ +jets	16.9/11	0.11	10.5/18	0.91
SHERPA	all-had	15.7/8	0.05	13.7/11	0.25
	ℓ +jets	88.0/11	<0.01	11.9/18	0.85
PWG+H7	all-had	5.0/8	0.75	8.2/11	0.69
	ℓ +jets	33.4/11	<0.01	11.4/18	0.88

Table 14.1: Selection of measured particle-level absolute single-differential cross-sections for all-hadronic and ℓ +jets analyses for predictions from several MC generators. For each prediction, a χ^2 and a p -value are calculated using the covariance matrix of the measured spectrum. The number of degrees of freedom (dof) is equal to the number of bins in the distribution.

A summary of values with result from both analyses is shown in Tab. 14.1 for an easier comparison.

The particle-level results of both analyses are generally compatible in terms of the level of agreement observed between data and predictions, with some differences identified where variables are better described in either the ℓ +jets channel or the all-hadronic channel.

Consistent mismodelling is observed in both analyses for the $p_T^{t\bar{t}}$ distribution. The $H_T^{t\bar{t}}$ distribution, which is strongly correlated with the top-quark p_T distributions, is poorly modelled by all the MC predictions in the all-hadronic channel, while in the ℓ +jets channel, good agreement is observed between data and all the MC predictions.

A summary of the results at parton level from the two analyses is presented in Tab. 14.2.

At parton level, the $p_T^{t\bar{t}}$ distribution is poorly described by most of the MC predictions in both the ℓ +jets and all-hadronic channels. Unlike at particle-level, good agreement between data and all the MC predictions is observed in both channels for the $H_T^{t\bar{t}}$ variable. This is due to larger uncertainties, a consequence

	Analysis	$p_T^{t\bar{t}}$		$H_T^{t\bar{t}}$	
		χ^2/dof	$p\text{-value}$	χ^2/dof	$p\text{-value}$
PWG+PY8	all-had	1.5/5	0.91	13.6/11	0.26
	ℓ +jets	8.6/9	0.47	9.9/9	0.36
PWG+PY8 Var. Up	all-had	12.6/5	0.03	11.0/11	0.44
	ℓ +jets	42.4/9	<0.01	10.1/9	0.34
PWG+PY8 Var. Down	all-had	2.2/5	0.83	20.0/11	0.05
	ℓ +jets	24.3/9	<0.01	9.9/9	0.36
SHERPA	all-had	9.6/5	0.09	16.7/11	0.12
	ℓ +jets	20.6/9	0.01	19.6/9	0.02
PWG+H7	all-had	3.0/5	0.70	11.0/11	0.70
	ℓ +jets	14.1/9	0.12	6.7/9	0.67

Table 14.2: Selection of measured parton-level absolute single-differential cross-sections for all-hadronic and single lepton analyses for predictions from several MC generators. For each prediction, a χ^2 and a p -value are calculated using the covariance matrix of the measured spectrum. The number of degrees of freedom (dof) is equal to the number of bins in the distribution.

of the extrapolation from the small fiducial region to the full phase space.

When considering the double-differential results at both particle and parton levels, both analyses show that none of the predictions can describe any of the measured distributions.

Fig. 14.1 shows a comparison between the measured absolute differential cross-sections in the ℓ +jets and all-hadronic channels, at parton level, for $H_T^{t\bar{t}}$ and the average top transverse momentum p_T^t . The average top transverse momentum is determined by randomly picking one of the two top candidates in each event.

The two measurements are qualitatively consistent in the overlap region.

For $H_T^{t\bar{t}} \gtrsim 325 \text{ GeV}$ and $p_T^t \gtrsim 130 \text{ GeV}$, where neither statistics nor signal purity are limiting, the all-hadronic measurement achieves a better resolution than the ℓ +jets channel.

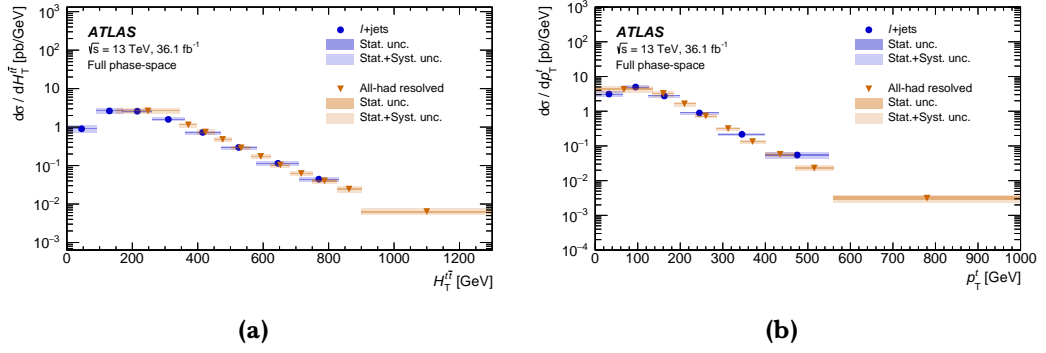


Figure 14.1: Comparison between the measured absolute single-differential cross-sections in the ℓ +jets and all-hadronic channels as functions of (a) $H_T^{l\bar{l}}$ and (b) the average top quark transverse momentum p_T^t .

14.2 Comparison of results with the all-hadronic channel in the boosted topology

Measurements of differential cross-sections in the all-hadronic channel have been performed in the boosted topology [88], motivating a comparison with the results of this analysis.

The all-hadronic resolved parton-level measurements are unfolded to the full phase space, while the measurements in the boosted topology are unfolded to a fiducial phase space, so a direct comparison of the differential measurements is not possible. The ratios of the measured absolute differential cross-sections are therefore compared.

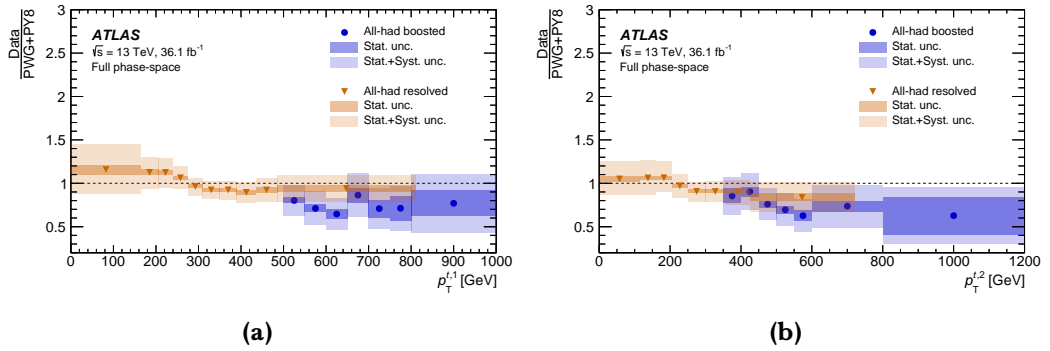


Figure 14.2: The ratios of the measured absolute differential cross-sections at parton level to the predictions obtained with the POWHEG+PYTHIA8 MC generator in the all-hadronic resolved and boosted topologies as a function of the (a) leading and (b) subleading top-quark candidate p_T .

Fig. 14.2 shows the ratios of the measured absolute differential cross-sections at parton level to the predictions obtained with the POWHEG+PYTHIA8 MC

generator in the all-hadronic resolved and the boosted topologies as a function of the $p_T^{t,1}$ and $p_T^{t,2}$ variables.

The ratios between the data and the signal MC generator are qualitatively consistent between the two topologies in the overlap region.

Deep neural network for $t\bar{t}$ system reconstruction

In this chapter, future prospects on the use of machine learning techniques for $t\bar{t}$ system reconstruction are presented. For this purpose, a deep neural-network architecture based on the pytorch library [89] has been developed. The code base, currently packaged under the name ALPACA, is being used also by other ATLAS analysis teams in searches for new physics where the final state has similar characteristics.

Connecting the reconstructed jets with their parent top quark of origin was one of the difficulties in the presented analysis, as the factorial dependence on the number of jets leads to an elevated number of combinatorics to be evaluated. As part of the χ^2 -minimisation method, a χ^2 value had to be computed for all possible permutations of jets in the event.

Future prospects concern the application of novel machine learning algorithms based on neural-network architectures for the classification of hadronic objects. Solving the computational problem of high combinatorics would avoid the factorial dependence burden of building the many jets permutations.

Other than improving on the current method of top reconstruction, such efforts have a direct applications to BSM searches characterised by a large multi-jet background.

The presented approach for the investigation of the jet substructure combines machine learning techniques with elements of special relativity. Specifically, the Lorentz group and the Minkowski metric are introduced as part of the neural-network architecture to distinguish signal from background.

15.1 Architecture

The top-tagger presented consists of a *combination layer* (CoLa) is combined with a physics-inspired layer called *lorentz layer* (LoLa) and with two fully connected layers forming a *deep neural network* (DNN) architecture [90].

The neural network entry for each event consists of a matrix of jets 4-momenta:

$$k_{\mu,i} = \begin{pmatrix} k_{0,1} & k_{0,2} & \dots & k_{0,N} \\ k_{1,1} & k_{1,2} & \dots & k_{1,N} \\ k_{2,1} & k_{2,2} & \dots & k_{2,N} \\ k_{3,1} & k_{3,2} & \dots & k_{3,N} \end{pmatrix}, \quad (15.1)$$

where μ is the Lorentz index, while the index i spans over the jets in the event.

15.1.1 Combination layer

The combination layer provides multi-jet recombination by returning M combined 4-vectors

$$\tilde{k}_{\mu,j} = k_{\mu,i} C_{ij}, \quad (15.2)$$

where $k_{\mu,i}$ is the input set of jets 4-vectors momenta and C_{ij} is the combination layer transformation matrix defined as follows:

$$C = \left(I_N \mid W_{N \times M} \right) = \begin{pmatrix} 1 & 0 & \dots & 0 & W_{1,1} & \dots & W_{1,M} \\ 0 & 1 & & \vdots & W_{2,1} & \dots & W_{2,M} \\ \vdots & \vdots & \ddots & 0 & \vdots & & \vdots \\ 0 & 0 & 0 & 1 & W_{N,1} & \dots & W_{N,M} \end{pmatrix}, \quad (15.3)$$

where I_N is the identity matrix $N \times N$ and the W submatrix $N \times M$ represents the trainable set of $M - N$ linear combinations weights.

15.1.2 Lorentz Layer

The Minkowski metric is used to construct a weight function, transforming the constituent 4-vectors to quantities more directly related to physical observables.

The Lorentz layer maps the jet 4-vector into five entries, which illustrate different structures included in this Lorentz layer. The first two are the invariant

mass and the transverse momentum. The third entry constructs a linear combination of all energies, with a trainable vector of weights $w_{jl}^{(E)}$.

$$\hat{k}_{i,j} = \begin{pmatrix} m^2(\tilde{k}_{\mu,j}) \\ p_T(\tilde{k}_{\mu,j}) \\ w_{jl}^{(E)} E(\tilde{k}_{\mu,l}) \\ w_{jl}^{(d)} d_{jl}^2 \\ w_{jl}^{(p_z)} p_z \end{pmatrix}, \quad (15.4)$$

where $w_{jl}^{(E)}$, $w_{jl}^{(d)}$ and $w_{jl}^{(p_z)}$ represent trainable vectors of weights; d_{jl}^2 is the Minkowski distance between two four-momenta $\tilde{k}_{\mu,i}$ and $\tilde{k}_{\mu,l}$ defined as

$$(\tilde{k}_{\mu,i} - \tilde{k}_{\mu,l})g^{\mu\nu}(\tilde{k}_{\nu,i} - \tilde{k}_{\nu,l}). \quad (15.5)$$

The role of the Lorentz layer can be considered as a transformation in the observable space, making the relevant information more accessible to the neural network layer that follows it.

15.2 Jet assignment

Each jet has a label based on ΔR matching to the truth partons from the top decay. These values represent the aim topology that the neural network has to understand and reconstruct from the event kinematics.

The label values are reported in Tab. 15.1. Although, it is not expected from the network to be able to distinguish the charges of the top quarks, or those of the W -boson decay products.

The loss functions used are built around sigmoid output nodes for binary classification. The multi-class tagging is handled by outputting a discriminant for each possible class, such that the highest score identifies the most likely label.

The model is trained to reproduce a series of binary labels that encode the jet identities. The decay structure has been encoded in three separate multi-binary forms.

The first form encodes the ISR information. A value of 1 is assigned to jets that are associated with the top-quarks decay, and a value of 0 is assigned otherwise. This discriminant is redundant for training in the six-jets region where all six jets are a result of the top-quarks decay.

Label	Description
0	jet not associated with any of the top-quarks decay products
1	b -jet associated with the top-quark decay
2	light jet associated with the top-quark decay
3	light jet associated with the top-quark decay
4	b -jet associated with the antitop-quark decay
5	light jet associated with the antitop-quark decay
6	light jet associated with the antitop-quark decay

Table 15.1: Training labels for the jets in an event based on ΔR matching to the truth partons from the top decay.

The second form aims to correctly assign the six jets associated with the top-quarks decay to the two triplets corresponding to the two top quarks. To achieve this goal, the two jets that belong to the same triplet of the leading top-jet are assigned a value of 1, while the jets that belong to the other triplet are assigned a value of 0. The leading jet in the two triplets and the jets that do not belong to any triplet are not labeled.

The third form encodes the b -tagging information aiming to use the kinematics information to tell apart the b -jets from the light jets produced by the W -bosons decay. A value of 1 is assigned if the jet is a b -tagged jet and a value of 0 is assigned otherwise.

A concrete example for an event with ten jets is shown in Tab. 15.2. The parton labels represent the truth matched information for each jet in the event. Since in this case the jet in the second position is considered to be the leading jet from a top decay, its triplet label is missing. The other two out of the remaining five top-jets that belong to the same leading top-jet triplet have a triplet label equal to 1.

The training is performed using cross-entropy between the output probabilities and the target labels.

The $t\bar{t}$ system is reconstructed according to the selection of the six jets with the highest top-jet score. Then, of those six, the leading top jet with the two other jets scoring highest in the top decay labels are grouped together. Finally, the two highest scoring jets with the b -tag label are considered as best b -jets candidates.

Parton labels	0	3	4	1	5	0	2	6	0	0
Top-jet labels	0	1	1	1	1	0	1	1	0	0
Triplet labels			0	1	0		1	0		
b -jet labels		0	1	1	0		0	0		

Table 15.2: A real-case example of label encoding for an event with ten jets. The parton labels are encoded into the three different binary formats for top-jet, triplets and b -jet labels.

15.3 Performance

The nominal POWHEG+PYTHIA8 sample is used to evaluate the top-tagger performance. The jets in each event are matched to true parton information with a $\Delta R < 0.2$. All six quarks are required to be unambiguously matched and to be among the first nine leading jets, as only the first nine jets in the event are fed into the neural network. These requirements leave 297 003 events, half of which are used for training and half for validation.

The *receiver operating characteristic* (ROC) curves are generic graphical illustrations of the diagnostic capability of a binary classifier as its discriminant threshold is varied. Such curves are created by plotting *false positive rate* (FPR) as a function of the *true positive rate* (TPR). Specifically, the FPR and TPR are defined as

$$FPR = \frac{FP}{FP + TN} \quad \text{and} \quad TPR = \frac{TP}{TP + FN}, \quad (15.6)$$

where FP are the false positives, FN are the false negatives, TP are the true positives and TN are the true negatives.

Fig. 15.1 shows the ROC curves for the three binary classifiers defined above. The areas under the curves have also been calculated and reported.

The top-jet discriminator for the first three leading jets in the event shows good performances with an *area under the curve* (AUC) of more than 80%. The leading jet has an AUC of almost 90%, while a slight lowering of about 5% is shown for the sub- and 3rd-leading jet with respect to the leading jet.

The b -jet discriminator for the first three leading top-jets candidates with AUCs just above 50% show almost no capacity from the network to distinguish between b -jets from light jets, based on kinematics information alone. This result is consistent with the fact that b -tagging algorithms, which rely on the b -quark distinct travel distance before decay, are indeed relevant for b -jet identification.

The triplet-matching discriminator also shows good performance with AUCs of

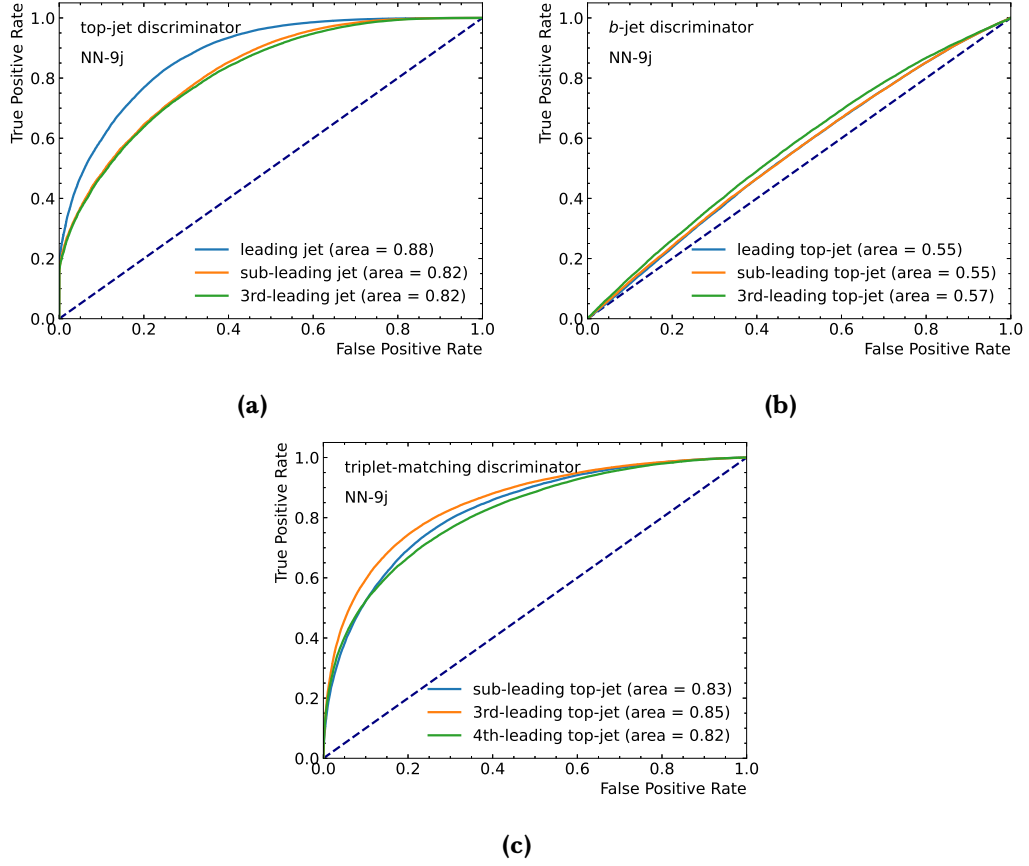


Figure 15.1: ROC curves for the (a) top-jet, (b) b -jet and (c) triplet-matching binary classifiers. In legenda, the area under the curves are specified.

about 80–85%. Although the trend for all top-jets is similar, a slight advantage is observed for the 3rd-leading top-jet.

15.3.1 Comparison with the chi-square method

In Fig. 15.2a are compared distributions of the leading top-quark candidate mass, reconstructed using the assignments generated by the DNN top-tagger and the χ^2 -minimisation method. The NN predictions are compared with and without an applied threshold on the top-jet discriminant score of the leading jet.

The chosen threshold value of 0.7 has been extracted from the comparison of score distributions for leading jets which correspond to jets generated from the products of the top-quarks decay against those which do not, as shown in Fig. 15.2b.

Together with a drastic reduction of the computational load, the NN prediction shows a favourable mass resolution distribution compared to the χ^2 . Further

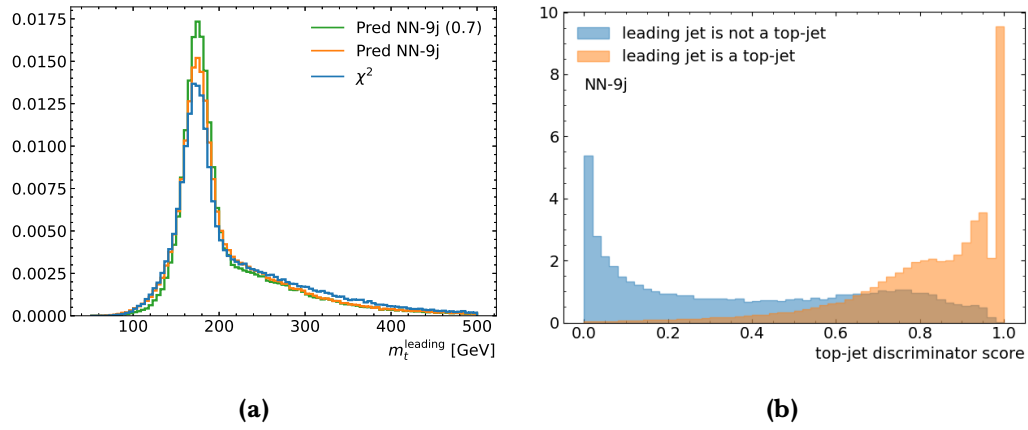


Figure 15.2: (a) Normalised distribution of the leading top-quark candidate mass as reconstructed using the neural network compared to the χ^2 method. The NN prediction with a threshold of 0.7 on the top-jet discriminant score is also compared. (b) Neural network top-jet discriminator score distribution for the leading jet in the event.

improvement on the mass resolution is observed for the NN prediction with an associated requirement on the top-jet discriminant of the leading jet in the event.

Conclusions

In this thesis have been presented single- and double-differential cross-section measurements for the production of top-quark pairs in the resolved topology of the all-hadronic channel. The data has been collected by the ATLAS detector at the CERN LHC from pp collisions at 13 TeV during 2015 and 2016, and it corresponds to an integrated luminosity of 36.1 fb^{-1} .

Several kinematic variables have been unfolded at the particle and parton level. Variables meant to probe correlations between the kinematics of the top-quark pair and associated jet radiation have also been introduced.

The results presented show sensitivity to various aspects of the MC predictions that have been tested.

Several predictions present poor agreement with the data. These observations can be used to improve the top-quark MC modelling. In particular, the double-differential cross-sections at the particle level offer to be extremely useful for improving the MC predictions in regions of the phase space with many additional jets. These regions are of express interest for analyses of many rare processes.

Furthermore, the measurements at the parton level are compared with theoretical predictions obtained from NLO MC generators, which interface with parton shower and hadronisation models. These results offer themselves to be used in future PDF measurements and top-quark pole mass extraction.

The rapidities of the individual top quarks and of the top-quark pair are well modelled, while the leading top-quark transverse momentum and top-quark pair transverse momentum are found to be incompatible with several theoretical predictions. Furthermore, significant mismodelling is observed in the hardness of the additional jet emissions.

The comparison with other published results showed that the predictions are rather accurate and for the most part compatible in the different regions of phase space and for different channels. However, some tension remains and better models are indeed needed to reproduce the data for all observables in all channels.

Concerning the upgrade studies for the HTT prototype, the obtained estimate on the FPGA resources necessary to obtain the targeted computational goal are used to drive the choice of FPGA vendor and model for the project.

Concerning the future prospects for the application of machine learning algorithms for the reconstruction of the $t\bar{t}$ system, a *deep neural-network* (DNN) architectures has been developed with embedded elements of special relativity, showing favourable results when compared with a χ^2 -minimisation technique.

Bibliography

- [1] G. Aad et al. ‘Measurements of top-quark pair single- and double-differential cross-sections in the all-hadronic channel in pp collisions at $\sqrt{s} = 13$ TeV using the ATLAS detector’. In: *Journal of High Energy Physics* 2021.1 (Jan. 2021), p. 33. ISSN: 1029-8479. DOI: [10.1007/JHEP01\(2021\)033](https://doi.org/10.1007/JHEP01(2021)033). URL: [https://doi.org/10.1007/JHEP01\(2021\)033](https://doi.org/10.1007/JHEP01(2021)033).
- [2] Riccardo Poggi. ‘Design of the ATLAS phase-II hardware-based tracking processor’. In: *Nuclear Instruments and Methods in Physics Research Section A: Accelerators, Spectrometers, Detectors and Associated Equipment* 936 (2019). Frontier Detectors for Frontier Physics: 14th Pisa Meeting on Advanced Detectors, pp. 305–307. ISSN: 0168-9002. DOI: <https://doi.org/10.1016/j.nima.2018.11.055>. URL: <http://www.sciencedirect.com/science/article/pii/S0168900218316309>.
- [3] Riccardo Poggi. ‘Digital Signal Processing in FPGA for Particle Track Reconstruction at the HL-LHC ATLAS’. In: *8th International Conference on Modern Circuits and Systems Technologies*. 2019, pp. 1–4. DOI: [10.1109/MOCAST.2019.8741949](https://doi.org/10.1109/MOCAST.2019.8741949).
- [4] S. L. Glashow. ‘Partial Symmetries of Weak Interactions’. In: *Nucl. Phys.* 22 (1961), pp. 579–588. DOI: [10.1016/0029-5582\(61\)90469-2](https://doi.org/10.1016/0029-5582(61)90469-2).
- [5] Steven Weinberg. ‘A Model of Leptons’. In: *Phys. Rev. Lett.* 19 (21 Nov. 1967), pp. 1264–1266. DOI: [10.1103/PhysRevLett.19.1264](https://doi.org/10.1103/PhysRevLett.19.1264). URL: <http://link.aps.org/doi/10.1103/PhysRevLett.19.1264>.
- [6] Abdus Salam. ‘Gauge unification of fundamental forces’. In: *Rev. Mod. Phys.* 52 (3 July 1980), pp. 525–538. DOI: [10.1103/RevModPhys.52.525](https://doi.org/10.1103/RevModPhys.52.525). URL: <https://link.aps.org/doi/10.1103/RevModPhys.52.525>.
- [7] G. Aad et al. ‘Observation of a new particle in the search for the Standard Model Higgs boson with the ATLAS detector at the LHC’. In: *Physics Letters B* 716.1 (2012), pp. 1–29. ISSN: 0370-2693. DOI: <https://doi.org/10.1016/j.physletb.2012.08.020>. URL: <http://www.sciencedirect.com/science/article/pii/S037026931200857X>.
- [8] S. Chatrchyan, V. Khachatryan and A.M. Sirunyan and. ‘Observation of a new boson at a mass of 125 GeV with the CMS experiment at the LHC’. In: *Physics Letters B* 716.1 (2012), pp. 30–61. ISSN: 0370-2693. DOI:

- <https://doi.org/10.1016/j.physletb.2012.08.021>. URL: <http://www.sciencedirect.com/science/article/pii/S0370269312008581>.
- [9] G. Aad et al. ‘Measurements of Higgs boson production and couplings in the four-lepton channel in pp collisions at center-of-mass energies of 7 and 8 TeV with the ATLAS detector’. In: *Phys. Rev. D* 91 (1 Jan. 2015), p. 012006. DOI: [10.1103/PhysRevD.91.012006](https://doi.org/10.1103/PhysRevD.91.012006). URL: <http://link.aps.org/doi/10.1103/PhysRevD.91.012006>.
 - [10] S. Chatrchyan et al. ‘Measurement of the properties of a Higgs boson in the four-lepton final state’. In: *Phys. Rev. D* 89 (9 May 2014), p. 092007. DOI: [10.1103/PhysRevD.89.092007](https://doi.org/10.1103/PhysRevD.89.092007). URL: <http://link.aps.org/doi/10.1103/PhysRevD.89.092007>.
 - [11] Helen R. Quinn. ‘The CP puzzle in the strong interactions’. In: (2001). arXiv: [hep-ph/0110050](https://arxiv.org/abs/hep-ph/0110050) [hep-ph].
 - [12] ‘Standard Model Summary Plots Spring 2020’. In: (June 2020).
 - [13] Stephen P. Martin. *A Supersymmetry primer*. [Adv. Ser. Direct. High Energy Phys.18,1(1998)]. 1997. DOI: [10.1142/9789812839657_0001](https://doi.org/10.1142/9789812839657_0001), [10.1142/9789814307505_0001](https://doi.org/10.1142/9789814307505_0001). arXiv: [hep-ph/9709356](https://arxiv.org/abs/hep-ph/9709356) [hep-ph].
 - [14] Eugenio Bianchi and Carlo Rovelli. ‘Why all these prejudices against a constant?’ In: (2010). arXiv: [1002.3966](https://arxiv.org/abs/1002.3966) [astro-ph.CO].
 - [15] The ATLAS et al. *First combination of Tevatron and LHC measurements of the top-quark mass*. 2014. arXiv: [1403.4427](https://arxiv.org/abs/1403.4427) [hep-ex].
 - [16] F. Abe et al. ‘Observation of Top Quark Production in $\bar{p}p$ Collisions with the Collider Detector at Fermilab’. In: *Phys. Rev. Lett.* 74 (14 Apr. 1995), pp. 2626–2631. DOI: [10.1103/PhysRevLett.74.2626](https://doi.org/10.1103/PhysRevLett.74.2626). URL: <https://link.aps.org/doi/10.1103/PhysRevLett.74.2626>.
 - [17] S. Abachi, B. Abbott and M. Abolins. ‘Observation of the Top Quark’. In: *Phys. Rev. Lett.* 74 (14 Apr. 1995), pp. 2632–2637. DOI: [10.1103/PhysRevLett.74.2632](https://doi.org/10.1103/PhysRevLett.74.2632). URL: <https://link.aps.org/doi/10.1103/PhysRevLett.74.2632>.
 - [18] ‘LHC Machine’. In: *JINST* 3 (2008). Ed. by Lyndon Evans and Philip Bryant, S08001. DOI: [10.1088/1748-0221/3/08/S08001](https://doi.org/10.1088/1748-0221/3/08/S08001).
 - [19] W.J. Stirling. *Parton Luminosity and Cross Section Plots*. Private Communication. URL: <http://www.hep.ph.ic.ac.uk/~wstirlin/plots/plots.html>.
 - [20] G. Aad et al. ‘The ATLAS Experiment at the CERN Large Hadron Collider’. In: *JINST* 3 (2008), S08003. DOI: [10.1088/1748-0221/3/08/S08003](https://doi.org/10.1088/1748-0221/3/08/S08003).
 - [21] S. Chatrchyan et al. ‘The CMS Experiment at the CERN LHC’. In: *JINST* 3 (2008), S08004. DOI: [10.1088/1748-0221/3/08/S08004](https://doi.org/10.1088/1748-0221/3/08/S08004).
 - [22] A. Augusto Alves Jr. et al. ‘The LHCb Detector at the LHC’. In: *JINST* 3 (2008), S08005. DOI: [10.1088/1748-0221/3/08/S08005](https://doi.org/10.1088/1748-0221/3/08/S08005).

- [23] K. Aamodt et al. ‘The ALICE experiment at the CERN LHC’. In: *JINST* 3 (2008), S08002. DOI: [10.1088/1748-0221/3/08/S08002](https://doi.org/10.1088/1748-0221/3/08/S08002).
- [24] G. Anelli et al. ‘The TOTEM experiment at the CERN Large Hadron Collider’. In: *JINST* 3 (2008), S08007. DOI: [10.1088/1748-0221/3/08/S08007](https://doi.org/10.1088/1748-0221/3/08/S08007).
- [25] O. Adriani et al. ‘The LHCf detector at the CERN Large Hadron Collider’. In: *JINST* 3 (2008), S08006. DOI: [10.1088/1748-0221/3/08/S08006](https://doi.org/10.1088/1748-0221/3/08/S08006).
- [26] John C. Collins, Davison E. Soper and George Sterman. ‘FACTORIZATION OF HARD PROCESSES IN QCD’. In: *Perturbative QCD*, pp. 1–91. DOI: [10.1142/9789814503266_0001](https://doi.org/10.1142/9789814503266_0001). eprint: https://www.worldscientific.com/doi/pdf/10.1142/9789814503266_0001. URL: https://www.worldscientific.com/doi/abs/10.1142/9789814503266_0001.
- [27] T. Aaltonen et al. ‘First Measurement of the $t\bar{t}$ Differential Cross Section $d\sigma/dM_{t\bar{t}}$ in $p\bar{p}$ Collisions at $\sqrt{s} = 1.96$ TeV’. In: *Phys. Rev. Lett.* 102 (22 June 2009), p. 222003. DOI: [10.1103/PhysRevLett.102.222003](https://doi.org/10.1103/PhysRevLett.102.222003). URL: <https://link.aps.org/doi/10.1103/PhysRevLett.102.222003>.
- [28] V.M. Abazov et al. ‘Dependence of the $t\bar{t}$ production cross section on the transverse momentum of the top quark’. In: *Physics Letters B* 693.5 (2010), pp. 515–521. ISSN: 0370-2693. DOI: <https://doi.org/10.1016/j.physletb.2010.09.011>. URL: <http://www.sciencedirect.com/science/article/pii/S0370269310010622>.
- [29] Karolos Potamianos. *The upgraded Pixel detector and the commissioning of the Inner Detector tracking of the ATLAS experiment for Run-2 at the Large Hadron Collider*. Tech. rep. ATL-PHYS-PROC-2016-104. 15 pages, EPS-HEP 2015 Proceedings. Geneva: CERN, Aug. 2016. URL: <https://cds.cern.ch/record/2209070>.
- [30] Joao Pequeno. ‘Computer Generated image of the ATLAS calorimeter’. Mar. 2008. URL: <https://cds.cern.ch/record/1095927>.
- [31] Morad Aaboud et al. ‘Performance of the ATLAS Trigger System in 2015’. In: (2016). arXiv: [1611.09661](https://arxiv.org/abs/1611.09661) [hep-ex].
- [32] *Trigger Menu in 2017*. Tech. rep. ATL-DAQ-PUB-2018-002. Geneva: CERN, June 2018. URL: <http://cds.cern.ch/record/2625986>.
- [33] Sebastian Artz et al. *Upgrade of the ATLAS Central Trigger for LHC Run-2*. Tech. rep. ATL-DAQ-PROC-2014-042. 02. Geneva: CERN, Nov. 2014. URL: <https://cds.cern.ch/record/1969488>.
- [34] R Achenbach et al. ‘The ATLAS Level-1 Calorimeter Trigger’. In: *Journal of Instrumentation* 3.03 (2008), P03001. URL: <http://stacks.iop.org/1748-0221/3/i=03/a=P03001>.
- [35] P Plucinski. ‘Upgrades to the ATLAS Level-1 Calorimeter Trigger’. In: *Journal of Instrumentation* 9.01 (2014), p. C01023. URL: <http://stacks.iop.org/1748-0221/9/i=01/a=C01023>.

- [36] *Performance of the ATLAS muon trigger in 2011*. Tech. rep. ATLAS-CONF-2012-099. Geneva: CERN, July 2012. URL: <https://cds.cern.ch/record/1462601>.
- [37] Eduard Simioni. ‘The Topological Processor for the future ATLAS Level-1 Trigger: from design to commissioning’. In: (2014). arXiv: [1406.4316](https://arxiv.org/abs/1406.4316) [physics.ins-det].
- [38] ATLAS Collaboration. *ApprovedPlotsDAQ*. URL: <https://twiki.cern.ch/twiki/bin/view/AtlasPublic/ApprovedPlotsDAQ>.
- [39] G. Duckeck et al. ‘ATLAS computing: Technical design report’. In: (2005). URL: <http://cds.cern.ch/record/837738>.
- [40] CERN. *HL-LHC UPDATES IN JAPAN*. URL: <http://cds.cern.ch/journal/CERNBulletin/2015/01/News%5C%20Articles/1975962>.
- [41] Apollinari G. et al. *High-Luminosity Large Hadron Collider (HL-LHC): Technical Design Report V. 0.1*. CERN Yellow Reports: Monographs. Geneva: CERN, 2017. DOI: [10.23731/CYRM-2017-004](https://doi.org/10.23731/CYRM-2017-004). URL: <https://cds.cern.ch/record/2284929>.
- [42] ATLAS Collaboration. *Technical Design Report for the Phase-II Upgrade of the ATLAS TDAQ System*. Tech. rep. CERN-LHCC-2017-020. ATLAS-TDR-029. Geneva: CERN, Sept. 2017. URL: <https://cds.cern.ch/record/2285584>.
- [43] ‘Technical Design Report for the ATLAS Inner Tracker Strip Detector’. In: (Apr. 2017).
- [44] ATLAS Collaboration. *Technical Design Report for the ATLAS Inner Tracker Pixel Detector*. Tech. rep. CERN-LHCC-2017-021. ATLAS-TDR-030. Geneva: CERN, Sept. 2017. URL: <http://cds.cern.ch/record/2285585>.
- [45] T. Kawamoto et al. ‘New Small Wheel Technical Design Report’. In: (June 2013).
- [46] Intel. *Intel Stratix 10 Variable Precision DSP Blocks User Guide*. 2018. URL: <https://www.intel.com/content/dam/www/programmable/us/en/pdfs/literature/hb/stratix-10/ug-s10-dsp.pdf> (visited on 27/11/2018).
- [47] Intel. *Intel Stratix 10*. 2018. URL: <https://www.intel.com/content/dam/www/programmable/us/en/pdfs/literature/pt/stratix-10-mx-product-table.pdf> (visited on 27/11/2018).
- [48] ‘Luminosity determination in pp collisions at $\sqrt{s} = 13$ TeV using the ATLAS detector at the LHC’. In: (June 2019).
- [49] Stefano Frixione, Paolo Nason and Carlo Oleari. ‘Matching NLO QCD computations with parton shower simulations: the POWHEG method’. In: *Journal of High Energy Physics* 2007.11 (Nov. 2007), pp. 070–070. ISSN: 1029-8479. DOI: [10.1088/1126-6708/2007/11/070](https://doi.org/10.1088/1126-6708/2007/11/070). URL: <http://dx.doi.org/10.1088/1126-6708/2007/11/070>.

- [50] J. Alwall et al. ‘The automated computation of tree-level and next-to-leading order differential cross sections, and their matching to parton shower simulations’. In: *Journal of High Energy Physics* 2014.7 (July 2014). ISSN: 1029-8479. DOI: [10.1007/jhep07\(2014\)079](https://doi.org/10.1007/jhep07(2014)079). URL: [http://dx.doi.org/10.1007/JHEP07\(2014\)079](http://dx.doi.org/10.1007/JHEP07(2014)079).
- [51] Torbjörn Sjöstrand, Stephen Mrenna and Peter Skands. ‘A brief introduction to PYTHIA 8.1’. In: *Computer Physics Communications* 178.11 (2008), pp. 852–867. ISSN: 0010-4655. DOI: <https://doi.org/10.1016/j.cpc.2008.01.036>. URL: <http://www.sciencedirect.com/science/article/pii/S0010465508000441>.
- [52] M. Bahr et al. ‘Herwig++ Physics and Manual’. In: *Eur. Phys. J. C* 58 (2008), pp. 639–707. DOI: [10.1140/epjc/s10052-008-0798-9](https://doi.org/10.1140/epjc/s10052-008-0798-9). arXiv: [0803.0883](https://arxiv.org/abs/0803.0883) [hep-ph].
- [53] T. Gleisberg et al. ‘Event generation with SHERPA 1.1’. In: *JHEP* 02 (2009), p. 007. DOI: [10.1088/1126-6708/2009/02/007](https://doi.org/10.1088/1126-6708/2009/02/007). arXiv: [0811.4622](https://arxiv.org/abs/0811.4622) [hep-ph].
- [54] Bo Andersson et al. ‘Parton Fragmentation and String Dynamics’. In: *Phys. Rept.* 97 (1983), pp. 31–145. DOI: [10.1016/0370-1573\(83\)90080-7](https://doi.org/10.1016/0370-1573(83)90080-7).
- [55] B.R. Webber. ‘A QCD Model for Jet Fragmentation Including Soft Gluon Interference’. In: *Nucl. Phys. B* 238 (1984), pp. 492–528. DOI: [10.1016/0550-3213\(84\)90333-X](https://doi.org/10.1016/0550-3213(84)90333-X).
- [56] S. Agostinelli et al. ‘GEANT4—a simulation toolkit’. In: *Nucl. Instrum. Meth. A* 506 (2003), pp. 250–303. DOI: [10.1016/S0168-9002\(03\)01368-8](https://doi.org/10.1016/S0168-9002(03)01368-8).
- [57] W Lukas. *Fast Simulation for ATLAS: Atlfast-II and ISF*. Tech. rep. ATL-SOFT-PROC-2012-065. Geneva: CERN, June 2012. DOI: [10.1088/1742-6596/396/2/022031](https://doi.org/10.1088/1742-6596/396/2/022031). URL: <https://cds.cern.ch/record/1458503>.
- [58] Richard D. Ball et al. ‘Parton distributions for the LHC run II’. In: *Journal of High Energy Physics* 2015.4 (Apr. 2015). ISSN: 1029-8479. DOI: [10.1007/jhep04\(2015\)040](https://doi.org/10.1007/jhep04(2015)040). URL: [http://dx.doi.org/10.1007/JHEP04\(2015\)040](http://dx.doi.org/10.1007/JHEP04(2015)040).
- [59] Richard D. Ball et al. ‘Parton distributions with LHC data’. In: *Nuclear Physics B* 867.2 (Feb. 2013), pp. 244–289. ISSN: 0550-3213. DOI: [10.1016/j.nuclphysb.2012.10.003](https://doi.org/10.1016/j.nuclphysb.2012.10.003). URL: <http://dx.doi.org/10.1016/j.nuclphysb.2012.10.003>.
- [60] *ATLAS Pythia 8 tunes to 7 TeV datas*. Tech. rep. ATL-PHYS-PUB-2014-021. Geneva: CERN, Nov. 2014. URL: <https://cds.cern.ch/record/1966419>.
- [61] *Simulation of top quark production for the ATLAS experiment at sqrt(s) = 13 TeV*. Tech. rep. ATL-PHYS-PUB-2016-004. Geneva: CERN, Jan. 2016. URL: <https://cds.cern.ch/record/2120417>.

- [62] L. A. Harland-Lang et al. ‘Parton distributions in the LHC era: MMHT 2014 PDFs’. In: *The European Physical Journal C* 75.5 (May 2015). ISSN: 1434-6052. DOI: [10.1140/epjc/s10052-015-3397-6](https://doi.org/10.1140/epjc/s10052-015-3397-6). URL: <http://dx.doi.org/10.1140/epjc/s10052-015-3397-6>.
- [63] *Studies on top-quark Monte Carlo modelling with Sherpa and MG5_aMC@NLO*. Tech. rep. ATL-PHYS-PUB-2017-007. Geneva: CERN, May 2017. URL: <https://cds.cern.ch/record/2261938>.
- [64] Stefan Höche et al. ‘QCD matrix elements and truncated showers’. In: *Journal of High Energy Physics* 2009.05 (May 2009), pp. 053–053. ISSN: 1029-8479. DOI: [10.1088/1126-6708/2009/05/053](https://doi.org/10.1088/1126-6708/2009/05/053). URL: <http://dx.doi.org/10.1088/1126-6708/2009/05/053>.
- [65] Fabio Cascioli, Philipp Maierhofer and Stefano Pozzorini. ‘Scattering Amplitudes with Open Loops’. In: *Phys. Rev. Lett.* 108 (2012), p. 111601. DOI: [10.1103/PhysRevLett.108.111601](https://doi.org/10.1103/PhysRevLett.108.111601). arXiv: [1111.5206 \[hep-ph\]](https://arxiv.org/abs/1111.5206).
- [66] W Lampl et al. *Calorimeter Clustering Algorithms: Description and Performance*. Tech. rep. ATL-LARG-PUB-2008-002. ATL-COM-LARG-2008-003. Geneva: CERN, Apr. 2008. URL: <https://cds.cern.ch/record/1099735>.
- [67] *Electron efficiency measurements with the ATLAS detector using the 2015 LHC proton-proton collision data*. Tech. rep. ATLAS-CONF-2016-024. Geneva: CERN, June 2016. URL: <https://cds.cern.ch/record/2157687>.
- [68] J. Illingworth and J. Kittler. ‘A survey of the hough transform’. In: *Computer Vision, Graphics, and Image Processing* 44.1 (1988), pp. 87–116. ISSN: 0734-189X. DOI: [https://doi.org/10.1016/S0734-189X\(88\)80033-1](https://doi.org/10.1016/S0734-189X(88)80033-1). URL: <http://www.sciencedirect.com/science/article/pii/S0734189X88800331>.
- [69] Matteo Cacciari, Gavin P Salam and Gregory Soyez. ‘The anti-ktjet clustering algorithm’. In: *Journal of High Energy Physics* 2008.04 (Apr. 2008), pp. 063–063. ISSN: 1029-8479. DOI: [10.1088/1126-6708/2008/04/063](https://doi.org/10.1088/1126-6708/2008/04/063). URL: <http://dx.doi.org/10.1088/1126-6708/2008/04/063>.
- [70] Georges Aad et al. ‘Performance of pile-up mitigation techniques for jets in pp collisions at $\sqrt{s} = 8$ TeV using the ATLAS detector’. In: *Eur. Phys. J. C* 76.11 (2016), p. 581. DOI: [10.1140/epjc/s10052-016-4395-z](https://doi.org/10.1140/epjc/s10052-016-4395-z). arXiv: [1510.03823 \[hep-ex\]](https://arxiv.org/abs/1510.03823).
- [71] M. Aaboud et al. ‘Jet energy scale measurements and their systematic uncertainties in proton-proton collisions at $\sqrt{s} = 13$ TeV with the ATLAS detector’. In: *Phys. Rev. D* 96.7 (2017), p. 072002. DOI: [10.1103/PhysRevD.96.072002](https://doi.org/10.1103/PhysRevD.96.072002). arXiv: [1703.09665 \[hep-ex\]](https://arxiv.org/abs/1703.09665).
- [72] *Optimisation of the ATLAS b-tagging performance for the 2016 LHC Run*. Tech. rep. ATL-PHYS-PUB-2016-012. Geneva: CERN, June 2016. URL: <http://cds.cern.ch/record/2160731>.

- [73] ‘Performance of b-jet identification in the ATLAS experiment’. In: *Journal of Instrumentation* 11.04 (Apr. 2016), P04008–P04008. ISSN: 1748-0221. DOI: [10.1088/1748-0221/11/04/p04008](https://doi.org/10.1088/1748-0221/11/04/p04008). URL: <http://dx.doi.org/10.1088/1748-0221/11/04/P04008>.
- [74] Particle Data Group et al. ‘Review of Particle Physics’. In: *Progress of Theoretical and Experimental Physics* 2020.8 (Aug. 2020). 083C01. ISSN: 2050-3911. DOI: [10.1093/ptep/ptaa104](https://doi.org/10.1093/ptep/ptaa104). eprint: <https://academic.oup.com/ptep/article-pdf/2020/8/083C01/33653179/ptaa104.pdf>. URL: <https://doi.org/10.1093/ptep/ptaa104>.
- [75] Johannes Erdmann et al. ‘A likelihood-based reconstruction algorithm for top-quark pairs and the KLFitter framework’. In: *Nuclear Instruments and Methods in Physics Research Section A: Accelerators, Spectrometers, Detectors and Associated Equipment* 748 (June 2014), pp. 18–25. ISSN: 0168-9002. DOI: [10.1016/j.nima.2014.02.029](https://doi.org/10.1016/j.nima.2014.02.029). URL: <http://dx.doi.org/10.1016/j.nima.2014.02.029>.
- [76] G. Aad et al. ‘Jet energy measurement and its systematic uncertainty in protonproton collisions at $\sqrt{s} = 7$ TeV with the ATLAS detector’. In: *The European Physical Journal C* 75.1 (Jan. 2015). ISSN: 1434-6052. DOI: [10.1140/epjc/s10052-014-3190-y](https://doi.org/10.1140/epjc/s10052-014-3190-y). URL: <http://dx.doi.org/10.1140/epjc/s10052-014-3190-y>.
- [77] ‘Tagging and suppression of pileup jets’. In: (May 2014).
- [78] Sebastian Heer. ‘The secondary vertex finding algorithm with the ATLAS detector’. In: *PoS EPS-HEP2017* (2017). Ed. by Paolo Checchia et al., p. 762. DOI: [10.22323/1.314.0762](https://doi.org/10.22323/1.314.0762).
- [79] Jon Butterworth et al. ‘PDF4LHC recommendations for LHC Run II’. In: *Journal of Physics G: Nuclear and Particle Physics* 43.2 (Jan. 2016), p. 023001. ISSN: 1361-6471. DOI: [10.1088/0954-3899/43/2/023001](https://doi.org/10.1088/0954-3899/43/2/023001). URL: <http://dx.doi.org/10.1088/0954-3899/43/2/023001>.
- [80] F. Bazzocchi et al. ‘Quark contact interactions at the LHC’. In: *Phys. Rev. D* 85 (11 June 2012), p. 114001. DOI: [10.1103/PhysRevD.85.114001](https://doi.org/10.1103/PhysRevD.85.114001). URL: <https://link.aps.org/doi/10.1103/PhysRevD.85.114001>.
- [81] Micha Czakon and Alexander Mitov. ‘Top++: A program for the calculation of the top-pair cross-section at hadron colliders’. In: *Computer Physics Communications* 185.11 (Nov. 2014), pp. 2930–2938. ISSN: 0010-4655. DOI: [10.1016/j.cpc.2014.06.021](https://doi.org/10.1016/j.cpc.2014.06.021). URL: <http://dx.doi.org/10.1016/j.cpc.2014.06.021>.
- [82] Simone Alioli, Sven-Olaf Moch and Peter Uwer. ‘Hadronic top-quark pair-production with one jet and parton showering’. In: *Journal of High Energy Physics* 2012.1 (Jan. 2012). ISSN: 1029-8479. DOI: [10.1007/jhep01\(2012\)137](https://doi.org/10.1007/jhep01(2012)137). URL: [http://dx.doi.org/10.1007/JHEP01\(2012\)137](http://dx.doi.org/10.1007/JHEP01(2012)137).
- [83] Michal Czakon et al. ‘Top-pair production at the LHC through NNLO QCD and NLO EW’. In: *Journal of High Energy Physics* 2017.10 (Oct.

- 2017). ISSN: 1029-8479. DOI: [10.1007/jhep10\(2017\)186](https://doi.org/10.1007/jhep10(2017)186). URL: [http://dx.doi.org/10.1007/JHEP10\(2017\)186](http://dx.doi.org/10.1007/JHEP10(2017)186).
- [84] Peter Bärnreuther, Michal Czakon and Alexander Mitov. ‘Percent-Level Precision Physics at the Tevatron: Next-to-Next-to-Leading Order QCD Corrections to $q\bar{q} \rightarrow t\bar{t} + X$ ’. In: *Physical Review Letters* 109.13 (Sept. 2012). ISSN: 1079-7114. DOI: [10.1103/physrevlett.109.132001](https://doi.org/10.1103/physrevlett.109.132001). URL: <http://dx.doi.org/10.1103/PhysRevLett.109.132001>.
- [85] Micha Czakon and Alexander Mitov. ‘NNLO corrections to top-pair production at hadron colliders: the all-fermionic scattering channels’. In: *Journal of High Energy Physics* 2012.12 (Dec. 2012). ISSN: 1029-8479. DOI: [10.1007/jhep12\(2012\)054](https://doi.org/10.1007/jhep12(2012)054). URL: [http://dx.doi.org/10.1007/JHEP12\(2012\)054](http://dx.doi.org/10.1007/JHEP12(2012)054).
- [86] Michal Czakon and Alexander Mitov. ‘NNLO corrections to top pair production at hadron colliders: the quark-gluon reaction’. In: *Journal of High Energy Physics* 2013.1 (Jan. 2013). ISSN: 1029-8479. DOI: [10.1007/jhep01\(2013\)080](https://doi.org/10.1007/jhep01(2013)080). URL: [http://dx.doi.org/10.1007/JHEP01\(2013\)080](http://dx.doi.org/10.1007/JHEP01(2013)080).
- [87] G. Aad et al. ‘Measurements of top-quark pair differential and double-differential cross-sections in the ℓ +jets channel with pp collisions at $\sqrt{s} = 13$ TeV using the ATLAS detector’. In: *The European Physical Journal C* 79.12 (Dec. 2019). ISSN: 1434-6052. DOI: [10.1140/epjc/s10052-019-7525-6](https://doi.org/10.1140/epjc/s10052-019-7525-6). URL: <http://dx.doi.org/10.1140/epjc/s10052-019-7525-6>.
- [88] M. Aaboud et al. ‘Measurements of $t\bar{t}$ differential cross-sections of highly boosted top quarks decaying to all-hadronic final states in pp collisions at $\sqrt{s} = 13$ TeV using the ATLAS detector’. In: *Physical Review D* 98.1 (July 2018). ISSN: 2470-0029. DOI: [10.1103/physrevd.98.012003](https://doi.org/10.1103/physrevd.98.012003). URL: <http://dx.doi.org/10.1103/PhysRevD.98.012003>.
- [89] Adam Paszke et al. ‘PyTorch: An Imperative Style, High-Performance Deep Learning Library’. In: *Advances in Neural Information Processing Systems* 32. Curran Associates, Inc., 2019, pp. 8024–8035. URL: <http://papers.neurips.cc/paper/9015-pytorch-an-imperative-style-high-performance-deep-learning-library.pdf>.
- [90] Anja Butter et al. ‘Deep-learned Top Tagging with a Lorentz Layer’. In: *SciPost Phys.* 5.3 (2018), p. 028. DOI: [10.21468/SciPostPhys.5.3.028](https://doi.org/10.21468/SciPostPhys.5.3.028). arXiv: [1707.08966](https://arxiv.org/abs/1707.08966) [hep-ph].
- [91] C. Rovelli and F. Vidotto. *Covariant Loop Quantum Gravity: An Elementary Introduction to Quantum Gravity and Spinfoam Theory*. Cambridge University Press, 2014. ISBN: 9781107706910.
- [92] Jonathan L. Feng et al. ‘ForwArd Search ExpeRiment at the LHC’. In: *Phys. Rev. D* 97 (3 Feb. 2018), p. 035001. DOI: [10.1103/PhysRevD.97.035001](https://doi.org/10.1103/PhysRevD.97.035001). URL: <https://link.aps.org/doi/10.1103/PhysRevD.97.035001>.

- [93] ‘The Pythia 8 A3 tune description of ATLAS minimum bias and in-elastic measurements incorporating the Donnachie-Landshoff diffractive model’. In: (Aug. 2016).
- [94] Luca Scodellaro. *b tagging in ATLAS and CMS*. 2017. arXiv: [1709.01290](https://arxiv.org/abs/1709.01290) [hep-ex].
- [95] Serena Palazzo. ‘Measurements of differential cross sections of top quark pair production in association with jets in pp collisions at $\sqrt{s} = 13$ TeV using the ATLAS detector’. Presented 20 Jul 2018. Nov. 2017. URL: <https://cds.cern.ch/record/2645488>.